DEVELOPMENT OF LOAD MEASUREMENT TECHNIQUE FOR ARBITRARY
SHAPES

A Thesis

presented to

the Faculty of California Polytechnic State University,

San Luis Obispo

In Partial Fulfillment

of the Requirements for the Degree

Master of Science in Aerospace Engineering

by

Quintin J. Cockrell

December 2023

COMMITTEE MEMBERSHIP

TITLE: Development of Load Measurement Technique for Arbitrary Shapes

AUTHOR: Quintin J. Cockrell

DATE SUBMITTED: December 2023

COMMITTEE CHAIR: Nandeesh Hiremath, Ph.D.
Professor of Aerospace Engineering

COMMITTEE MEMBER: Aaron Drake, Ph.D.
Professor of Aerospace Engineering

COMMITTEE MEMBER: Hans Mayer, Ph.D.
Professor of Mechanical Engineering

COMMITTEE MEMBER: John Fabijanic, M.S.
Lecturer of Mechanical Engineering

ABSTRACT

Development of Load Measurement Technique for Arbitrary Shapes

Quintin J. Cockrell

Obtaining aerodynamic forces and moments about all three orthogonal axes for arbitrary shapes at arbitrary orientations in a fast manner via a measurement technique specific to Cal Poly's low-speed wind tunnel to continually obtain the forces and moments under quasi-steady conditions is explored. A Continuous Rotation Technique (CR) uses a 6-DOF load cell and stepper motor to rotate an object about an axis for a complete rotation. The forces and moments acting upon the object pass through the stepper motor and interface plates and recorded by the load cell as the object is rotated continuously a finite number of rotations. An optical encoder installation tracks the progress of a rotation serving indicator between the subsequent rotations to determine starting angles and body slippage. Average loading of measurements at each timestep along the average time for rotation is found. This dataset along the average time is placed in 1-degree bins and averaged to a final dataset of load measurements at 0.5-degree intervals for a complete 360-degree load map. Testing of this technique is performed on aspect ratio 1 circular cylinder and for a sphere. These test cases are representative of the 3D flow features that are prevalent for bodies of finite aspect ratios. The airloads on these canonical shapes were used to calibrate the measurement technique deriving similarity with prior work performed at Georgia Tech's wind tunnel. This thesis showcases the repeatability of the results in a different and smaller wind tunnel with improved certainty on angle measurements. The scope of the thesis tackles the showcase of an initial proof of concept for the incorporation of such a novel measurement technique using Cal Poly resources.

ACKNOWLEDGMENTS

TABLE OF CONTENTS

LIST OF TABLES

LIST OF FIGURES

LIST OF SYMBOLS

ω Angular Velocity (m/s)

ρ Fluid Density (kg/m^3)

σ_t Total Measurement Uncertainty

σ_{sys} Systemic Uncertainty

σ_{stat} Statistical Uncertainty

A Test Body Frontal Projected Area (m^2)

AR Aspect Ratio

b Test Body Radius (m)

cal Load Cell Calibration Factor

C_d Drag Coefficient

CR Continuous Rotation

d_{st} Predicted Rod Deflection (m)

E Young's Modulus of Steel (Pa)

F Force (N)

F_{full} Fullscale Force of Load Cell (N)

F_{st} Predicted Force Bending Steel Rod (N)

f Frequency (Hz)

f_s Sampling Rate (Hz)

f_N Nyquist Frequency

I_{st} Mounting Rod Second Moment of Inertia (m^4)

k Reduced Frequency

L_{st} Mounting Rod Length (m)

$LSWT$ Low Speed Wind Tunnel

Re Reynolds Number

r_{st} Mounting Rod Radius (m)

St_{RPM} Stepper Motor Rotation Rate (RPM)

T Torque $(N-m)$

V Velocity (m/s)

V_{exc} Excitation Voltage (V)

V_{mea} Measured Voltage (V)

Chapter 1

INTRODUCTION

1.1   Problem Statement

Aerodynamic loading of bluff bodies within a freestream flow has been an area of interest of wind tunnel testing for many years, given the many applications and use of bluff bodies in various engineering and science sectors. One of the most common forms of which a bluff bodied object is has been tested is that of the long ciruclar cylinder orientated perpendicular to the freestream. The extent of testing of this attitude of the cylinder has allowed for the development of empirical models for prediction of the aerodynamic loading in lift and drag acting on the object in a 2D problem. The simple nature of a single stationary testing orientation also allows for wind tunnel testing within the current facilities at Cal Poly to be well within feasible. This is confirmed with the inclusion of this very setup within one of the labs currently offered at Cal Poly. The feasibility however, quickly becomes impractical for our current lab capabilities when the testing on the same object tries to incorporate multiple attitudes of the test body.

When bluff bodies are considered for real-world application it is often the case that the object in question is expected to take an arbitrary number of orientations relative to the freestream. This can result in substantial changes to the aerodynamic loading of the object in the presence of small changes in attitude. The problem of load prediction becomes more complex when the body in question takes on a more complex or arbitrary shape than that of a simple ciruclar cylinder. Regions of an arbitrary bluff body facing the flow may experience high pressure as a resultant of flow stagnation

while aft surfaces experiencing separated flow have low pressure. Complex geometry can take the form of sharp edges that can trigger separation and the generation of strong vortices and possible unsteady flow increasing the difficulty of load prediction. A complete aerodynamic load map for any given object, in any attitude, is an essential piece for researchers to gain a better understanding of how the relationship between an object's geometry and attitude impact the 6-DOF loads acting upon it.

1.2 Motivation

The process of taking force and moment measurements within a wind tunnel environment takes significant time allocation that can be diffcult to arrange for high trafficked wind tunnels like those in academic settings such as the Cal Poly Low Speed Wind Tunnel (LSWT). This challenge is further increased when a more detailed resolution is desired about a given axis of 1-degree or less. The Continuous Rotation technique (CR) developed at Georgia Tech achieves a significant reduction for testing duration, 10 minutes per axis using 10 rotations, to obtain quasi-steady 6-DOF component loads on a given test object. This opens the possibility for faster and higher quality load maps to be studied and cataloged within the LSWT. The setup and incorporation of the CR technique within the current facilities of the LSWT will greatly expand the scope of testing for laboratory classes, individual student research opportunities, and expansion of basic research into 3D Bluff Bodies of arbitrary shapes.

1.3 Objective

This work tests the repeatability of the CR technique with Cal Poly's $3ft \times 4ft$ wind tunnel. The goal of this work is to progress the continuation of this technique with an emphasis on improving the certainty of angular measurement of the test object over a given test run. Prior iterations of this technique relied on motor step size and sampling rates of the load cell to map aerodynamic loading a full 360-degree profile. Improvements to the test rig setup seek to isolate outliers of results in the event of motor slippage allowing higher fidelity. The primary objective is to demonstrate feasibility of replicating the CR technique setup within a smaller wind tunnel test section. Methods for the characterization of the operational limits, testing ranges, and quantitative assessment of sources of error and overall uncertainties is established. The results are collected through testing of an aspect ratio one circular cylinder and sphere. The scope of these test objects are to provide an initial proof of concept and highlight concerns to be addressed with future work for improvements to this preliminary setup. These test objects being canonical shapes offer 3D flow features like attached/detached vortices on the side surfaces of the cylinder, sharp edge vortex development at the leading edges of the side plates, and vortex shedding phenomena. Such flow features are representative of 3D Bluff objects of finite aspect ratios. These tests articles serve as a test bed for quantifying the overall measurement uncertainties and system limitations.

Chapter 2

BACKGROUND ON BLUFF-BODY AERODYNAMICS AND STATE-OF-ART

MEASUREMENT TECHNIQUES

A review of literature and previous implementation of CR enhances the understanding of how the technique is able to provide the quasi-steady load maps. This section includes examples of how CR can provide solutions for real-world applications, wind tunnel testing shortcomings, and wind tunnel time allocation. The characteristics of bluff bodies are reviewed to understand why CR specifically serves as an ideal means for obtaining measurements on bodies of finite aspect ratios. Advances in the field of force measurement tools are covered to highlight the growing feasibility of CR implementation in facilities, the size and scope as offered by LSWT. Finally, CR is detailed to provide understanding of its fundamentals that will be used for implementation within Cal Poly facilities.

2.1   The Slung Load Problem

A specific field where a sufficiently accurate means of arbitrary bluff body load prediction could prove to be highly beneficial is that of rotorcraft slung loads. In the majority of these missions a helicopter, manned or unmanned, in transportation operations such as water delivery for combating forest fires, emergency supplies, search and rescue, food delivery, and emergency medical evac. In all of these cases, typically a non-streamlined object is carried as a slung load underneath the rotorcraft supported by cables or chains. The suspension system is commonly attached using a single-point attachment that allows for roll, pitch, and yaw oscillations [26, 44, 50].

This allows the object to take nearly any attitude towards the oncoming freestream resulting in all six components of aerodynamic loading potentially playing a significant role [51]. Uncertainty of these loads can influence the limit of speed that rotorcraft are allowed to travel while possessing these slung loads [16].

The speed is often set not as a reflection of vehicle performance, but out of safety of the slung load experiencing large amplitude or divergent oscillations that would threaten the safety of the vehicle or slung load [69]. A more accurate means of predicting the loads for a body at an arbitrary attitude would allow for a more precise speed limit to be placed for each particular slung load. This would benefit the end users by potentially increasing the operation speed for a particular mission due to having a better understanding at what conditions the slung load would become unsafe.

Increased mission speed will substantial increase the efficiency of missions previously listed by shortening the time water is transported to fires, emergency supplies are delivered to locations, or the increase in speed will lead to a safer mission to the crew of the rotorcraft in the case of missions within hostile territories and being able to enter and exit these regions at a faster pace. A higher fidelity for load prediction would also serve to increase certainty of operations involving the dropping of these bluff bodies from their slung load orientation to specific drop locations for supply and re-supplying based missions where landing would cause unnecessary risk to flight and ground crews. As the objects fall through the sky they can experience unexpected side forces and moments altering its landing trajectory away from its intended location [62]. These benefits lead the desire for a complete load map at arbitrary attitude of a given bluff body to better understand the forces and moments acting on a particular body. This poses the challenge to quickly and iteratively measure loads on practical shapes about arbitrary orientations.

2.1.1 The Challenge of Bluff Body Wind Tunnel Testing

The field of experimental measurement has historically been limited by the time and resources allocated to any given series of tests. This is a characteristic that is also shared by the low speed wind tunnel present at Cal Poly. This particular wind tunnel sees use not only for pedagogical purposes, but also from student researchers, and sponsored projects. All of these groups and individuals seeking time to use the wind tunnel located on campus results in a more difficult time to use the wind tunnel for higher resolution and extensive measurements, particular for basic research on bluff bodies. To combat this projects often must simplify to fit within the time constraints available to them. When this is applied to testing an object over a range of attitude, say azimuthal resolution, increment steps must be increased to scales of typically 15 degrees [52, 35]. This is done since traditional testing practice has the test object firmly supported and positioned at a specific orientation within the freestream flow of the wind tunnel for a period of time long enough to obtain stationary statistical measurements [68]. Conventionally, the tunnel is then shutdown and a lab technician is required to open up the test section of the wind tunnel to manipulate or remount the test object in the next orientation of interest. When this practice is repeated over the course of a complete resolution around an axis of a test object a substantial time commitment is made unless sacrifices are made to the resolution. The same can be said assuming symmetry as a means to reduce the workload of the test. This time limitation prevents a complete load map to be made for a given object and restricts the test subject selection to more symmetrical objects as an arbitrary shaped object would further increase the complexity and labor of a complete load map.

This highlights a key shortcoming of the current facilities available at the LSWT regarding the testing of bluff body objects. Bluff bodies while containing a substantial amount of symmetrical test objects, spheres and cylinders, also encompasses an infinite array of arbitrary shapes possessing little to no symmetry. Furthermore, unlike streamlined object like airfoils which are expected to operate within a far smaller range of attitudes, bluff bodies, as demonstrated from slung loads, are expected to be placed within a much more extensive range of orientations [26, 44, 50, 69]. The result is a need for a new method of load measurement for test objects that reduces the time in which stationary statistical measurements are taken for a given orientation. This method of measurement must also reduce the amount of time taken for manipulation of the test object attitude. A method that is able to achieve both of these goals will provide a means for higher resolution measurements as the time saved compared to traditional testing practice can be reinvested in testing at more attitude positions along all principle axis of a body to create a complete loading map for analysis.

It was with these goals in mind that a group of researchers at Georgia Tech's Aerospace Engineering department pioneered a new load measurement technique focused on bluff body airload load mapping. The development and validation of the system created at Georgia Tech has opened up the possibilities for a simplified and time efficient means of measuring force and moment measurements of bluff bodies at any arbitrary attitude. Their work continued by post processing these measurements as a truncated set of Fourier series coefficients allowing for easy database construction and cross-referencing between objects. The construction and further expansion of these coefficient catalogs further assists with estimation of non-tested bodies via combining and interpolation between similarly shaped objects already cataloged [43].

The accurate estimation through these catalogs also provides a means of reducing time needed for studying the forces on arbitrary shapes since wind tunnel testing of each individual arbitrary body of interest are no longer needed. As the catalogs used for estimation become larger in scope, a further refinement of the untested body estimation is to be expected. This is the driving force for this thesis project to prove this same measuring technique can be achieved with the facilities available at Cal Poly and to implement and validate that system with testing of canonical bluff bodies, a circular cylinder and sphere, showing similarities with published data sets from Georgia Tech [27]. This systematically validated technique will provide avenues to build the airload catalogs for untested bodies.

2.1.2 The Challenge of Wind Tunnel Time Allocation

A perfect demonstration of the substantial time commitment that can be taken up by wind tunnel testing at various attitudes can be seen by the bicycle testing offered at the A2 Wind tunnel [1]. This process sees cyclists place their bikes within the wind tunnel to record the wind effects at different yaw angles. The initial loading stage of bicycle into the wind tunnel takes a total of 5 minutes. A tare reading of 20 seconds of the tunnel off is taken for calibration of results. An additional 20 seconds are needed to get the wind tunnel up to speed and steady before measurements can be taken. This thus far has not been a large requirement of time to operate and use a wind tunnel for testing, but the problem emerges when changes to yaw are considered.

The process to change a yaw angle for the model, stabilize the flow, and take two 22 second average readings takes approximately 1 minute. While this might not at first appear to be substantial, one must consider what that will result in for high fidelity testing like what would be decided for bodies of arbitrary shapes. The A2 services allows for a plus/minus 25-degrees of yaw movement at increments as small as 0.1 degrees. If a full loading map at the highest fidelity was desired this would take 500 specific attitudes with each taking a minute to collect. A table with an itemized list for a test of this extent is shown in Table 1 below to tally the total time commitment.

Table 2.1: A2 Wind Tunnel with 0.1 Degree Fidelity Testing Time

Action	Action Time (sec)	Test Time (hr)
Mounting	300	0.083
Tare	20	0.088
Startup	20	0.094
Measurement/Attitude Change	60	8.427
Shutdown	10	8.429

It is also worth noting that this itemization assumes one wind tunnel run between all yaw attitude measurements. This may impart impacts to the flow field that the 60 seconds for movement and stabilization is not correcting for. If static measurements were to be guaranteed the tunnel would need to be started up and shutdown for each increment even further increasing the time needed. This would be more traditional to model manipulation methods that have been employed by Cal Poly in previous years for certain experiments or labs conducted within the LSWT.

2.2 Bluff Body Characteristics

Of all the aerodynamic forces that are exerted on an object as it moves through a uniform flow, the most dominant force acting on non-lifting bodies is drag [31]. Drag is often made up of two components, namely, pressure drag and skin friction drag. Pressure drag is characterized by the formation of wakes shedding off of the object as it travels through a fluid. This association with wakes results in low pressure regions, being sensitive to flow separation that are predominantly seen in the aft portions of the bodies. Further, for finite aspect ratios, such effects are aggravated on the lee side and windward side surfaces. A bluff body is an object who's shape results in flow separation over a substantial portion of the object's surface [2, 11]. Counter to a streamlined object with geometry that promotes as little flow separation as possible. These differences between bluff and streamlined bodies is what leads bluff bodies to have pressure drag as the dominating component of drag compared to a streamline body where the pressure drag ideally is a far less substantial portion of the total drag [46, 38]. Since object geometry plays the largest role in pressure drag experienced, parameters such as the Reynolds number are usually little impact on changes to pressure drag [4]. However, such a claim is limited to 2D shapes. The 3D effects are far more complicated involving vortical structures at varied time and length scales.

Frictional drag makes up the second component of the total drag of an object. This drag can be understood as drag induced by the friction experienced between the surface of the object and the fluid passing over it. Frictional drag is able to represent a larger portion of total drag when the flow remains attached to an object for a longer portion of the object's skin. This means that the more surface area that an object has within the attached region of the flow the more frictional drag that will be created. These characteristics are the primary reasons as to why frictional drag is usually the

dominating drag experienced by streamlined bodies. Optimally designed streamlined shapes can sustain attached flows on the entire wetted surface, leading to higher skin friction drag. This is not true for bluff body objects that experience sizable portions of their surface within regions of separated flow where the skin friction drag is drastically lower [40, 36, 13, 56]. The interaction between the attached flow and the surface area of the object also means that increases to the freestream Reynolds number can drastically impact the frictional drag, and therefore the total drag on an object since pressure drag remains relatively unchanged by increases to Reynolds Number [4, 58, 61]. It must be noted that although freestream Re has less effect on overall pressure drag, surface finishing, roughness, or viscosity greatly influences the flow separation lines.

Since pressure drag accounts for the vast majority of the total drag acting on a bluff body object, reducing the magnitude of the pressure drag is the best solution towards lowering the total drag experienced by the bluff body [57, 53]. A means to accomplish this is to shrink the size of the low pressure region in the wake of the object. A reduction of the wake itself is needed in order to achieve this shrinking [24, 22, 37, 29, 64, 63, 28]. Introducing the bluff body into a turbulent flow, as seen in Figure 2.1, is able to narrow the wake behind the object by moving the separation point where the flow is no longer attached to a more downstream location. The impact of this point movement is clearly seen with a change in drag coefficient from 1.2 down to 0.3. While it maybe true that the frictional drag is greater for the object in the turbulent flow since more surface area comes in contact with the flow, the object being a bluff bodies makes pressure the dominant drag force meaning the total drag for the object to the right will be lower than the object to the left [2, 40].
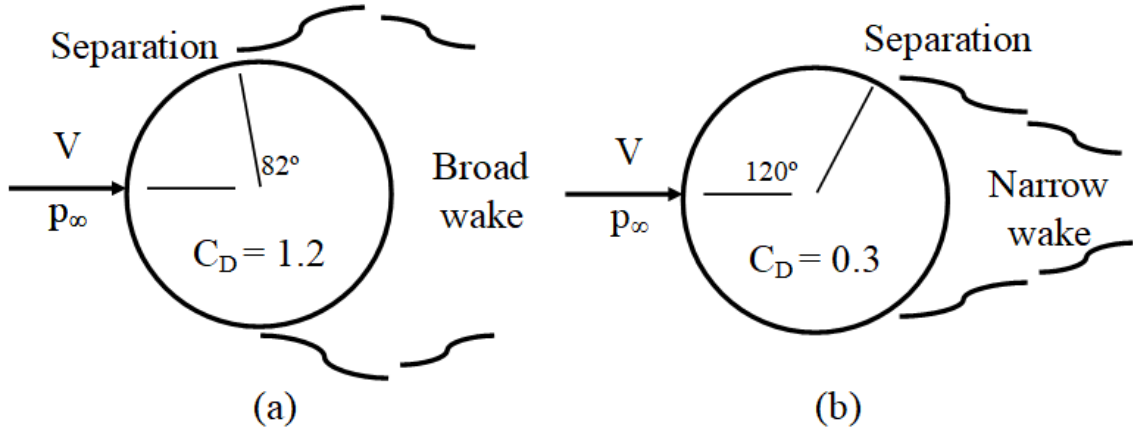
Figure 2.1: a)Cylinder Laminar Flow b)Cylinder Turbulent Flow [34]

2.2.1 Quasi-Steady Flow Assumption

The quasi-steady aerodynamics assumption provides an ideal simplification to represent complex quasi-steady variations into periodic problems. When the requirements of this assumption are met the forces and moments acting upon a body are defined to depend solely on the instantaneous motion acting on the body's surface at that exact moment in time [39]. Continuous measurements are therefore possible to be recorded that are not time impacted by the history of the wake or vortex shedding that may occur while a body is in rotational motion. The assessment if a given problem is able to use the quasi-steady aerodynamics assumption makes use of the reduced frequency parameter. This dimensionless parameter characterizes the degree of unsteadiness observed in a problem. The formula of reduced frequency is provided by Eq. 2.1 below. A reduced frequency of exactly zero is classified as steady-state aerodynamics, $0 < k \leq 0.05$ meets the quasi-steady aerodynamics limit, and $k > 0.5$ are classified as unsteady aerodynamics. The reduced frequency range of the sphere and cylinder for the set of test cases conducted all fall within the needed range to be classified as a quasi-steady assumption. This ranges from $3.0x10^{-4} - 7.0x10^{-3}$.

$$k = (\omega * b)/V \qquad\qquad (2.1)$$

2.3 Cal Poly Low Speed Wind Tunnel

A report conducted by students after the most recent refurbishment of the LSWT, shown below in Figure 2.2, indicates a velocity deviation from the average cross-sectional area of the test section to reach a maximum of 2.5 percent deviation approximately 5 inches off of the test section floor. Any testing within the LSWT should consider this when determining placement of test objects. The turbulence intensity indicated less than 0.5 percent for the vast majority of the test section. A small region located at the top center of the test section where this value reached a high of 2.5 percent [65]. As the wind tunnel test section is substantially larger than these two regions of identified flow irregularity, the LSWT sees itself as an ideal candidate for this project of CR implementation.
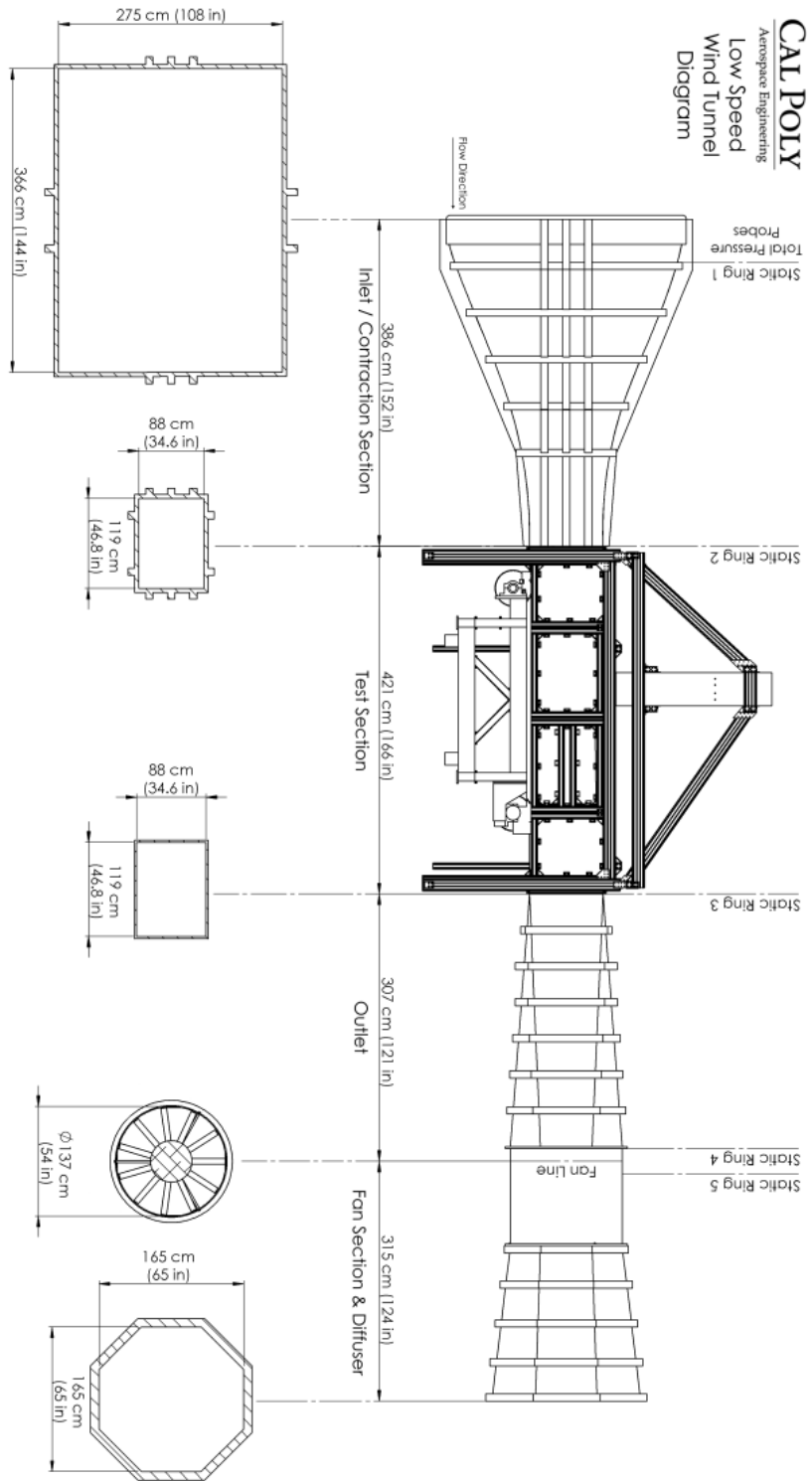
Figure 2.2: Cal Poly Low Speed Wind Tunnel Diagram [65]

Chapter 3

PRIOR WORK

3.1 Traditional Force Balances

A problem that has plagued the force measurement of bluff body test objects within wind tunnels has historically been linked to preference of streamlined test objects taking the primary focus [15]. This testing of bodies with streamlined characteristics has influenced the design process and focus of force balances over the past century of wind tunnel testing by engineers [49, 20, 70]. In a typical test run, the body of interest is often characterized by a higher lift-to-drag ratio over a reduced range of attitude. It is also common in these tests that the drag coefficient, which is based on the cross-sectional area of the test object, is on the order of 0.1 or lesser values. The issue of drag channel sensitivity then is made a concern since the airload range is 1 to 2 orders of magnitude lower than that of the lift forces. This makes testing of larger bluff body models using this force balance method impractical since the drag coefficient raises to an order of 1 and unsteady loads are likely to occur [34, 26, 45].

This leads to the challenge of measuring smaller drag forces at a high enough accuracy when a much larger lift force is simultaneously acting on the object of interest. As discussed previously, bluff bodies may be exposed to substantial forces from all 6 components of loading at an arbitrary attitude that can undergo dramatic shifts in the magnitudes to each individual component with minimal shifts to the attitude towards the freestream. The focus of mapping the complete loading for a bluff body object therefore will require a measurement technique that is capable of producing accurate measurements across multiple axis at the same time. This disqualifies traditional

wind tunnel force balances for the scope of this project [73, 66, 48]. An advancement that offers the development for a solution to this issue comes in the form of 6-DOF load cells [74]. The progress of commercially available models, some of which that are already within the possession of the Aerospace Engineering department here at Cal Poly, offer an affordable means for aquiring these measurements.

3.2   6-DOF Load Cell

6-Degrees of Freedom (6-DOF) load cells has emerged as solution to designing a simplified force balance system with the capability of measuring a wider range of forces and moments acting on a test body to an acceptable degree of sensitivity. An expected frequency response range of below 100 Hz is achieved through public accessible models [74]. While point-to-point consistency is achieved at a high precision level for a single test, these load cells can be susceptible to interactions and interference between the axes of the load cell. This interaction can increase the difficulty of repeatability for a given test. This issue can be avoided through multi axis calibration [34].

Another aspect of the 6-DOF load cell that makes it a prime candidate for the proposed implementation at the current wind tunnel testing capabilities, at not only Cal Poly but promising number of private and public wind tunnel facilities, is their growing availability within the consumer market. The growing development within this consumer sector of 6-DOF load cells has also lead to more sophisticated and miniaturized models that are able to meet the precision desired with a smaller sized balance system [9]. The smaller size of load cell available has therefore increased the practicability of the Continuous Rotation Technique as developed at Georgia Tech as the smaller size better lends itself to the sweeping axis rotation necessary in the technique. This will provide the benefit of a simplification for a mounting setup.

3.3 Prior work from Georgia Tech

The following section will serve to explain the work that has been done by researchers at Georgia Tech to create the measurement system for bluff body load maps that is proposed for implementation within the Cal Poly wind tunnel. Through the use of the Continuous Rotation Technique developed by the researchers, the load maps of over 40+ models across all necessary axes have been collected and verified. These load maps collected were further simplified by a Fourier series to represent the 6-component load coefficients. Interpolation of these Fourier coefficients were then considered for approximating load maps of more complex bluff body objects such as cars or engine canisters [44].

3.3.1 Continuous Rotation Technique

The Continuous Rotation Technique was developed at Georgia Tech to serve as the solution for obtaining bluff body force and moment measurements at a high enough resolution to fully detail a loading map of any arbitrary attitude in a time frame that is reasonable for wind tunnel allocation. To accomplish this the support of the model is placed on top of a stepper motor. The stepper motor is in turn attached to the 6-DOF load cell. The reactions that are exerted upon the load cell from the stepper motor have been found to provide an accurate means of measuring the aerodynamic loading upon the test object. This is supported through measurements taken of the azimuth-resolved drag forces acting on a rotor hub [25].

A stepper motor of sufficient sophistication can rotate the model at speed slow enough to assume a quasi-steady load measurement with the rotation rate of the body treated as stationary. This allows for the dismissal of concerns about asymmetric flow separation as a result of the rotation rate [23, 21]. At this slow rate of rotation, the stepper motor can be set to azimuthal steps of 0.1 degrees or smaller achieving much higher resolution as opposed to steps of 15-degrees as discussed in traditional setups requiring several wind tunnel startups and shutdowns to access the test section for manipulation of fixed mount systems. The stepper motor mount also provides the ability for multiple rotations over a time required to reach statistical stationarity of measurements with fine fluctuations. In the setup as produced at Georgia Tech this balance system was able to obtain all 6 components of loads at 1-degree of azimuth resolution in a 10 minute span [26, 35, 34, 27].

Static measurements were performed at discrete azimuth angles to show statistical in-variance with the airloads obtained from CRT. Using the aspect ratio 1 cardboard cylinder, a series of fixed angle measurements were taken for the drag forces acting on the cylinder at a given Reynolds number range. After taking these different fixed point measurements, the Continuous Rotation Technique utilizing a 0.99 rpm was performed across a complete range of attitudes covered by the fixed point measurements. These results were then overlaid and displayed in Figures 3.1-3.3.
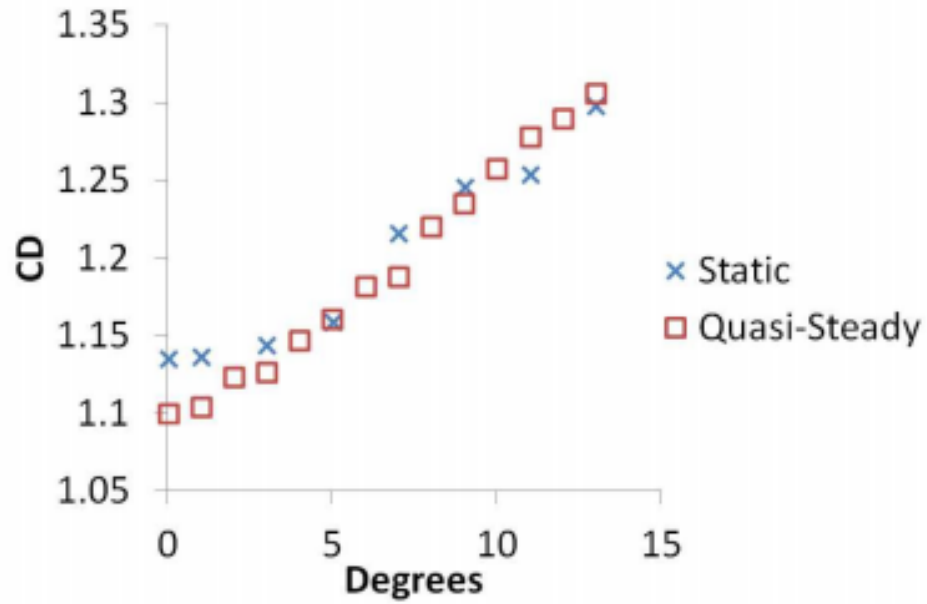
Figure 3.1: Drag Coefficient variation over azimuth angles showing comparisons with discrete static angle measurements performed at Georgia Tech wind tunnel [34]
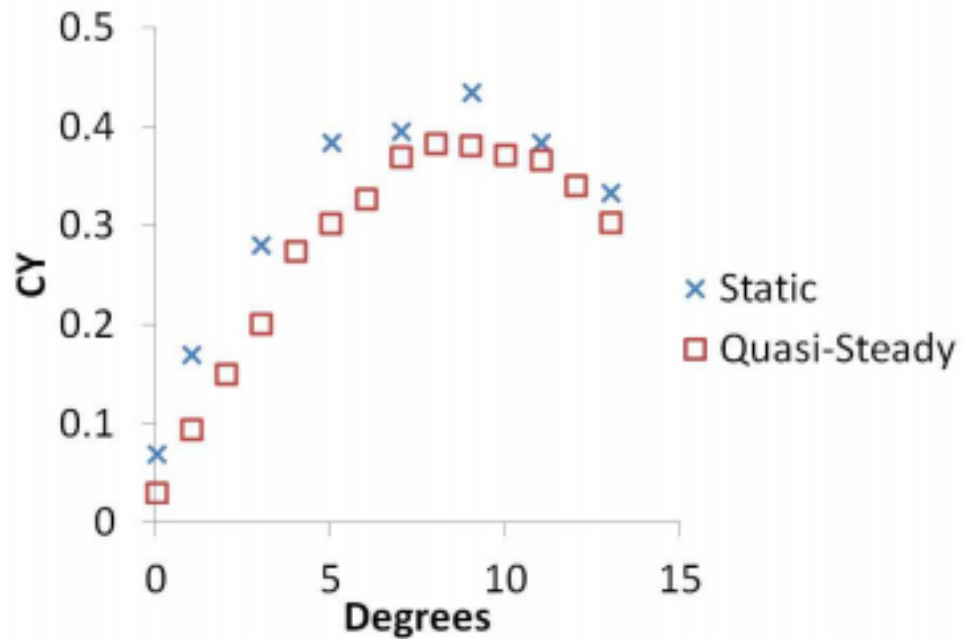
Figure 3.2: Side Coefficient variation over azimuth angles showing comparisons with discrete static angle measurements performed at Georgia Tech wind tunnel [34]
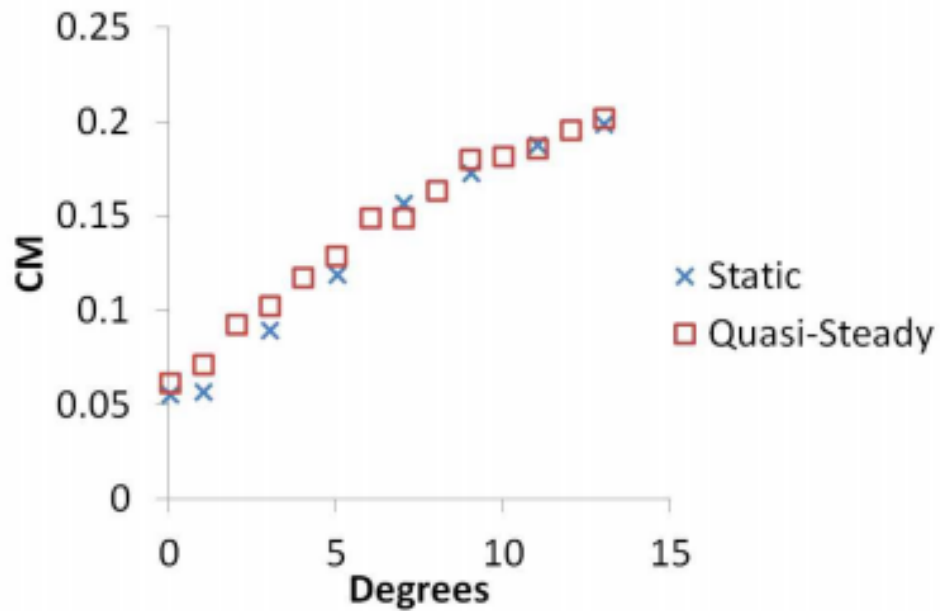
Figure 3.3: Torque Coefficient variation over azimuth angles showing comparisons with discrete static angle measurements performed at Georgia Tech wind tunnel [34]

When comparing the quasi-steady measurements to the fixed static ones a level of uncertainty have been reported that met the expected behavior at that Reynolds number range. This is due to the 3-dimensional separation lines and their tendency to remain attached at some flow conditions. This behavior is not possible to exactly repeat from one test to another. Since the uncertainty between the quasi and static measurement matches the anticipated levels, this validates the expectation that a slow-rotating body will not cause any inconsistency or impact the flow field in any noticeable or meaningful way. This validation supports this CR as an alternative means of taking static measurements for a given test body.

3.3.2   Fourier Series

The variation of each 1-degree location along the azimuth resolution are cataloged as 20-term Fourier series. This process of converting experimental measurements to a discrete Fourier representation has been commonly used in various wind tunnel data sets [42]. The rotation rate of the stepper motor is treated as the fundamental frequency of the transformation. For the tests run at Georgia Tech, the Fourier series was truncated following the 20th complex term. These were verified by overlaying with the original data file to ensure that no substantial peaks or valleys were being lost from the original data set to the Fourier series. In cases of sharp features more terms were reported with some cases requiring up to 50 terms in extreme cases. When implementing this technique at Cal Poly validation will be needed to confirm that 20 complex terms will be enough to match level of precision as seen at Georgia Tech or if more terms will be required [34]. The current work shows statistical similarities in airloads with the reported data. Cataloging airloads as Fourier Series coefficients is part of future work.

The process of converting measurements taken by the load cell into the truncated Fourier series begins by assigning a sample Block size N, a power of 2 for simple use of the Fast Fourier Transformation algorithm. The sampling period T is given in seconds by

$$T = 1/\Delta f$$

where the Nyquist Frequency is

$$f_N = N\Delta f/2$$

The Fourier series is utilized for interpolation of the data collected by the load cell. This is equivalent to a polynominal curve fit with coefficients being A_n and B_n.

$$y = \sum_{n=0}^{N} A_n Sin(2n\pi x/360) + \sum_{n=0}^{N} B_n Cos(2n\pi x/360)$$

Figures 3.4-3.6 show a reported comparison of truncated Fourier series to original load variations over a single rotation of an AR 1 circular cylinder. It is worth noting that the test object is not required to be perfectly symmetric between the two hemispheres along the length of the profile. This is seen with the measurements of the second half of the cylinder having different load variation than when compared to the first 180 degrees. This asymmetry is to be expected given that the test object for this validation was constructed from cardboard tubing. The presence of the asymmetry in the graphs between the first 180 degrees of the rotation to the second 180 degrees shows this technique is able to accurately represent this variation.
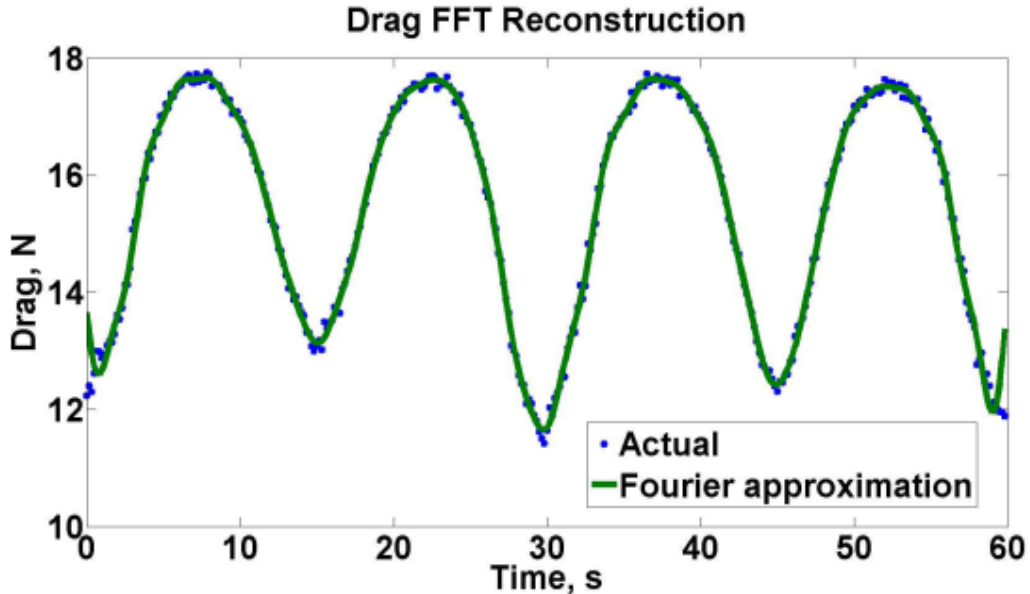
Figure 3.4: Drag force variation for an aspect ratio 1 circular clyinder over azimuth angles showing comparisons with Fast Fourier Transformation approximation performed at Georgia Tech wind tunnel [34]

22
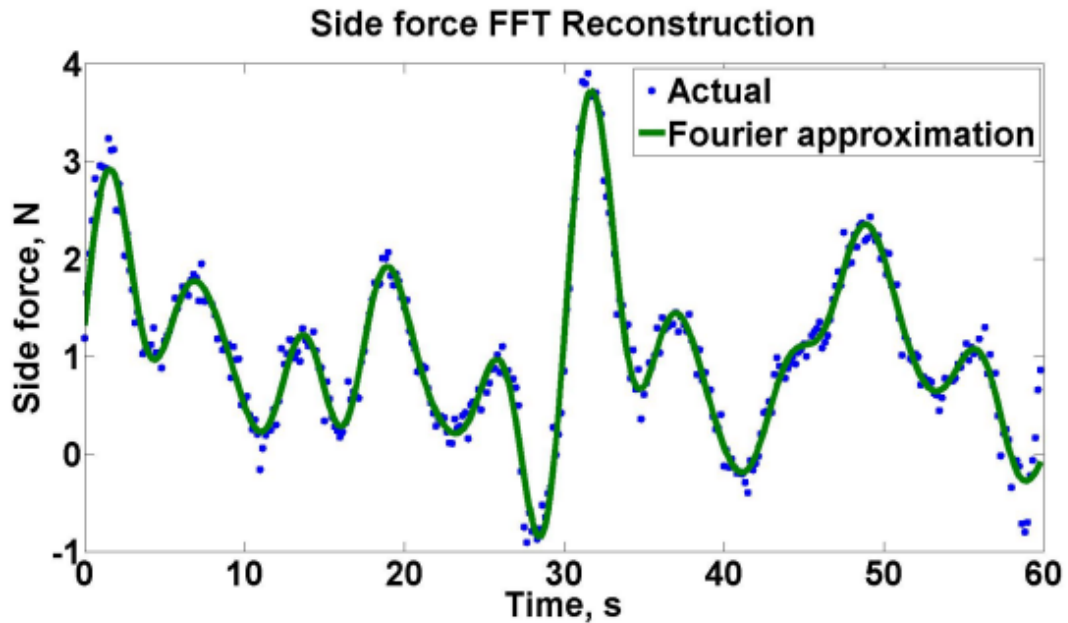
Figure 3.5: Side force variation for an aspect ratio 1 circular clyinder over azimuth angles showing comparisons with Fast Fourier Transformation approximation performed at Georgia Tech wind tunnel [34]
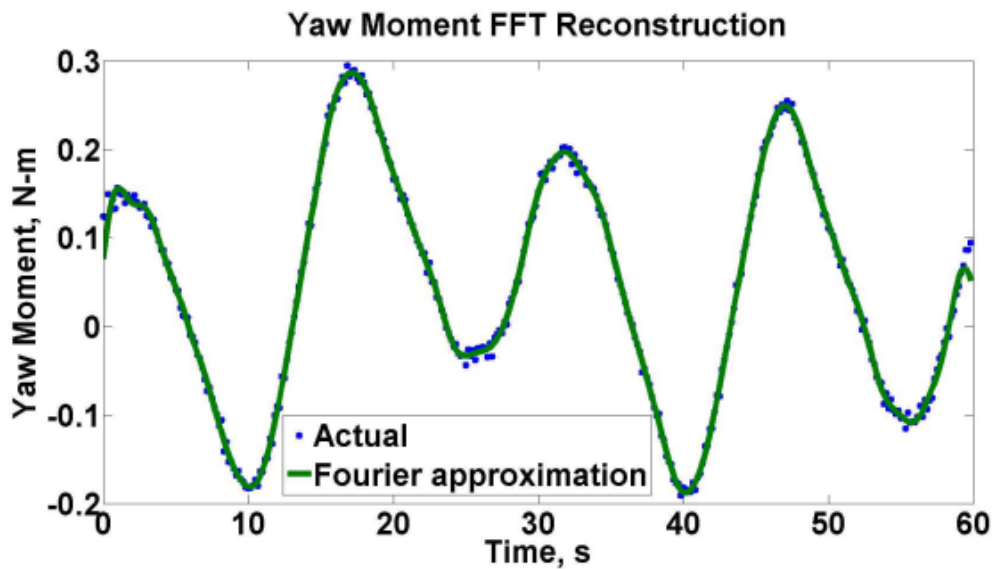
Figure 3.6: Yaw moment variation for an aspect ratio 1 circular clyinder over azimuth angles showing comparisons with Fast Fourier Transformation approximation performed at Georgia Tech wind tunnel [34]

3.4 Georgia Tech Implementation

3.4.1 John J. Harper Wind Tunnel Memorial

The wind tunnel testing done by the research group at Georgia Tech was performed within the John J. Harper Low Speed Wind Tunnel in Atlanta (277.4m above standard sea level). The tunnel is a closed-circuit system powered by a 600-hp dc motor powering a blower fan shaft configuration capable of a top speed of 32.2 m/s [59]. When the tunnel is provided with a cleaned and empty test section a freestream turbulence intensity of 0.04 percent is present.The test section of the wind tunnel is contained within a 2.74m diameter cylindrical tube with flat floor and ceiling allowing a clear height of 2.13m. A scale model version of the John J. Harper wind tunnel is provided in Figure 3.7 to better illustrate its configuration setup. Expected blockage was reported to be $3 - 5\%$.
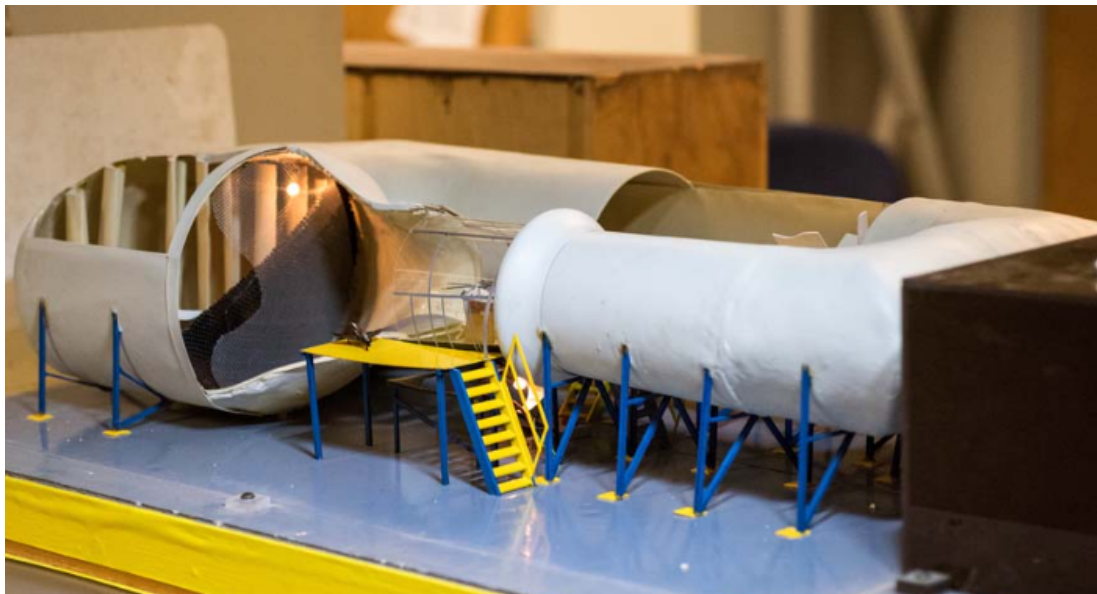
Figure 3.7: Scaled model of the closed-circuit John Harper Wind Tunnel Memorial powered by a 600-hp dc motor capable of reaching test section speeds of 32.2 m/s located at Georgia Tech [34]

3.4.2 Wind Tunnel Comparison

It becomes apparent when comparing the size of the wind tunnel and test section at Georgia Tech to the wind tunnel present at Cal Poly that a much larger system was present for this project when it was initially developed at Georgia Tech. A representation to the size disparity is shown in Figures 3.8 and 3.9 showing images of Georgia Tech's slow speed wind tunnel and the low speed wind tunnel at Cal Poly.

Given the sizable difference between the two wind tunnels it can be expected that wall interference will play a larger role when implementing this force measurement technique within the Cal Poly wind tunnel than it had been in the project at Georgia Tech. The steps that will be taken to account for this increase of interference will be explored in section 4.1.1. An advantage that will be present for the testing done at Cal Poly opposed to the original site at Georgia Tech is the presence of a fan location. The closed-circuit design at Georgia Tech involves the fan upstream to the test section blowing the air towards the body of interest. The turbulence from fan blades thus requires a more extensive series of flow straightening apparatus to create a smooth freestream. The Cal Poly wind tunnel has the fan placed downstream of the test section pulling air through the system without imparting turbulence to freestream moving through the test section.

Figure 3.8: Former Ph.D. researcher Nandeesh Hiremath entering the main diffuser section of John Harper Wind Tunnel Memorial near the tunnel's four blade driven fan powered through a World War II Curtis bomber propeller hub [34]
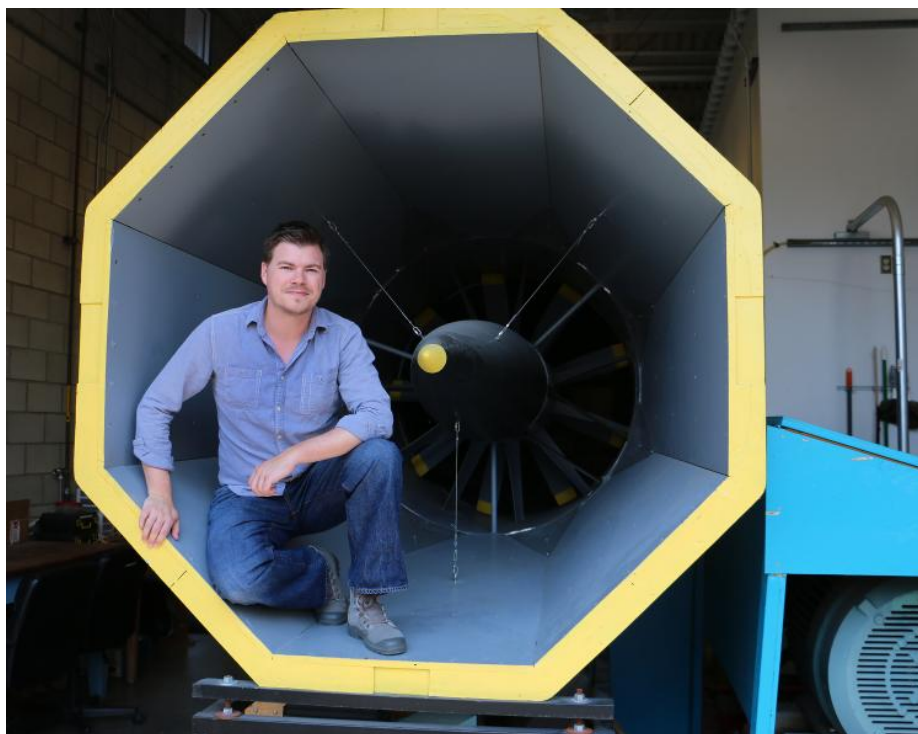
Figure 3.9: Graham Doig kneeling inside the outlet section of the Cal Poly Low Speed Wind Tunnel just beyond the driver fan assembly aiding in the size comparison between the facilities offered at Georgia Tech than that available at Cal Poly [3]

3.4.3 Georgia Tech Testing Rig

The setup developed at Georgia Tech, was made up of a long cylindrical rod to support the body at a height within the wind tunnel where support interference effects was negligible. When support interference reaches a small enough magnitude, it can be accounted for with superposition through subtraction of tare readings made without the test object attached to the mount. A balance must also be reached between the length of the support rod and the limit of airspeed or Reynolds number available for a test. As the rod used to support the model increases in length there is a reduction to the support interference experienced by the model. This length also will impose a larger pitching moment on the load cell as dynamic pressure increases thus restricting the speed at which tests can be performed or require a reduction of model size to accommodate. A 12-inch support rod length made of stainless steel was determined to meet the negligible demands for support interference up to the desired velocities for a AR 1 cylinder.

The support rod is then attached to a micro-stepping enabled stepper motor. To measure the reactions on the stepper motor the 6-DOF ATI Industrial Automation Gamma load cell was utilized. The load cell measurements on the reactions of the stepper motor from the body were proven to be an accurate measurement of the loading of the test object. A rotation rate of 0.99 RPM was used to achieve the quasi-steady load measurements that the Continuous Rotation Technique requires. A total of 10 revolutions were used to provide statistical stationarity at each of the azimuth increment steps along the full 360-degree resolution. The deciding factor for the number of rotations necessary was to minimize the impact of unsteadiness present within the John. J. Harper wind tunnel. This number would be unique to any given wind tunnel as it is associated with freestream turbulence, and attainable Reynolds numbers. A task for applying this technique to Cal Poly's wind tunnel

requires analysis and validation on the necessary number of revolutions per second for accurate ensemble averages, ensuring quasi-steady conditions. An illustration of the mounting system is included in Figure 3.10. Here the test object is shown to be mounted atop the mounting rod with the testing rig as a whole oriented perpendicular to the oncoming flow of the air. In this setup the testing rig being fully enclosed within the test section results in loading acting on all components, including the stepper motor and load cell obstructing the freestream.
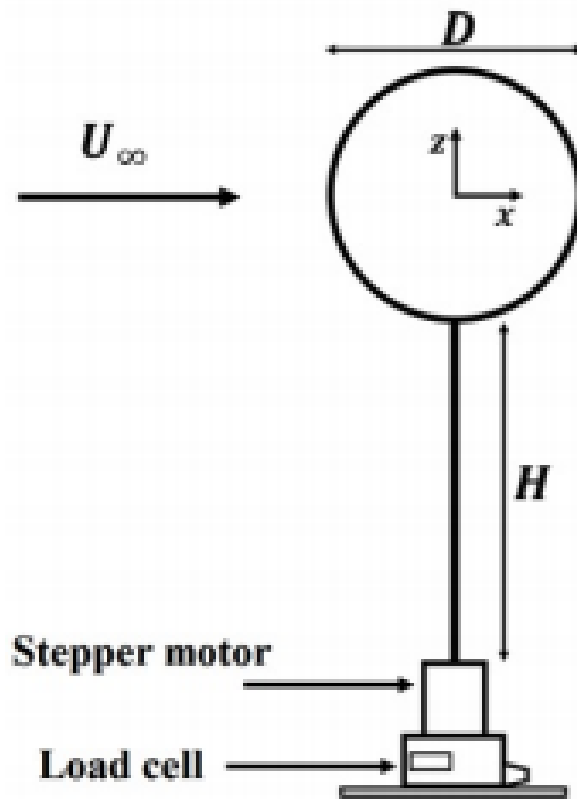
Figure 3.10: Schematics of the testing rig assembly consisting of load cell, stepper motor, and supporting rod used for CRT measurement for test bodies within the John Harper Wind Tunnel Memorial at Georgia Tech [52]

The 10 rotations at 1 RPM allows for a complete azimuthal load map to be performed on a given test object in a matter of minutes. This is a drastic time saving operation than traditional fixed mount measuring techniques that involve no manipulation of the model attitude during a single test run, and often at a less fine resolution. A faster method of collecting aerodynamic loading gives end users the ability to test the same object over multiple axes. In the case of work done by the researchers at Georgia Tech, the vast majority of bluff bodies were found to capture all necessary features for slung load divergence speed prediction using periodic interpolation from data sets of 3 or less axes. The selection of the axes was based on symmetry of the object as a means to simplify the data sets given that an infinite amount of axes are possible. Included in Figure 3.11 is an example of axes selection based upon symmetry of a Humvee.

The stepper motor that was used to perform the rotation of the test object had a step resolution of 200 steps/revolution. To further increase the the refinement of the step size the stepper motor was driven using an NI motion controller - nuDrive. This was capable of allowing micro-stepping to be taken at a 10x improvement thus a resolution of 2000 steps/revolution. This comes at the loss of holding torque. In the tests run at Georgia Tech, Reynolds numbers of 300,000 and above were able to have the stepper motor maintain the desired rotation speed [34].
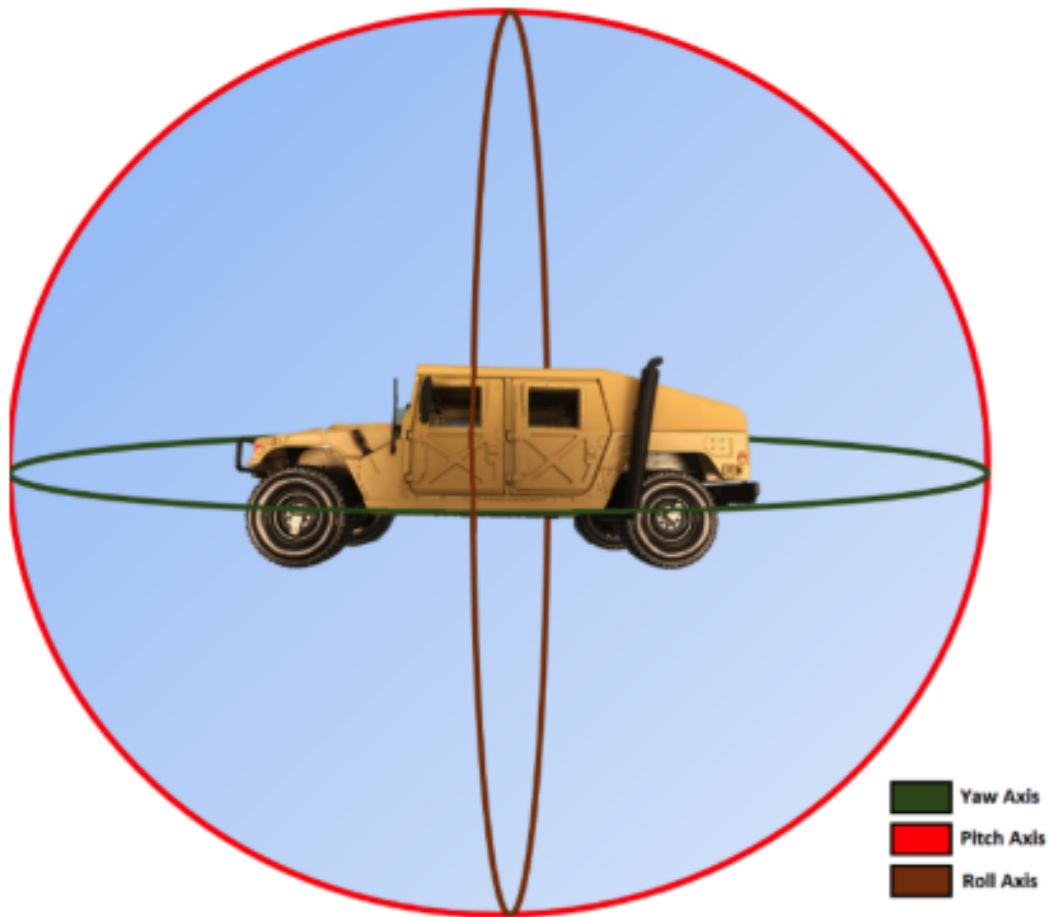
Figure 3.11: Axis selection consisting of yaw, roll, and pitch for a scaled model of an all-terrain Humvee vehicle for the purpose of determining axis of rotation to fully capture the airloads acting on the object using CRT in John Harper Wind Tunnel Memorial [43]

Chapter 4

EXPERIMENTAL METHODS

The focus of this thesis paper will now shift to the work that was done to implement a CRT testing rig within the infrastructure of Cal Poly. The process for sizing and selection of test bodies that would be used to validate this initial test rig and determined and their fabrication is discussed. A detailed look into the components that make up the system are included to demonstrate the progression of the system as developed at Georgia Tech to a feasible system within our facilities. Complications of this adaptation are identified and discussed. This chapter will then move on to covering the design and fabrication of an optical encoder system for purpose of slippage monitoring and general improvement upon Georgia Tech implementation. A set of testing procedures are developed along with a testing matrix to examine the final testing rig's ability to capture reliable airload measurements. Subsequent chapters with explore and quantify both sources of error and uncertainty of those testing results and provide comparison of CRT to a static measurement configuration.

4.1 Test Setup

This section will focus on the physical components required to implement a functional CRT testing apparatus. The process of test body selection is detailed to provide confidence that proper and insightful test objects have been selected that will offer clear results for analysis and comparison to expected trends identified from Georgia Tech's prior work. Hardware used in the test rig are included with explanations of physical interfaces between components as well as software interfaces creating the proper motion required for this type of testing. Topics on the incorporation of an encoder system are to be discussed within section 4.2 to emphasize its differing approach to that at Georgia Tech.

4.1.1 Test Body Selection

The process of test body selection was primarily driven by prior work conducted by an undergraduate researcher who had started initial work for this project by designing and manufacturing the general housing of the CR assembly and mounting rods [17]. Specifically for the case of the mounting rods, attention was needed to capture expected deflection of these rods when placed within the wind tunnel freestream with a test object. A limit of 1-degree of rod deflection was set and paired with a mounting rod length of 0.4572 meters. This provides ample clearance to place the test bodies in question as close to the center of the test section cross-sectional area as possible. The 1-degree allowed deflection of the mounting rod stems from the nature of expected future test objects to have characteristics in their geometry that result in significant change of all loading components with only subtle attitude change. For the purposes of a sizing assessment of the test objects, Eq. 4.1 demonstrates how drag force is deduced. A Drag Coefficient of 1.3 is used to align with empirical results for a circular

cylinder placed perpendicular to the flow. A set of two inertia are then found for a set of two steel mounting rods of diameter 10mm and 15mm through use of Eq. 4.3 that when paired with a span of test section velocities results in a value of rod deflection, Eq. 4.4, which can be compared to the maximum allowable deflection of Eq. 4.2.

$$F_{st} = 0.5 * \rho * V^2 * A * C_d \tag{4.1}$$

where F_{st} = Force on steel rod (N),

ρ = Fluid density (kg/m^3),

V = Fluid velocity (m/s),

A = Projected Area (m^2),

C_d = Drag Coefficient

$$d_{st_{max}} = L_{st} * tan(1°) \tag{4.2}$$

where $d_{st_{max}}$ = Maximum steel rod deflection (m),

L_{st} = Length of steel rod (m)

$$I_{st} = (\pi * (r_{st}^4))/4 \tag{4.3}$$

where I_{st} = Steel rod second moment of inertia (m^4),

r_{st} = Steel rod radius (m)

$$d_{st} = (F_{st} * L_{st}^3)/(3 * E_{st} * I_{st}) \tag{4.4}$$

where d_{st} = Steel rod deflection (m),

E_{st} = Young's Modulus of steel (Pa)

As will be discussed in section 4.1.3, the load cell used in this project expects a much higher force for its sensing range then could be achieved with any test object these mounting rods could support without exceeding the deflection limit. This made the thicker mounting rod the focus for sizing an AR1 circular cylinder test object as it would support the largest body while still remaining under the 1-degree rod deflection over the entire operating range of wind tunnel speed at a max speed of 40 m/s. The AR1 was determined to be the most logical primary test object due to its extensive testing in two/three-dimensional flows as both computational and empirical studies [36, 14, 38, 61, 32, 18, 55, 12, 41, 72]. The choice was made to purchase a PVC Pipe and manufacture end caps to create this closed cylinder test object. An 8.65 inch pipe was purchased because of anticipated clearance of mounting rod deflection as shown in Figure 4.1. The size results in max blockage of 5%.
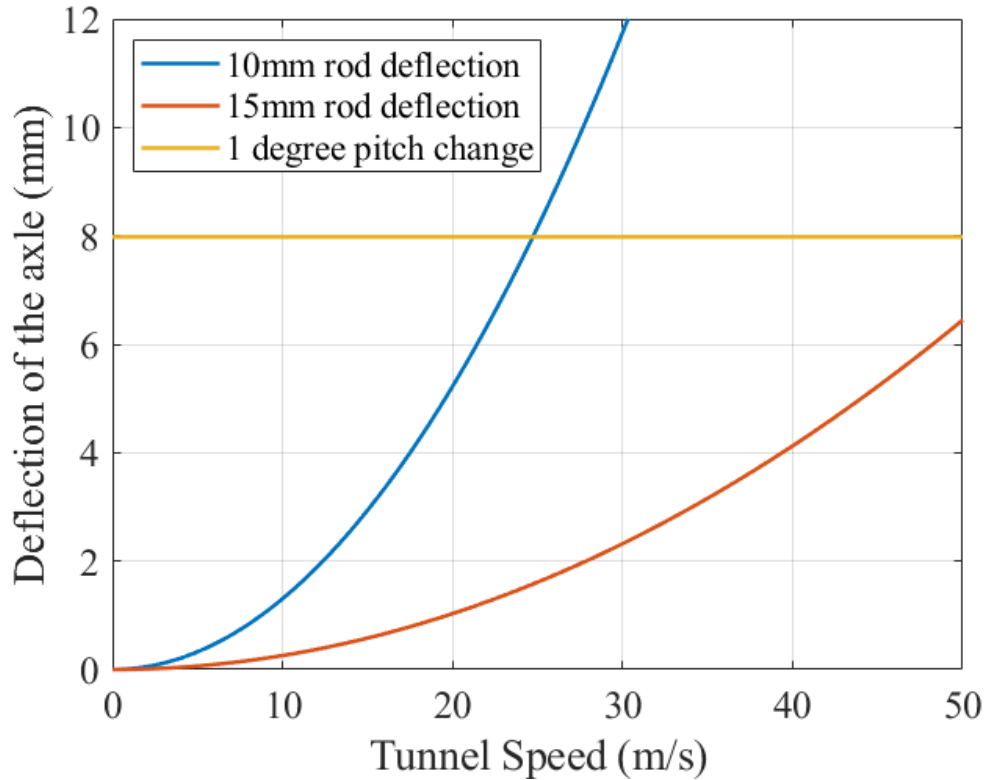
Figure 4.1: Anticipated quantity of steel mounting rod deflection compared to required deflection for 1-degree pitch change for 10mm and 15mm diameter cases for complete span of Cal Poly Low Speed Wind Tunnel speed range assuming projected area of 8.65" aspect ratio 1 circular cylinder oriented perpendicular to flowfield with Drag Coefficient value of 1.3

Figures 4.2 and 4.3 show how these expected loads acting upon this test object compare with the maximum load sensing range as provided from ATI Mini58 datasheet. The drag force that is anticipated falls below the sensing range of the load cell. The impact of this in the terms of uncertainty of the CR testing rig in its current phase of implementation will be discussed later in section 5.2.2. The maximum sensing range of torque is exceeded for this test object at wind tunnel speeds passing 36 m/s. Testing of this project did not explore regions above 75 percent wind tunnel power thus the later regions of Figure 4.3 weren't considered.
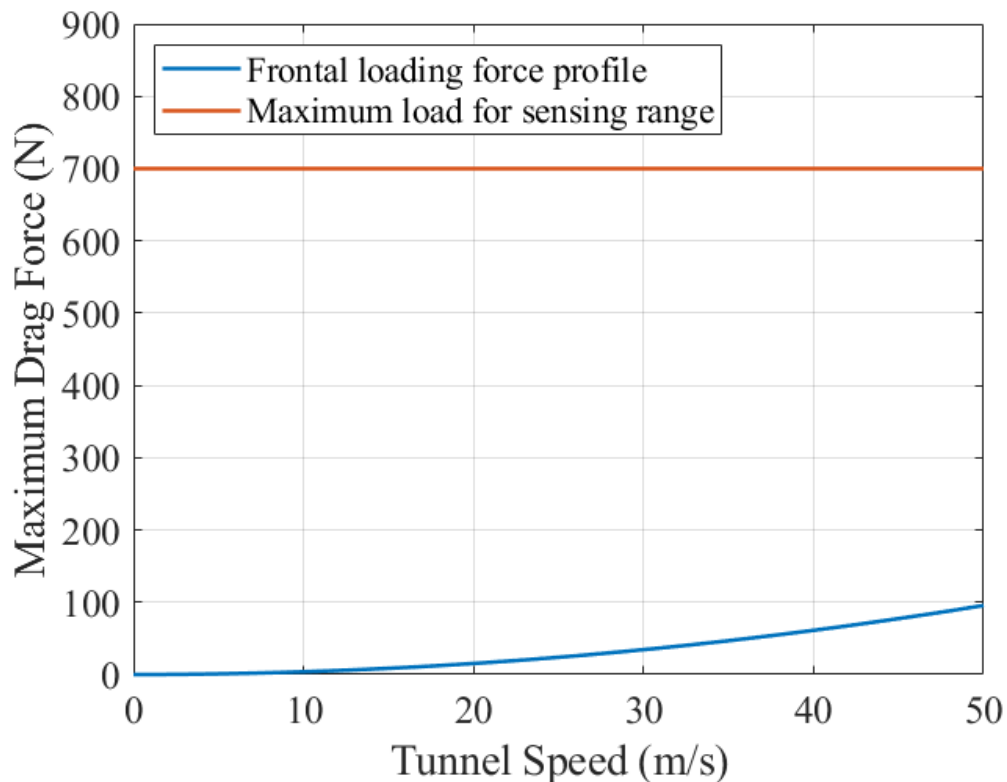
Figure 4.2: Anticipated drag force with steel mounting 15mm diameter for complete span of LSWT speed range assuming projected area of 8.65" aspect ratio 1 circular cylinder oriented perpendicular to flowfield with Drag Coefficient value of 1.3 comparison to maximum sensing range of ATI Mini58 load cell

The end caps of the cylinder test object were fabricated from 1 inch wooden rounds. An additional set of rounds were cut and then split into a set of 8 pieces reassembling equal pieces of a pie chart. The tips of these pieces was cut to a flat face for weight mitigation and safety. The PVC pipe was cut to an aspect ratio of 1 using a band saw at the AERO Hangar and was placed face down on a level surface. The end cap round were then pushed through the opposite end of the pipe until flush with the level surface. Four of the cut rounds were then secured to the interior walls of the pipe using super glue. These provide support to the ends of the model when placed perpendicular to the flow of the wind tunnel. The end cap is then removed and the same process was repeated to the other opening. Once all round cuts were secured

to the interior wall the end caps were again placed flush to the face of the pipe and lightly secured with a small set of applications of super glue to the crease along the circumference. This is for greater ease of removal of end caps as it will be required when removing a test object from the mounting rod.
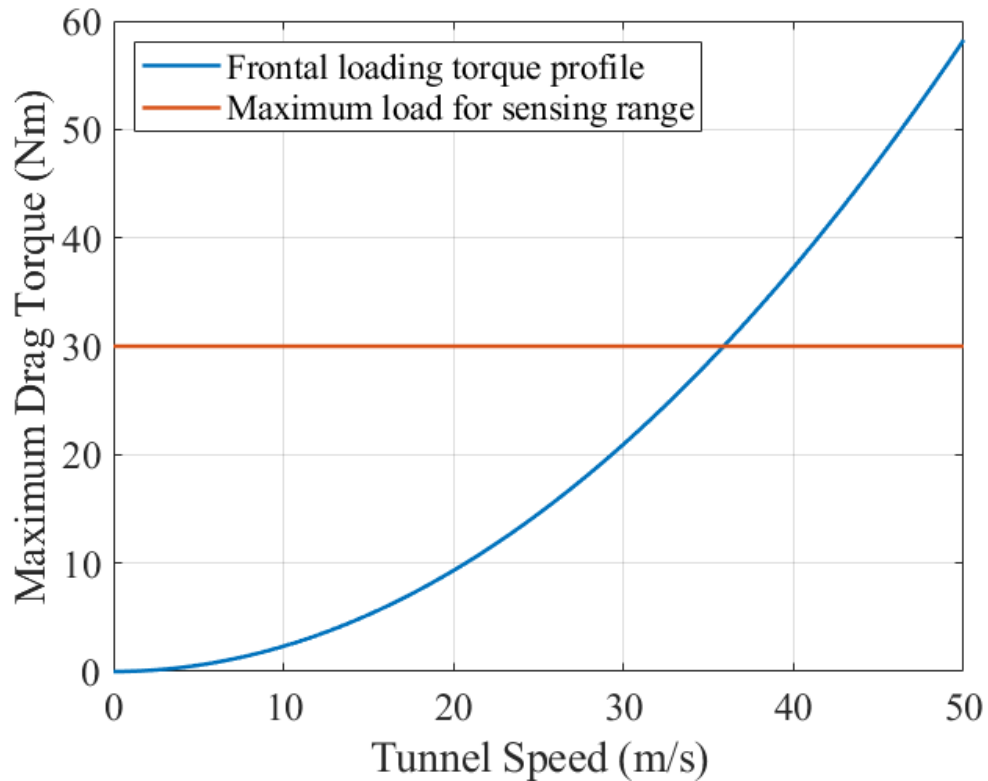
Figure 4.3: Anticipated drag torque with steel mounting 15mm diameter for complete span of LSWT speed range assuming projected area of 8.65" aspect ratio 1 circular cylinder oriented perpendicular to flowfield with Drag Coefficient value of 1.3 comparison to maximum sensing range of ATI Mini58 load cell

To provide additional testing of objects using this testing rig a sphere was selected. This was accomplished through purchase of a large 8-inch ball float valve. The benefits of this came as the body was already fabricated, which a sphere would prove a more difficult object to manufacture in-house, with a pre-threaded mounting interface. It was discovered during the process of finding a suitably sized float valve that all threads were done in imperial units. This would require an adapter to be made as both mounting rods utilized a metric thread. This was fabricated from a stock aluminum rod with the aid of a lathe machine. Included below are images of both the AR1 circular cylinder and sphere test object in Figures 4.4 and 4.5 respectively. The interface using for the attachment of the sphere to the mounting rod can also be clearly seen.
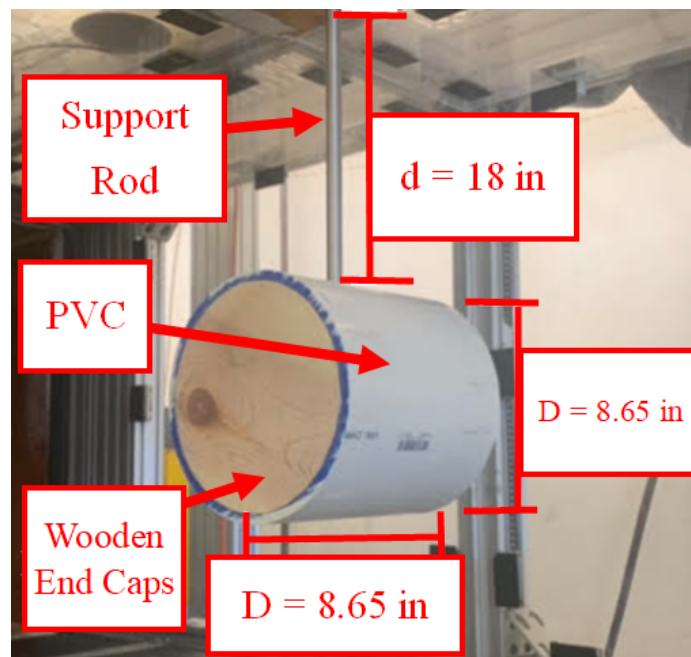
Figure 4.4: Aspect ratio 1 circular cylinder test object mounted for CRT testing with the Cal Poly Low Speed Wind Tunnel fabricated from a 8" nominal diameter PVC pipe and closed with cut and sanded wooden end caps secured with press fit and supper glue adhesive
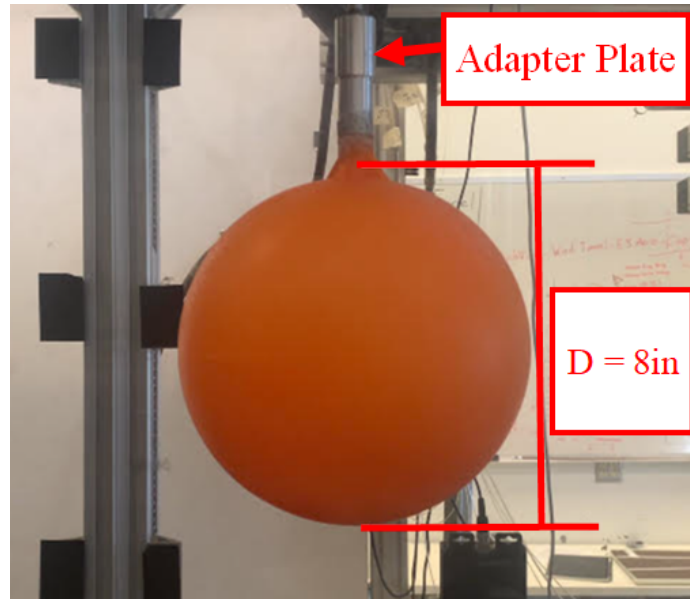
Figure 4.5: Sphere test object mounted for CRT testing with the Cal Poly Low Speed Wind Tunnel fabricated from a 8" diameter ball float valve secured to mounting rod by a metric to imperial thread adapter plate

4.1.2 Stepper Motor

The P series Nema 23 bipolar stepper motor was utilized for the test setup of the CR method at the LSWT. The specifications and visualization of the particular stepper motor are provided in Figure 4.6 and Table 4.1 as defined by the manufacturer [6]. Baseline operation of the Nema 23 with no guidance of a stepper driver provides a 200 steps per revolution actuation. The level of resolution for successful implementation of the CR technique relies on a smooth and continuous appearing actuation at low RPM rates. In reality, the actuation regardless of resolution is not a continuous motion but, instead a non-continuous disjointed series of a set number of steps over a complete rotation. Consider the motion of the hands of an analog clock. The hour, minute, and second hands all move a step at a time for a complete rotation around the face of the clock. If you where to look closely at the minute hand you would see the hand advancing with a series of clicks in a bopping fashion. Alternatively, looking at the second hands it is much harder to discern the non-continuous motion

than that of the minute hand. This would suggest the that either the second hand had a greater resolution than the minute hand or they possess the same resolution and a faster rotation rate creates a smoother actuation for lower step counts.

If the motion of the stepper motor was to be left in this disjointed state it would raise the concern that rotational effects were being created to an extent that the quasi-steady assumption that the CR technique requires would be violated and CR would not provide reliable data. A stepper driver, similar to the one shown in Figure 4.7, is used to perform micro-stepping. Micro-stepping is a feature provided by stepper drivers that allow for the steps per revolution value to be increased greatly beyond the default capability of the stepper motor in its baseline form. The increase of resolution allows for a smoother actuation to be achieved without changing the rotation rate of the stepper motor. The stepper driver of this project was increased to its maximum micro-stepping value of 25,000 steps per revolution allowing for the smooth actuation of the desired stepper rotation of 1 RPM for the majority of test cases to be run within the wind tunnel. This combination of step count and rotation speed allowed for the perceived continuous rotation required for the use of the quasi-steady flow assumption.

The communication between the Nema 23 and the DM542T driver is controlled through use of an open-source Arduino Uno micro controller. A C++ script written for the Arduino to read dictates the rotation rate of the stepper driver which in turn commands the stepper motor to actuate through the step count via a high-low digital pin reading. The process of the pin responsible for the motion of the stepper motor being set to high and subsequently to low allows for the stepper motor to advance one step count. The size of this step count being controlled by the switch settings of the stepper driver control. Changing the duration value of the delay that is conducted between the digital pin being set from high to low and the delay between pulses of

the digital pin allows for the RPM control for the stepper motor. A simple while loop repeats this process while a counter variable is incrementally increased with each step of the stepper motor. The duration of this while loop has the exit condition occur when the value of the integer variable tracking step count has reached the same value as the steps per revolution as set from the stepper driver controller. When this point in the script has been reached the stepper motor has completed a single rotation and thus so has the test object attached to the supporting rod.

Since CR method makes use of a series of rotations the reality is the Arduino script must allow for this while loop of stepper motor actuation to continue until the total number of desired rotations has been achieved. Simply increasing the exit condition for the step integer variable to be the number of steps per revolution times the number of required rotations would not be a possible solution given the high value of 25000 steps for a given rotation through the use of the stepper driver. If the exit condition of the while loop was set to the actual total actuations expected for a 10 to 12 rotation sequence of the stepper motor the value of the exit condition will quickly exceed the maximum integer value that the Arduino script is capable of handling. This overload of the parameter limit results in the script never reaching its exit condition and stepper motor failing to end its rotating motion after the number of needed revolutions has occurred.

The solution to this overloading issue comes by nesting the current while loop within a second while loop that is concerned with tracking the number of completed rotations during the test. Keeping the interior while loop as initially described, when the integer variable has reached the value matching the step count per rotation of the stepper motor the script exits the initial while loop. A new integer variable that is defined with the value of zero at the start of the script is then increased by one. The key of this script is then to redefine the value of the variable tracking step count back to its

starting value of zero. the exterior while loop then examines the value of the variable corresponding to revolution count. If the value is less than the desired number of rotations then the script will enter the interior while loop that actuates the stepper motor for another complete rotation. This process will continue until the revolution counting variable matches the inputted end condition for the while loop.
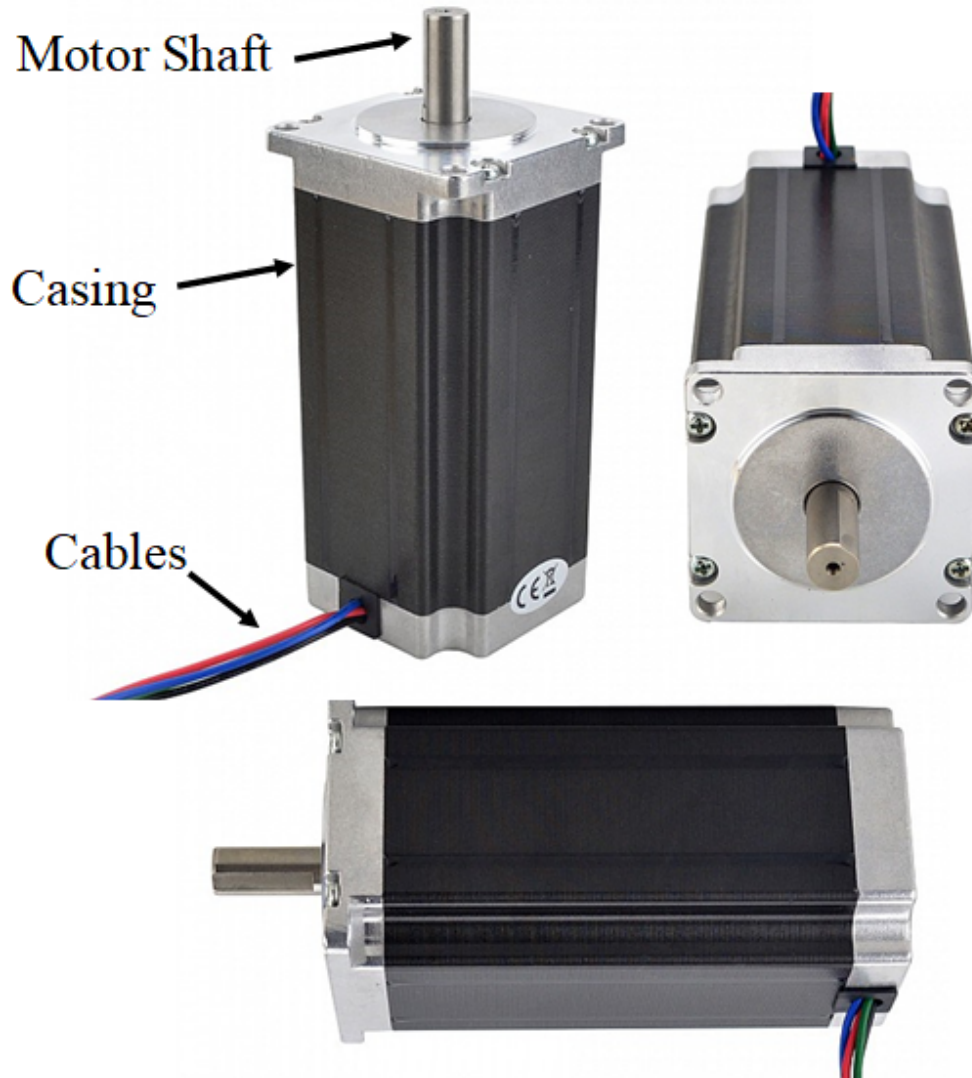
Figure 4.6: A set of views of the P Series Nema 23 stepper motor, manufacturer part number 23HE45-4204S, capable of 1.8-degree step size used as the stepper motor for rotation of test bodies for the CRT implementation within Cal Poly facilities [5]

Digital Stepper Driver

DM542T

PWR/ALM
PUL+
PUL-
DIR+
DIR-
ENA+
ENA-
ALM+
ALM-
SW8
SW7
SW6
SW5
SW4
SW3
SW2
SW1
GND
+Vdc
A+
A-
B+
B-

Current Table(Peak=RMSX1.4)

Peak	RMS	SW1	SW2	SW3
1.00A	0.71A	on	on	on
1.46A	1.04A	off	on	on
1.91A	1.36A	on	off	on
2.37A	1.69A	off	off	on
2.84A	2.03A	on	on	off
3.31A	2.36A	off	on	off
3.76A	2.69A	on	off	off
4.50A	3.20A	off	off	off

SW4: off=Half Current; on=Full Current

Pulse/rev Table

Pulse/rev	SW5	SW6	SW7	SW8
200	on	on	on	on
400	off	on	on	on
800	on	off	on	on
1600	off	off	on	on
3200	on	on	off	on
6400	off	on	off	on
12800	on	off	off	on
25600	off	off	off	on
1000	on	on	on	off
2000	off	on	on	off
4000	on	off	on	off
5000	off	off	on	off
8000	on	on	off	off
10000	off	on	off	off
20000	on	off	off	off
25000	off	off	off	off

VDC: +18V~+50V

Figure 4.7: Fully digital stepper driver, manufacturer part number DM542T-23HS45, developed with advance DSP control algorithm offering automatic idle-current reduction, over-voltage and over-current protections, soft-start with no jump in step when powered on, and micro stepping capability up 25,000 steps per revolution [7]

Table 4.1: P Series Nema 23 Specifications

Parameter	Baseline	Driver
Step Angle	1.8°	0.0144°
Steps per Revolution	200	25000
Holding Torque	3.0 N-m	3.0 N-m
Rated Current	4.2 A	4.2 A
Shaft Length	24 mm	24 mm
Shaft Diameter	10 mm	10 mm

4.1.3 ATI Mini-58 Load Cell

The ATI Mini58 6-DOF load cell was utilized for the Cal Poly implementation of the CR method within the LSWT facilities. The Mini58 load cell in particular, is a load cell that is designed by ATI to operate in a sensing range of forces and moments far exceeding the anticipated loading that is to be expected on the two test objects of this project for any of the given test conditions that can be achieved within the LSWT. Figure 4.8 and Table 4.2 found below, provide the specifications of this particular model of load cell [8]. The selection of this particular load cell for the current state of this project for the proof of concept for the CR technique to be shown within the smaller confines of Cal Poly's wind tunnel facilities was driven by both caution of department equipment during the early incorporation of the test rig and from available resources within the possession of the Aerospace Engineering department. The ATI Mini58 load cell was one of the load cells already available within the facilities at the LSWT thus, allowing for a faster incorporation of the CR test rig with existing Cal Poly infrastructure.

Table 4.2: ATI Mini58 Specifications

Mini58	Sensing Range	Resolution	Overload
F_x,F_y (N)	700	1/6	± 21000
F_z (N)	1700	7/24	± 48000
T_x,T_y (N-m)	30	9/1600	± 590
T_z (N-m)	30	1/320	± 800

Use of a load cell other than the Mini58 would require additional time and budget into the project to either fabricate an in-house load cell tailored to the testing ranges expected with the given test objects or the purchase of a different load cell of a lower range. A goal of this project is to expand the scope of testing within the wind tunnel that can be offered to students both in and out of the classroom. As such, a desirable trait of the testing rig for student use is that it operates in a manner that
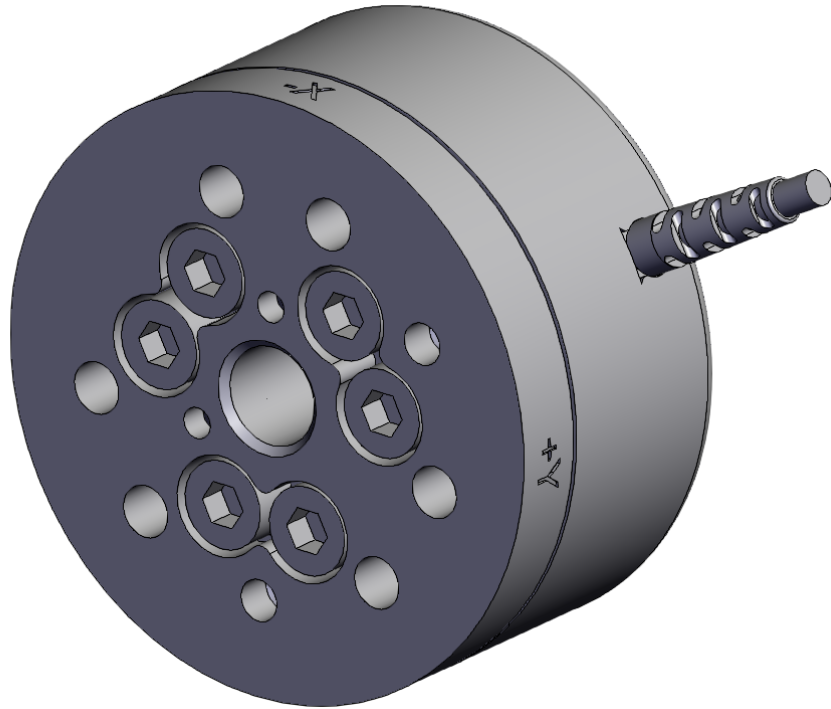
Figure 4.8: 3D CAD model of ATI Mini58 load cell used for CRT implementation in Cal Poly Low Speed Wind Tunnel [9]

allows students to confidently use the equipment and is forgiving to underclassmen that may improperly load or handle the load cell during the duration of a test run. This characteristic trait comes from the Overload value of the load cell. When the Overload value is exceeded in one of the 6-DOF the load cell may become damaged requiring repair for accurate subsequent measurements or complete loss of the unit as a whole. Such a load cell possesses far higher sensing range allowing the test setup to ensure that no students in the early stages of the CR implementation at Cal Poly will unintentionally push the load cell beyond its safe operating range. Since the current test objects in use of the CR test rig cannot reach aerodynamic load conditions that push the the ATI Mini58 load cell beyond its Overload values in any of the 6-DOF, even at maximum desired wind tunnel fan speed, it was an ideal candidate for this stage of the program.

The calibrated forces and moments acting upon the load cell is represented using Newtons and Newton-Meters, respectively. This is accomplished by the load cell interpreting the change in voltage that is experienced due to the presence of loading. This is determined by the ratio of measured voltage to the product of excitation voltage and the calibration factor unique to that model of load cell. A calibration file is provided to customers upon purchase of a load cell. As the ATI Mini58 was already in the department's possession, access to this file was available from the start of the project. Previous projects conducted within the LSWT that made use of the ATI Mini58 had already developed LabVIEW interfaces to obtain 6-DOF measurements using the relationship explained above, thus drag and side force are determined from Eq. 4.5.

$$F = F_{full} * V_{mea}/(V_{exc} * cal) \tag{4.5}$$

where F = Actual Force (N),

F_{full} = Fullscale Force (N),

V_{mea} = Measured Voltage (V),

V_{exc} = Excitation Voltage (V),

cal = Load Cell Calibration Factor

4.1.4 Labview Interface

Measurements that are collected initially from the load cell setup are in the form of analog measurements. These measurements are then converted to a digital form for transfer into the computer terminal to be recorded within the LSWT's LabVIEW interface. Figure 4.9 provides a diagram of the connection method utilized to facilitate

this data transfer process to the terminal. The included diagram comes directly from the ATI installation manual that is included with all transducer purchases. The method in question makes use of a DAQ power supply unit and DAQ Acquisition Card to create a connect link of the voltage change experienced by the load cell and provide a digital reading to LabVIEW to have that reading represented as a loading condition acting on the Mini58. The interface of the Cal Poly LabVIEW program for ATI load cell measurements then allows for the manipulation of the sampling rate to determine the given amount of data points that are to be collected for a given frequency input. The units of this input variable are given in the form of Hz. This in turn can be conceptually seen as samples per second. An example of this would be a sampling rate of 1000 Hz instructing the LabVIEW to collect 1000 readings from the load cell in the span of one second. The sampling rate then becomes a significant parameter for the collection of data for the various test conditions conducted using the CR technique. This is because as the body rotates, the sampling rate and rotation rate of the stepper motor will determine the amount of data points of each increment bin during the assembled bin averaging step of the CR post-processing.
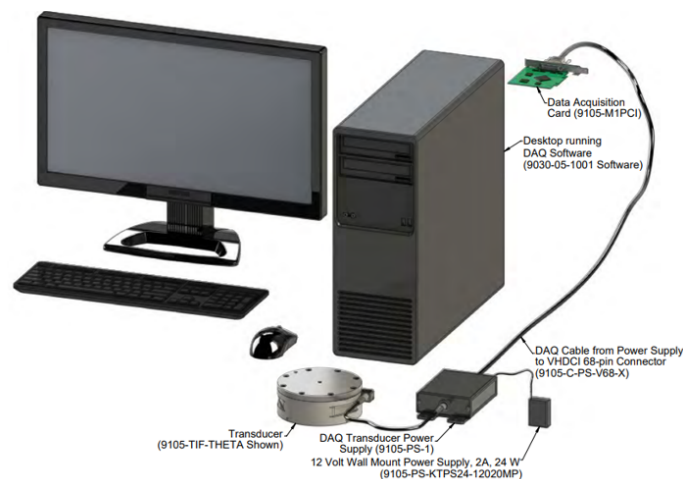
Figure 4.9: A schematic, provided in the manufacturer user manual, for installation setup of an ATI load cell transducer for capture on a desktop terminal consisting of the transducer powered by a DAQ power supply unit sending data to a Data Acquisition Card in computer terminal [9]

An important factor to allow for direct comparison between different rotation rates of the stepper and the resulting ability to capture the aerodynamic loading acting on the object compared to static readings was to ensure that any test collected using CR technique was to obtain the same number of data points per 1° azimuthal bin. If one test configuration utilizing a certain stepper motor rotation rate was providing a smaller number of data points per azimuthal bin then that particular test would experience a potential increase in measurement error of the final load map creating the false impression that it was a poor rotation rate for the CR technique than others. While this may be very well true in reality, the factor of data points per bin, number of samples per degree, must not be allowed to alter that conclusion. It was then necessary to determine what number of data points per azimuthal bin would allow for all tested configurations to be achieved with the given sampling rate range allowed by the LabVIEW program used. Two limiting conditions were identified that would aid in the selection of the needed sampling rates for the load cell.

1. It was found that if certain sampling rates were used within the input node of the LabVIEW interface the program would instantaneously fail as the program was not able to call and interpret measurements from the load cell at a speed fast enough rate as indicated by the sampling rate frequency. The upper limit of this instantaneous failure was found to be for sampling rates exceeding around 1100 Hz or 1100 data points every second.

2. Sampling rates just below this threshold were found to not result in instantaneous termination of the data collection program however, would fail if the program was expected to collect data over an extended duration due to memory limitations since as initially the script is able to collect and interpret the load cell readings in time to report the desired rate but, as time progresses LabVIEW falls behind the readings given by the load cell, which is capable of

collecting measurements at a far higher rate than the LabVIEW program. As the program falls further behind the load cell the program was found to terminate data collection after a given amount of time depending on the sampling rate input. The closer the value was to the instantaneous failure threshold the shorter the program was able to collect data before terminating. The selection of the highest sampling rate used was therefore chosen by what high sampling rate would collect data over the complete duration of the shortest duration test configuration. All tests made use of a series of 12 rotations of the test body with each rotation maintaining a constant rotation rate. Over the course of all test configurations of the project a trade study of stepper rotation rate was conducted over a range of 1-10 RPM. This results in the shortest test case being 12 rotations at 10 RPM with a total test time of 72 seconds. A maximum sampling rate value for these tests would then only need to stably collect load measurements for the time needed to zero the load cell, bring the wind tunnel up to speed, and conduct the 72 second test. A window of 60 seconds was used to allow for zeroing of the load cell and bringing the wind tunnel up to speed as this allowed that value to be kept constant over all test cases and provided enough time for the maximum fan speed of 900 RPM to be reached consistently before the stepper motor began rotation. 1000 Hz proved a capable sampling rate to collect measurement of this 132 second requirement. At 1000 Hz for a stepper motor rotation rate of 10 RPM a total of 6000 data points were collected per each rotation. This value of 6000 data points would therefore need to be held constant between the various stepper motor rotation rates to keep the number of data points per azimuthal bin the same for all test configurations. This allows for the simple scheme to determine the proper sampling rate given rotation rate of the stepper motor.

$$f_s = (St_{RPM}/60) * 6000 \tag{4.6}$$

where f_s = Sampling Frequency (Hz),

St_{RPM} = Stepper motor rotation rate (RPM)

Using this scheme to consider the most tested configuration, that of 1 RPM stepper motor, a sampling rate of 100 Hz is identified. Through the micro-stepping provided via the stepper driver at maximum the 25,000 step count per revolution corresponds to a total of 69.4 steps required to traverse 1° and 1 second required to traverse 6°. A final rounded value of 17 data points are then determined to be contained within a 1° bin for data reduction. This value of 17 is standard among all tested cases utilizing CR in this project.

4.1.5 Test Rig Interfaces

A key change that has been implemented into the CR test rig compared to the work previously accomplished by the team of researchers at Georgia Tech concerns the manner in which the test rig is faceted and orientated relative to the wind tunnel. As mentioned within the earlier passages of this report, Georgia Tech's John Harper Wind Tunnel Memorial is characterized as having a substantially larger test section cross-sectional area than compared with Cal Poly's LSWT. The $2.13m \times 2.74m$ test section provided sufficient test space for a CR setup consisting of load cell, stepper motor, mounting rod, and test object to be vertically assembled and secured to the test section floor using a bolted tripod stand. Exploring the allowable clearance given by the test section size of the LSWT quickly shows the inability for this same configuration setup to be used as Georgia Tech.

A consideration that must be made in the development of any wind tunnel testing of an object mounted using a support arm is the impact of support arm interference. As a force acts upon any given arbitrary test object a bending moment is to be experienced from the support rod. The relationship between the given support rod material, experienced force, length of the support rod, and girth of the support rod will impact the amount of deflection the rod, and thus test object, will experience. It was previously discussed that for arbitrary bluff bodies the characteristic of substantial changes of any or all six components of loading can occur with only minor change to attitude. Rod deflection mitigation, or quantification, is therefore a primary goal to ensure load maps of test objects are accurately representing the correct orientation they are said to be reporting. An initial conclusion that could be taken from these comments is to make the support rod as rigid as possible to allow for virtually no deflection when in the presence of the forces expected at maximum load conditions for the AR1 cylinder and sphere. A short fat rod would then seems like the obvious solution to the problem then. This would be problematic for two reasons.

The first concerns the girth of the rod and its impact on the flow field within the wind tunnel. In an ideal world, the loading that acts upon the test object transfers through the support rod, into the stepper motor, and finally reaches the load cell where the loads are recorded and measured. This case behaves as if no physical mounting was needed to hold the test object completely within the freestream. There has been work done towards supporting methods that achieve this free body mounting, even allowing for test body attitude change using magnetic fields to suspend the test object [33]. This method would not be possible using the current capabilities of Cal Poly nor would it allow for a feasible way for loads to be captured using a load cell. In this ideal case no forces are lost as this transferring through the rig components occurs and the only forces being measured are those acting on the test object. In reality, all components that are placed within the freestream of the test section will

experience individual loading that will all be in turn recorded by the load cell as a single six component measurement. Since this support rod will always be placed perpendicular to the freestream, the cross-sectional area of the support rod is a simple way to interpret the amount of drag, the largest expected load component, of different support rod dimensions. An avoidance of larger cross-sectional areas will then result in the rejection of support arms of overly large girth or excessively long lengths as these promote larger cross-sections that will experience a larger drag force skewing the load cell measurement of the test object. At first this may seem like an issue that can be dismissed as a tare reading can be taken of the support rod with no test object present to be subtracted from all subsequent tests. It is indeed true that this can correct for the concern of added load measurement picked up from forces acting on the support rod but, it will not address the greater problem a larger girth support rod poses. As the mounting rod increases in girth a greater impact on the flowfield will occur on the side of the test object the mounting rod attaches to the test object. This interruption of the natural flowfield of the test object at that region can result in shedding of the boundary layer of the test object and the introduction of shed vertices that would otherwise not have occurred without the presence of the support rod. This support rod interference will thus cause pressure differentials along the geometry of the test objects impacting the final readings as taken from the load cell [47, 67]. It is thus the desired characteristic that the support arm creates the least disturbance possible to the test body flowfield. This explains way many support rods are chosen to possess streamlined contours for static support rods and circular cylinder support rods for moving support rods that would maintain a constant flowfield when rotated along its longest axis. The second major concern of support rod sizing considers what the ramifications are for the selection of a shorter support rod. A key goal of any support rod used for wind tunnel testing of an object is to hold the given body with the desired location of the test section. In the case of the testing of this project that

concerns the collection of load maps for arbitrary bodies within a freestream flow it was necessary for the support arm to provide enough clearance for the test object to be housed entirely within the freestream inside the test section to avoid wall interference effects to measurement as interaction with the boundary layer can manipulate the flowfield about a test body [60, 30, 54]. This meant that no portion of the test object was to be placed within or bordering the boundary layer that forms along the walls of the test section. Ideally this would see the object placed in a manner that saw its center point placed as closely to the center of the test section as possible. A rule of thumb for the LSWT wind tunnel is that the boundary layer extends 6 inches above the test section floor at the current mounting location. If the same exact strategy as the work previously done at Georgia Tech was utilized the support rod would need to be of short enough length to allow the clearance of the load cell, stepper motor, and interface plates within the test section while still placing the entirety of the test object within the freestream. At this reduced support rod length the test object is then placed significantly closer to the stepper motor and load cell housing which poses a risk to the flowfield of the test object at that side. This would prove to have an even larger concern than that of a larger girth support rod as the bluff body shape of the stepper motor would experience larger flow separation from its rectangular geometry causing increased error to load measurements.

If the complete test rig was to be left within the test section as done in the fashion of Georgia Tech a reduction to the size of the test object would be needed in order to achieve a sufficient support rod length to both place the test object within the freestream while also placing it far away enough from the test rig components to avoid interference of the flowfield. This shrinkage of the test object would be an undesirable solution to this problem given that the Mini58 load cell that is currently utilized for the test rig for this stage of the CR implementation operates within a sensing range higher than any expected forces on the two test objects even at the largest Reynolds

number conditions at the maximum tested wind tunnel speed. Any reduction to the size of either test object would further reduce these expected forces smaller than the sensing range of the load cell available for this project. A solution that both allowed for sufficient support rod length to minimize flowfield disturbances, place the object completely within the test section freestream, and avoid a compromise to test object sizing was required to successfully implement CR technique within Cal Poly facilities. The answer to this problem came from abandoning the initial configuration of Georgia Tech's implementation for one that better made use of the advantages that the LSWT has to offer to the John Harper Wind Tunnel Memorial.

As shown in LSWT schematic in Figure 2.2. A set of three Plexiglas walls line the side walls, ceiling of the test section with a series of plywood panels make up the floor. The glass walls do contain a few access points placed with the intent of providing access for instrumentation or wiring to components housed within the wind tunnel. This would not provide a sufficient region for mounting the test rig as it would experience the same spacing limitations as the previously discussed vertical orientation with the added challenge of securing the load cell to the glass wall of the test section. The ultimate solution regarding the orientation of the test rig was found to be achieved by inverting the original test setup with the load cell interface secured to the support frame along the top, outside of the wind tunnel. An access port cut into one of the wooden panels making up the ceiling of the test section allowed the support rod to enter the test section and hold a given test object while the majority of the testing rig, consisting chiefly of the load cell and stepper motor, are able to remain outside of the test section. The access port is sized beyond the diameter of the support rod to ensure that no contact is made between the mounting rod and the walls of the test section. This assurance of no contact with the walls of the test section is essential to confirm that the loads experienced on the test object are properly transferring through the test rig all the way to the load cell with no loss or distribution of the

forces that would transfer to the test section walls if the support rod contacted it during the duration of a test. The test rig is secured to the wind tunnel using an H-beam support system secured to the structural beam that runs along the streamline span of the test section shown in Figure 4.10. This support system, fabricated by an undergraduate AERO 200 student, is constructed from a set of the same structural beam as the wind tunnel to allow for easy faceting to the current beam infrastructure.

The grooves that can be seen along the aluminum extrusion beams that make up the H-beam structure as well as the structural beams of the wind tunnel allow for attachment via a bolt and sliding lock plate. When tightened these sliding lock plates creates the anchoring points to fully restrict the movement of the H-beam system along the span of the sliding groove. A benefit of this system is the added adaptability for the testing of different test objects. As previously mentioned, the purpose of this testing requires test objects to be placed fully within the freestream flow with no portion of the test object located near the boundary layer. Objects of differing size and shape may require differing vertical position to ensure complete orientation within the freestream. The sliding lock plate bolt interface for both vertical and horizontal position of the two beams making up the bars of the H-beam system as well as the additional crossbeam used for attachment of the load cell interface gives the ability to move the testing rig to always be in the ideal location. Vertical adjustments allow for the test rig to move the center location of the test object either up or down without the need for manufacturing multiple support rods of varying length. This allows a single support rod to be feasible to test for a variety of arbitrary test bodies with the center location of the objects remaining constant. The horizontal freedom to adjust can also be utilized to preform testing at differing stream-wise positions along the test section in future applications of the CR infrastructure, to further avoid test section wall interference.
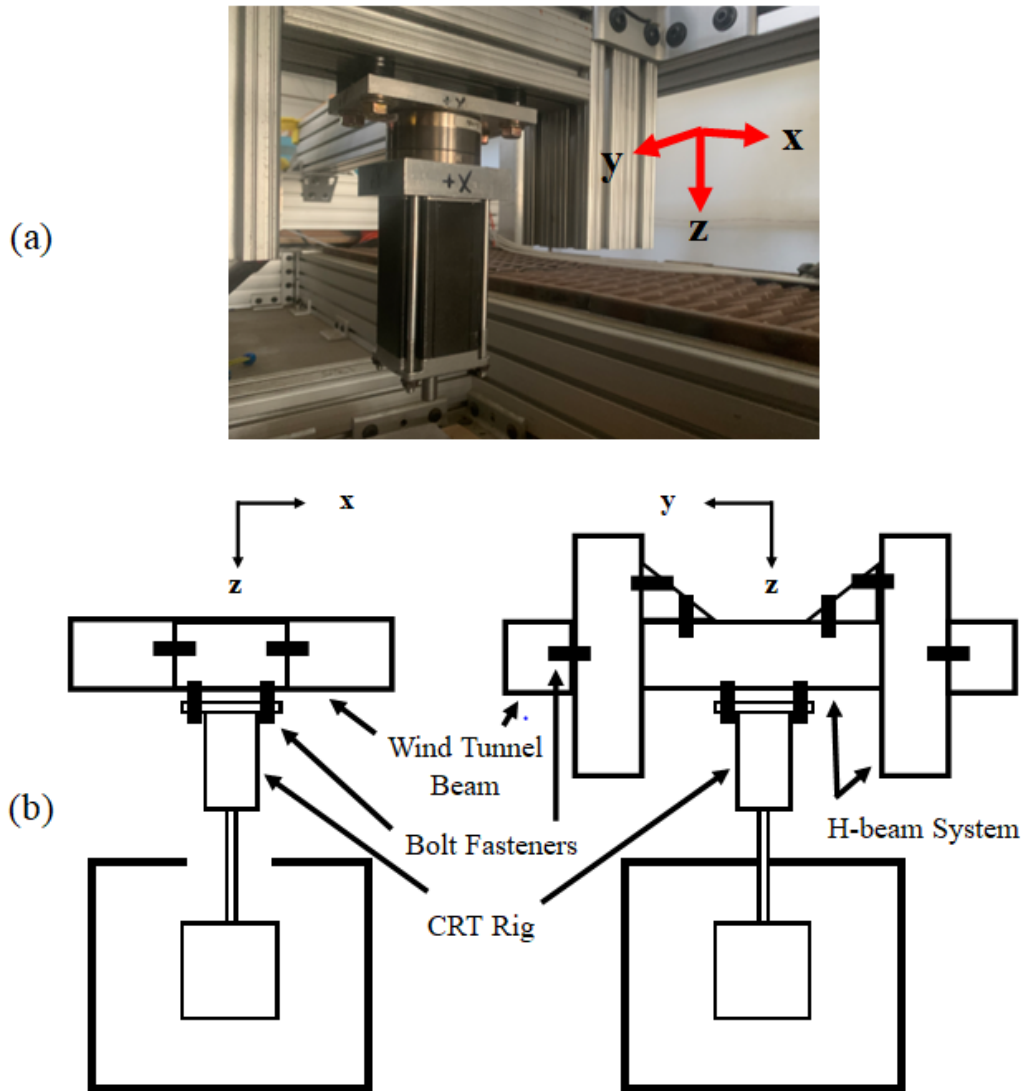
Figure 4.10: a) H-beam mounting system with component interface plates, mounted on aluminum extrusion beams b) Shows the side (left) and front (right) schematics of the H-beam mounting system with connection locations between aluminum extrusion beams and CRT testing rig allowing for adjustable location of CRT rig along crossbeam, height of crossbeam, and crossbeam location along x-axis

The inverted vertical orientation of the test rig provides a combating to deflection of the support rod resulting from the drag forces. Since the test object is being suspended into the test section as illustrated by the diagram of Figure 4.11, the weight from the test object before forces are even supplied from the wind tunnel is pulling the

object down. This downward force is then acting as corrective force to any deflection that may occur when the wind tunnel is in operation and drag forces are bending the support rod. This is a useful tool when testing objects that experience substantial changes to all loading components with minor pitch attitude alteration. This may not be a substantial enough corrective force to completely remove any deflection that occurs depending on the test object but, will contribute to deflection reduction. This is untrue of horizontal configurations of the test rig where the weight of the test object creates a force and source of deflection to the rod before the wind tunnel has even been turned on. It is worth mentioning that given the current Mini58 load cell utilizes sensing ranges and overload limits far beyond the values capable of being produced on the two current test objects further study into a method of adding additional weight to the current objects in a manner that would not result in a significant unequal weight distribution could further aid in support rod deflection.
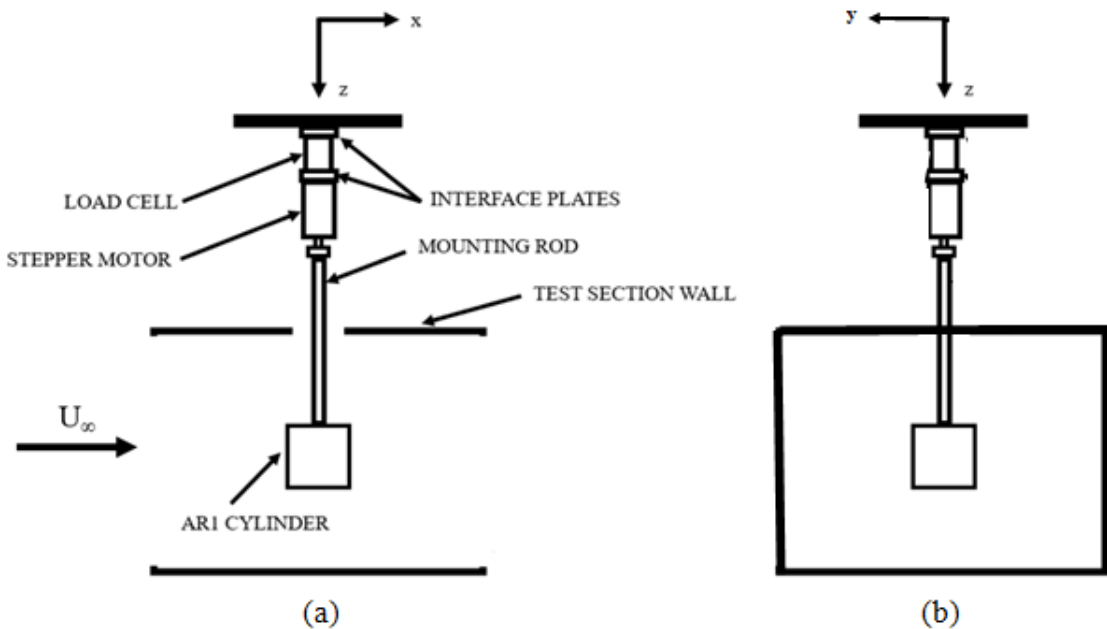
Figure 4.11: a) Side view schematic of Cal Poly CRT infrastructure consisting of load cell and stepper motor casing housed and supported between a set of interface plates with mounting rod secured to stepper motor shaft for suspension of test body within wind tunnel test section b) Front view schematic of same setup

4.2   Topic of Encoder Improvements

A goal of improvement for the implementation of this CR testing rig than compared to the original rig located at Georgia Tech was a refinement of the encoder system for better usage of identifying slippage. The term slippage in this context refers to the phenomena of the model slipping forwards or backwards along the duration of a given rotation. A consequence of this slippage if left unnoticed will be an offsetting of subsequent measurements taken in the following rotations. When this occurs the actual attitude of the test object will not match with the location the assumed by the stepper motor as it continues with its set number of actuations. This results in data shifting away from its proper location. When this is combined with the time-averaging element of the CR technique a smoothing to the behavior of the final load maps can be observed, especially in regions of nonlinear behavior. This smoothing then results in failure to capture this behavior that would otherwise be captured by standard static measurement. An encoder system ensures that the progression of steps has fully completed by the end of a test. In previous work accomplished at Georgia Tech this was done by use of an optical encoder that reported when a complete rotation had been recorded. This when paired with the known rotation time of the stepper motor was used to assess if slippage had occurred and by what extent.

The work done at Cal Poly has refined the resolution from the original concept to allow for the constant feed of encoder data to incrementally track rotation progress. This provides the same means for ensuring the test has successfully completed the required number of stepper motor steps in the time as given by the rotation rate. This is done by taking the step count number of the encoder wheel and multiplying by the 12 rotations of a given test. Where this provides a level of further insight then the Georgia Tech comes from the ability to plot the continuous data provided by the

encoder system over the time taken for the 12 rotations. This vector of time will have a incremental step size that matches the delay value specified by the Arduino script that controls how often a measurement is taken by the optical sensor. If the laser of the sensor is obscured it will indicate a value of 0 and a value of 1 when not obscured. Since all slots of the encoder wheel are sized the same and the rotation of the stepper motor is constant the pattern of binary values given by the optical encoder should be a steady and repeating pattern. A disruption of this pattern by a lengthening or shortening of the duration the encoder stays at a given value would therefore indicate that slippage had occurred. This allows specific points of interest to be identified.

Incorporation of an encoder system makes use of two 3D printed components that are shown with interfaces to the stepper motor in Figure 4.12. An interface plate was designed and fabricated to firmly hold on to the face of the stepper motor via a 4-point-of-contact press-fit. A notch extends out from this connection which is used to secured the optical sensor of the encoder system to a fixed position. It is important to ensure that the sensor is not allowed to freely move during the course of a rotation as movement could create a false positive result that slippage has occurred. A encoder wheel with base thickness of a standard CD was designed and 3D printed. This wheel provides equally spaced slots to provide 360 increments per revolution. The dimensions of the holes of the encoder match the size of the adjacent printed material. The outer radius of the encoder wheel making up the encoder slots is increased in thickness to avoid being too thin to successfully block the laser of the optical encoder as was found to be the case for previous designs of the wheel.
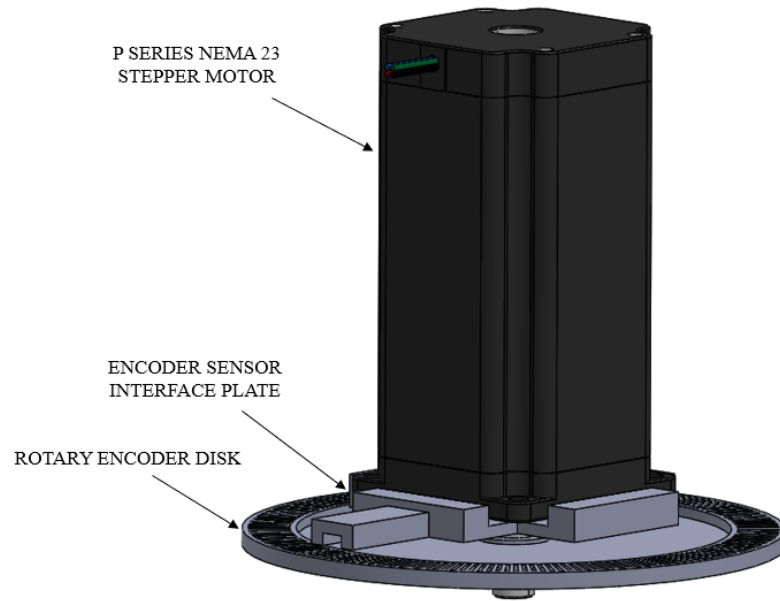
Figure 4.12: 3D model assembly of the 3D-printed optical encoder setup with Nema 23 stepper motor using a press-fit adapter plate with an access port for stepper shaft and slot for optical sensing device [5]

Figure 4.13 captures progression of incremental encoder as a pulse graph with corresponding drag measurements simultaneously captured. The duration the encoder state remains at the value of 1 longer than the value switches to the state of 0. The explanation of this would come from the wheel design. As mentioned, the dimensions of the positive and negative regions along the laser sensor's path were the same. For the sensor to report a value of 0, the sensor needs to be fully obscured which only occurs for a split second when the encoder is perfectly positioned. As soon as this moment has passed the encoder sensor value will jump back to 1 as it now is only partially obscured. The pulse graph indicates in 1 second of encoder data, during which 6 degrees of rotation occurred matching expectations of this test $(360/60 = 6(deg/s))$.
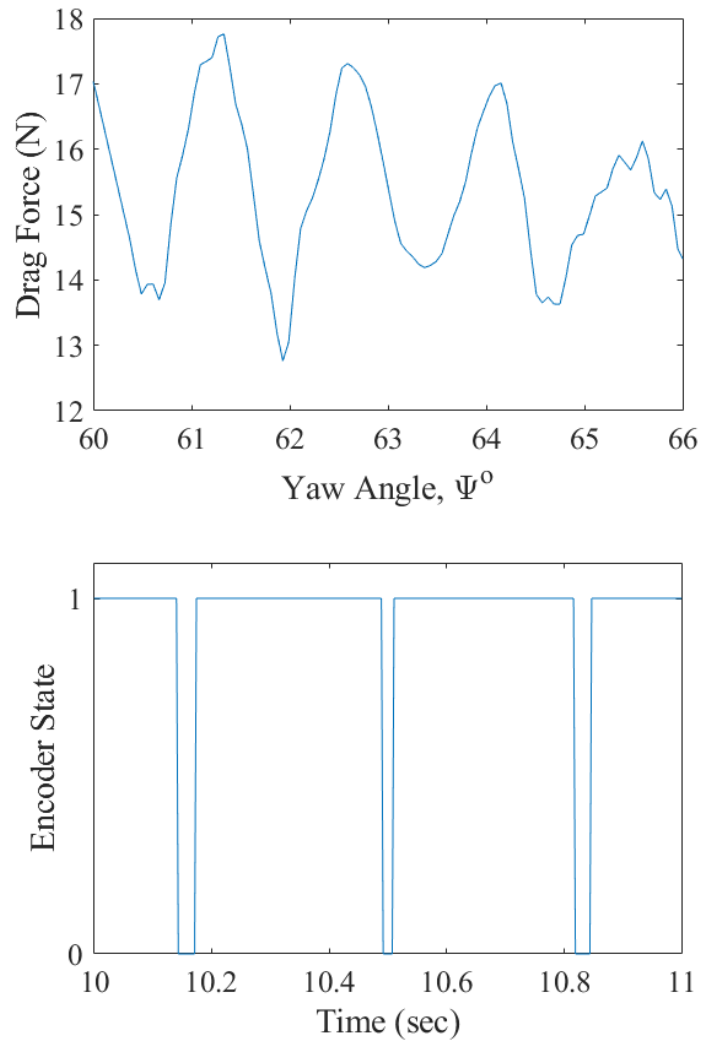
Figure 4.13: Encoder State, AR1 Cylinder, Stepper 1RPM, $Re = 235301$

4.3 Validation Testing

4.3.1 Test Matrix

To test this setup over a complete span of the wind tunnel's capabilities the following test matrix was developed to identify the number of unique testing conditions within the wind tunnel that would be tested located in Table 4.3. Test conditions are characterized by the speed at which the wind tunnel is set as well as the rotation

rate set for the stepper motor. Each test condition was performed twice, once with the Aspect Ratio-1 cylinder and once with the sphere test bodies. The final column tabulates the duration of test time required to finish a test of that particular test conditions. The duration includes the 1 minute buffer time before the stepper motor begins to rotate. This buffer zone is used to zero the load cell and bring the wind tunnel to steady state at the desired speed.

Two static conditions are included within the test matrix to have a means of validating that the measurements collected by the load cell during CR tests are accurately capturing the static behavior that would be expected given the quasi-static assumption. The collection of these static measurements was achieved by mounting the test objects to the same CR test rig but, making use of a different Arduino script specifying the movement of the stepper motor. This code held the stepper motor in a static position for a total of 30 seconds before rotating the body 1 degree. This process is repeated for a full 360-degree revolution of the test object with each 30 second bin averaged to provide 360 averaged static measurements for both objects. A test time of 3 hours for each of these AR1 static tests further highlights the need for a testing rig like the CR rig discussed in this project. Sphere static testing used a single 30 second average measurement.

Table 4.3: Continuous Rotation Technique Test Matrix

Test Cond.	Fan (RPM)	Stepper (RPM)	Body	Time (min)
1	400	Static	AR1, S	181
2	900	Static	AR1, S	181
3	400	1	AR1, S	13
4	400	2	AR1, S	7
5	400	3	AR1, S	5
6	400	4	AR1, S	4
7	400	5	AR1, S	4
8	400	6	AR1, S	3
9	400	7	AR1, S	3
10	400	8	AR1, S	3
11	400	9	AR1, S	3
12	400	10	AR1, S	3
13	900	1	AR1, S	13
14	900	2	AR1, S	7
15	900	3	AR1, S	5
16	900	4	AR1, S	4
17	900	5	AR1, S	4
18	900	6	AR1, S	3
19	900	7	AR1, S	3
20	900	8	AR1, S	3
21	900	9	AR1, S	3
22	900	10	AR1, S	3
23	500	1	AR1, S	13
24	600	1	AR1, S	13
25	700	1	AR1, S	13
26	800	1	AR1, S	13

4.3.2   Testing Procedures

The following list enumerates the steps taken for the collection of load cell data for any given test run. The steps are given in the order in which they would occur. Post-processing of the data collected using these steps is detailed in the included Matlab scripts within the Appendix A.2.

1. Securely attach test object to mounting rod via a locking nut to threaded extent at end of rod.

2. Insert stepper motor interface of mounting rod through ceiling of wind tunnel test section. Ensure personnel is located atop wind tunnel to support rod prior to attachment. Mounting rod is secured to stepper motor shaft via a size 4 metric Allen wrench locking pins.

3. Orient the test object in the desired starting position for rotation, the test object should freely spin at this phase.

4. Power up the stepper driver system and ensure the test object has not altered in position, the test object should now be rigidly held in place.

5. Power up load cell power supply, this step is ideally done an hour before testing if possible to provide ample time for the load cell to warm up.

6. Launch LabVIEW 6-DOF ATI load cell interface program. Set sampling rate to the desired frequency to ensure constant data points per 1 degree of stepper rotation is maintained. Set file name of given test run.

Figure 4.14: LabVIEW terminal interface with controls of zeroing load cell, setting sampling rate, and saving data points to mat file

7. Open two Arduino codes, stepper motor control and optical encoder system control, on two separate terminals as both codes will be running simultaneously using two Arduino Uno. In addition have opened on the optical encoder terminal CoolTerm.exe to transfer data from the serial monitor to a .txt file for post-processing.

8. Set the fan speed to the desired RPM rate. Ensure that wind tunnel facilities are ready for test by the standards of Cal Poly's Low Wind Speed Wind Tunnel safety procedures.

9. Simultaneously begin the two Arduino programs, a timer of 60 seconds will elapse before the stepper motor begins to rotate and the optical sensor begins reporting state.

10. Happening simultaneously with step 10, have an additional support personnel begin the LabVIEW program. When the program begins select the zero button on the interface to ensure the load cell has been properly zeroed.

11. After the load cell has been zeroed bring the wind tunnel up to desired speed. Verbally confirm that the tunnel has reached speed prior to rotation of the stepper motor.

12. Upon completion of rotations, end labVIEW load cell data collection and encoder state collection.

13. Shutdown wind tunnel in accordance to Cal Poly's Low Wind Speed Wind Tunnel safety procedures and operating procedures.

Chapter 5

ERROR AND UNCERTAINTY ESTIMATIONS

The classification and evaluation of sources of error and uncertainty present for the testing system as constructed at Cal Poly are considered. This can be broken down into two categories with the first being sources of error that became known or were identified during the process of data collection or post-processing. These factors are discussed in focus in section 5.1 chiefly being the discussions of stepper motor wobble and stepper motor noise generation. The latter of this chapter will then seek to provide values to the uncertainty present in the system in both systemic and statistical components. This is concluded with the final tabulation and report of total uncertainty in each axis of interest as dimensional values. The extent of uncertainty identified in this chapter will provide further insight during the subsequent results chapter to highlight the significance of that uncertainty in the face of the forces collected from the two test objects.

5.1   Testing Rig Complications

Testing rig complications refers to the unforeseen phenomena that was not initially expected at the onset of this thesis work in its literature review phase. Analysis is conducted to either correct or quantify the extent of said phenomena for future work as a insightful tool for its eventual mitigation or removal. A wobbling behavior of the mounting rod while in motion is viewed as a potential source of error in objects where pitch orientation will significantly impact airload measurements. A technique for measuring the displacement of wobble is highlighted and subsequent results for

both test objects are included. In addition, an unanticipated noise within the raw data is observed. This source of this noise, the stepper motor, is discussed and the creation and implementation of a sufficient filter to remove the noise is mentioned.

5.1.1 Mounting Rod Wobble

Both visual observations made during testing and corresponding video footage captured of said test runs appeared to show a wobbling motion of the mounting rod outlining a circular pattern that roughly matched the diameter of a US quarter at the tip of the mounting rod. The direct source of this drift was not initially identified as the presence of shed vortices from the geometry of the two tested bodies, AR1 circular cylinder and sphere, could be inducing a shaking of the test bodies matching the shedding frequency for the object. This would later be supported by the presence of some shaking of the test object during the static testing on the same test bodies. When a test was run with the wind tunnel not in operation the noticeable drift of the shaft from its vertical orientation was still present and characterized to follow a sinusoidal motion over the course of a single rotation before returning to its starting position upon finishing the revolution. Since this behavior is present even without the presence of a wind tunnel freestream and the orientation of the test rig has the weight of the test object pulling down, thus not adding a buckling or bending moment to the mounting rod, it is likely that a manufacturing error has produced a misalignment of the stepper motor shaft. This misalignment may not be a concern when the stepper motor only has its shaft extend 10mm from its casing but, the added length of the support rod amplifies this misalignment to noticeable levels.

To better understand the extent of this wobbling it became an important task of the project to provide a quantified report of the distance that the wobble is displacing the test objects. Since bluff bodies can come in an arbitrary number of shapes and sizes that can experience significant changes to all six components of aerodynamic loading with smaller attitude change, knowing how much displacement the bodies experience will serve future work for assessment if additional design work must be made into the current test rig to reduce or eliminate this wobble if deemed too extreme. To acquire this quantitative data the videos taken of various test runs was used to determine the displacement of the bottom of each test object at various points over the duration of a single rotation. Still images from the videos were collected at 5 second intervals for test cases utilizing a 1 RPM stepper motor speed. The stills were captured via a smartphone camera secured in a stationary position to ensure that all captured images from any given test run would have the exact same captured field of view. This was important because any shift or off-centering of the camera during the duration of a video would be reflected in the assessed displacement of the test body from its initial position.

The still image at time zero, or the moment of the video where the test object was just beginning its rotation, was used for the defining of the coordinate system that would quantify drift. The overlay of this coordinate system was accomplished using an engauge digitize software. This software allows for a coordinate system to be placed atop an image and subsequently specify to the user the x-y coordinates of any point within the image. The intersect of the x and y axis was defined as the top of the test object at the center of the support rod. The reason this point was chosen as the intersect was due to it being the must consistently simple location to manually select from the image. This is easily explained by the locking nut interface between the threaded end of the mounting rod and the measured center hole of the test objects, specifically the AR1 circular cylinder. This interface ensure no sliding or slippage

of between the rod and test object making it an easily visible fixed location relative to the two components. The process of setting up the coordinate system in engage digitize allow requires two additional points within the image to be defined to be able to determine any point within the rest of the image. The use of the test body and support rod characteristics allows for this to be a simple task.

It was stated that the $(0,0)$ point was selected as the center of the support rod at the point the rod is flush with the test object. Knowing the radius of the support rod easily allows for the determination of the $(X,0)$ coordinate by setting X equal to the radius and placing the point on the wall of the support rod directly adjacent to the initial point on the downstream side. Now that the x-axis has been defined for the software, a final point can be placed at the $(0,Z)$ position directly below the first point located at the bottom of the test object. The value of Z will correspond to the diameter of the sphere or the circle making up the AR1 circular cylinder depending on which test object video is being examined. The coordinate system now being fully defined allows for the software to quantify drift of subsequent images. When the next still is imported into the software it is able to replace the current image overlaid onto the coordinate system. When the new still replaces the previous the identical framing of each image results in any change of the position of the test body and support rod to be found by selecting new location of the bottom of the test object. The difference of the (X,Z) points between the nth still and the 0th can be used to produce the displacement of the body along the x and z axis. A disadvantage of this method of testing for displacement is that for videos conducted with the wind tunnel in operation there is no means for framing the test body and support rod within the y-z axis resulting in no quantifying the values for the displacement of the body along the y-axis during a single rotation. Provided below in Figure 5.1 is an example of one of these coordinate systems overlaid onto a still image of a sphere test object.
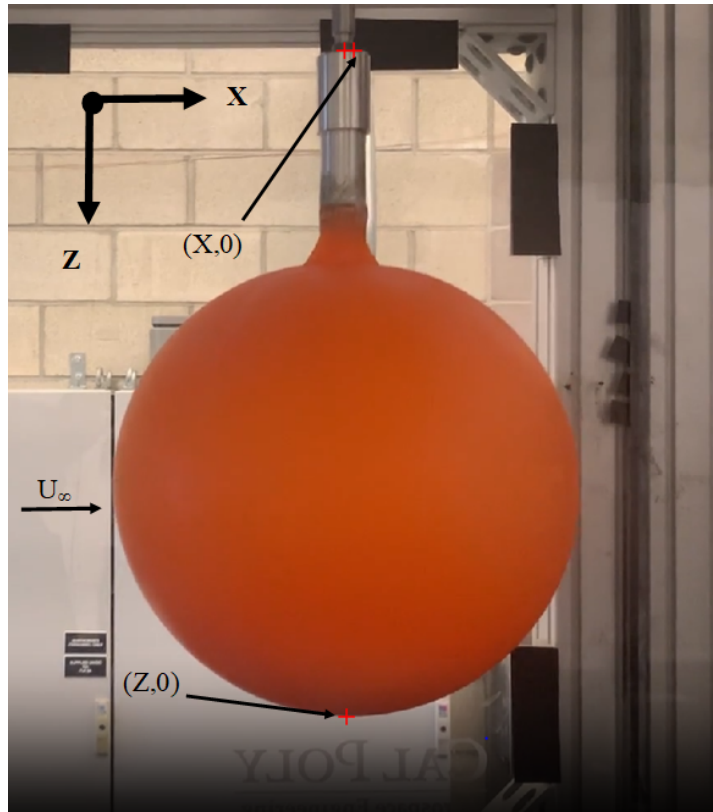
Figure 5.1: Sphere test object mounted with the Cal Poly Low Speed Wind Tunnel with labeled locations of (X,0) and (Z,0) being the bottom of the sphere test object and outer diameter of the mounting rod

Table 5.1 catalogs the x-axis displacement that is experienced by the AR1 circular cylinder at each time step for a series of different 1 RPM stepper motor tests at varying wind tunnel fan speeds.The same process is cataloged for the sphere test body. The 8-inch sphere was used to conduct the same tests as performed by the AR1 circular cylinder with the goal of better removing the effects of changing the flowfield at different stages of the rotation due to attitude change relative to the freestream. The symmetrical nature of the sphere allows it to maintain the same profile relative to the freestream regardless of what orientation it is in therefore, if the quasi-steady assumption is valid the flowfield would not change from the rotation by the stepper motor. Sphere testing used a support arm of smaller girth than the AR1 which resulted in further deflection from the forces acting on the body.

Table 5.1: Mounting Rod Drift Quantification

Time (sec)	AR1 (deg)	AR1 Dist (in)	Sphere (deg)	Sphere Dist (in)
0	0°	0	0°	0
5	0.55°	0.08	0.57°	0.08
10	1.64°	0.247	2.21°	0.309
15	1.62°	0.244	3.38°	0.472
20	0.54°	0.08	2.25°	0.314
25	0.52°	0.08	1.58°	0.221
30	0.26°	0.04	0.54°	0.08
35	−0.66°	−0.10	−0.25°	−0.03
40	−1.10°	−0.166	−1.16°	−0.162
45	−0.57°	−0.09	−1.85°	−0.258
50	−0.57°	−0.09	−3.37°	−0.470
55	−0.17°	−0.03	−1.18°	−0.165
60	0°	0	0°	0

5.1.2 Stepper Motor Noise

A issue that developed during the post-processing phase emerged regarding the reduction of noise the stepper motor was having in the final data as collected by the load cell. The initial LabVIEW interface made use of two parameters, sampling rate and samples per read, to determine the total number of data points collected and given in the final text (.txt) file for post-processing. Sampling rate would correlate to the number of samples taken from the load cell in a given second of recording. The samples per read define how many of samples would be taken in a batch and averaged to provide a reading. For example, if the sampling rate was set to 1000 Hz with a samples per read of 10 this would result in 100 data points per second for post-processing. A later iteration of this LabVIEW program removed the samples per read as a parameter and thus all samples taken from the load cell would be reported. This produced a more raw set of data that displayed noise that wasn't observed prior due to the previous format incorporating an averaging of raw data values. To identify the source of the noise the configuration of the test rig was considered. Since loads

imparted on the test object are only allowed to transfer through the mounting rod and stepper motor housing on the way to the load cell it was clear that the operational noise of the stepper motor must be the source of this noise seen in the data. Looking at Figure 5.2 the noise can most easily be seen by the overlaid drag measurements of a particular AR1 cylinder test. Here the behavior is shown as streaking spikes of the data equally spaced along the duration of each rotation. The frequency of noise corresponds to the pulse per seconds created by the stepper motor, at a given microstepping setup. This is a known value and this frequency component can be filtered.
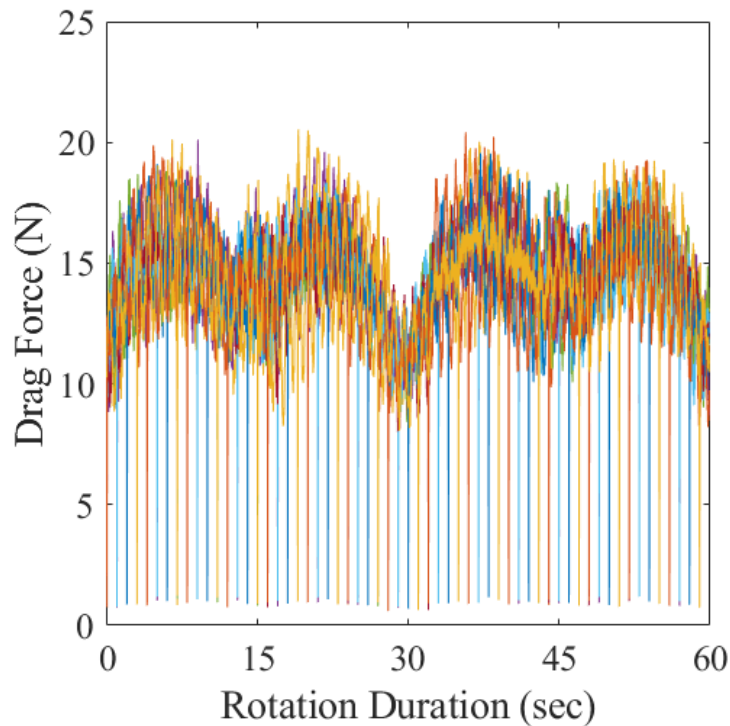
Figure 5.2: Rotations Drag Noise, AR1, Stepper 4RPM, Fan 500RPM with each color representing rotations 2-11 used for post-processing

When left uncorrected, this same noise makes its way into post-processing as a time-averaged dataset. Figure 5.3 shows this result as the spikes non align with the contour of a higher concentration of points that closely follows the expected behavior of the drag map for the AR1 cylinder at this wind tunnel test condition. A reduction to this

noise occurs as a natural consequence of the time averaging of individual rotations but is still noticeable and creates a poor load map. A similar process occurs when the data is further post-processed to its final iteration with the bin-assembled average, phased averaged to an angular resolution of 0.5-degrees, load map of Figure 5.4. The spiking behavior, while decreased in amplitude, has become systemic and created a jagged load map of drag. This becomes a large problem specifically when considering the regions of the load map where nonlinear behavior becomes dominant like 45-degrees.
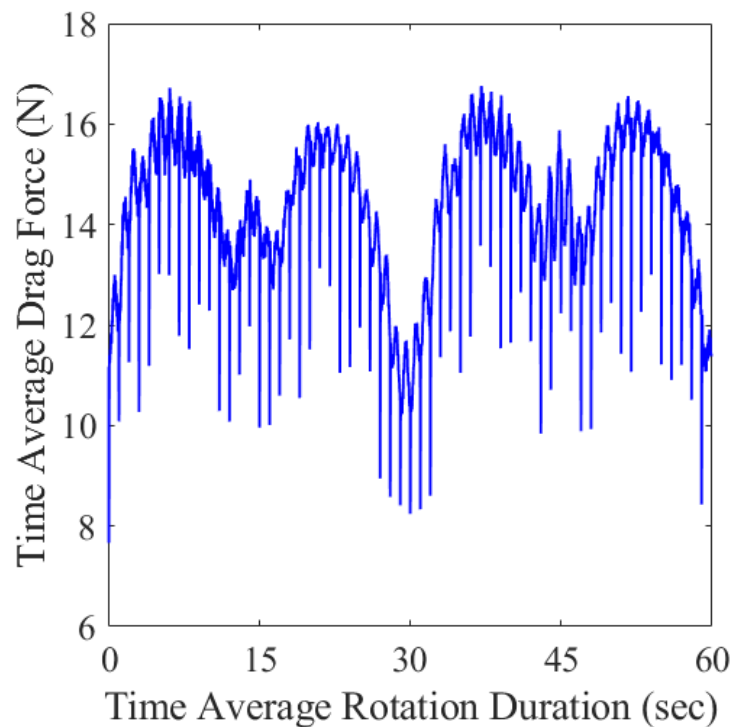
Figure 5.3: Time Averaged Drag Noise, AR1, Stepper 4RPM, Fan 500RPM

The process of correcting this unwanted noise first required the understanding of what frequencies of the data were desired and what frequencies were imparting these undesirable effects. Using the algorithm provided with Eq. 5.1-5.5, Figure 5.5 illustrates the single-sided amplitude spectrum for the drag data of the same AR1 test case as Figures 5.2-5.4 through use of a Fast-Fourier Transformation. Sampling frequency is set to the same value as set within the LabVIEW interface with sampling period and

Figure 5.4: Final Time Averaged and Phase Averaged with angular resolution of 0.5 degrees Drag Noise, AR1, Stepper 4RPM, Fan 500RPM
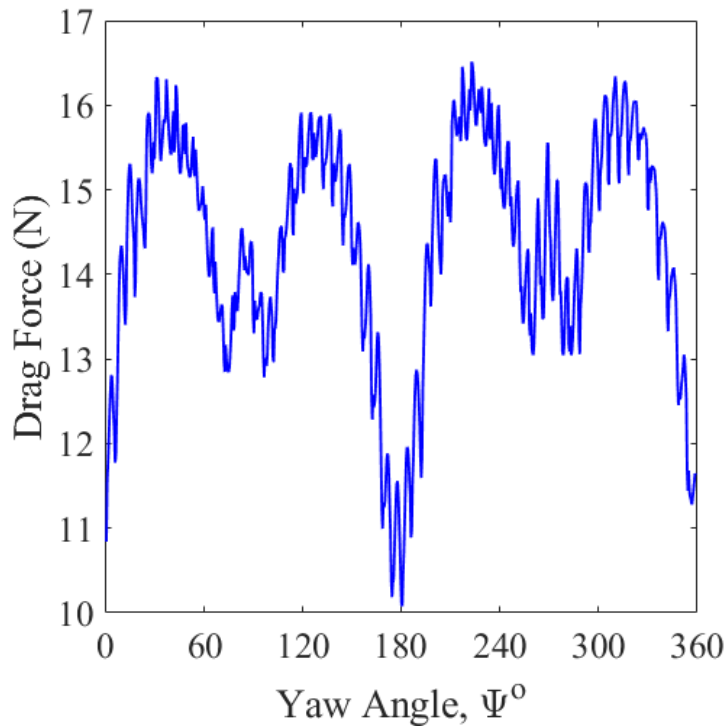
time vector derived from the sampling frequency. The length of the signal is set to match the length of the vector for the parameter seeking a noise reduction, in this case drag. The initial spike of magnitude between the frequency values of 1-3 Hz are identified to be the behavior of the object captured by the load cell. This was concluded as the reduction or removal of data at this frequency resulted in the final load map not matching any of the expected behavior of this object. This provided a frequency cutoff of 3 Hz and above where the magnitude of noise above this threshold was to be reduced. The Butterworth notch filter within the filter design function of Matlab was utilized to reduce the power of frequencies within a specified range by half. The range of 3 to 50 Hz was selected as it reduced noise experienced by the final load maps. Compare Figure 5.4 to Figure 5.6 serving as the before and after the implementation of the filter.

$$T = 1/F_s \tag{5.1}$$

$$t = (0 : L - 1) * T \tag{5.2}$$

$$f = F_s * (0 : (L/2))/L \tag{5.3}$$

$$P_1 = abs * fft(Data))/L \tag{5.4}$$

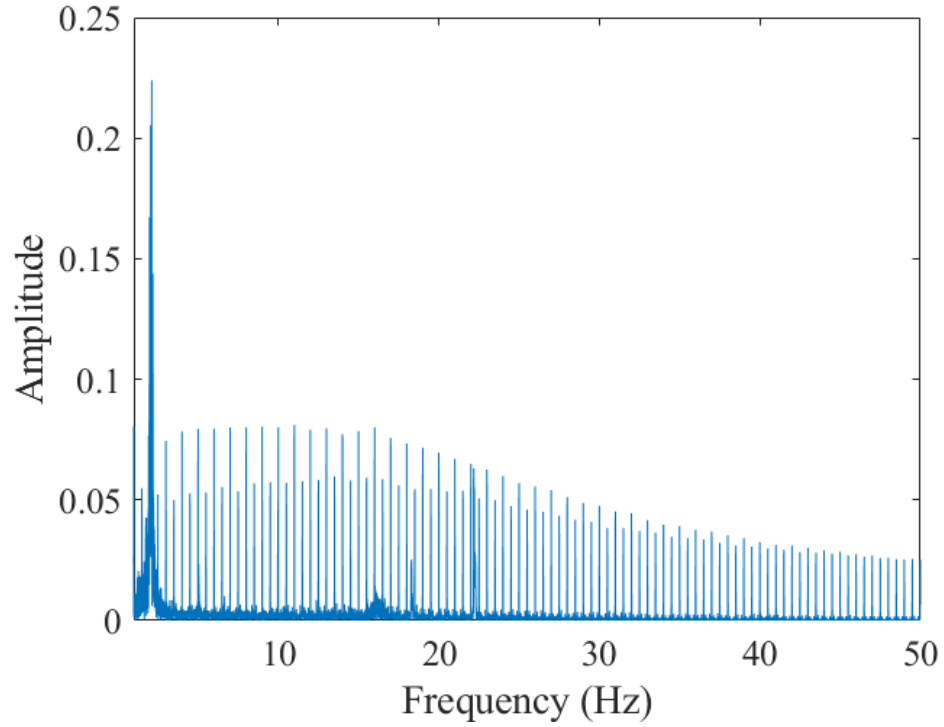$$P_2 = P_1(1 : L/2 + 1) \tag{5.5}$$

Figure 5.5: Single-sided Amplitude Spectrum obtained from FFT where concentrations at 3 Hz correspond to load cell data, at around 23 Hz corresponds to the observed shedding frequency of the circular cylinder, and at 15 Hz to stepper motor noise
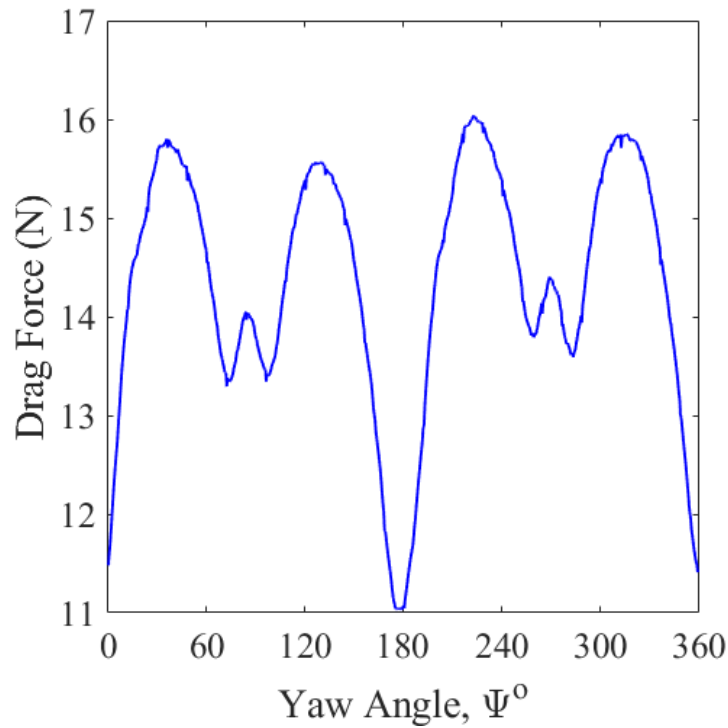
Figure 5.6: Drag Filtered, AR1, Stepper 4RPM, Fan 500RPM, obtained by applying Butterworth notch filter removing systemic noises coming from stepper motor in the frequency range 3-50 Hz

While this current implementation provides a means for removing this noise present within the raw data taken from the load cell it does not distinctly identify in what manner this noise is being generated from the stepper motor. An additional set of tests can help to provide validation that the stepper motor is indeed the source of the noise but, distinguish the nature of the noise. This distinguishing that is being referred to is the question of whether the noise from the stepper is from an electrical origin or if the noise is generated from the a mechanical source with the physical actuation of the stepper motor. Testing with the wind tunnel not in operation, thus no acting forces, can provide further insight with a set of data with no noise impacts from outside sources in turn isolating the noise from the stepper motor. Subsequently, testing of a object with an added weight can provide a means to verify inertia effects

leading to odd spikes of the data. A heavier test object could potentially become a means of controlling this effect and thus remove the requirement of a filter.

5.2 Uncertainty Assessment

The quantitative assessment of uncertainty present within the system is performed. This process is done by the individual total uncertainty being represented between a statistical and systemic component. The statistical uncertainty is assessed with the use of standard deviation values for a given test run of 10 rotations of data being processed to arrive at uncertainty windows for all three airloads of interest. This component of uncertainty is subject to change with considerations of increased sampling rate or number of rotations or tests. The systemic uncertainty is a far more stagnant value being derived from the limitations of the load cell utilized being the driving characteristic. Strategies of how best to improve the total uncertainty are mentioned.

5.2.1 Statistical Uncertainty

The statistical uncertainty is the component of total uncertainty that comes from the given observations obtained from any given test run. The determination of this uncertainty value is found during the data reduction phase of the CR technique, specifically prior to the assembled bin averaging that produces the final generated load maps. The first step of this process consists of evaluating for the standard deviation of each relevant rotation of the duration of a test. In the case of the tests conducted in this project a total of 12 rotations are made for any given test with the first and final rotations being left out of data processing to ensure the stepper motor is at constant speed with no acceleration or deceleration being captured by the load

cell measurements used to generate the load maps. Eq. 5.6 demonstrates the setup that is used within Matlab to determine these standard deviations.

$$S = Std(A) = \sqrt{\sum (x - \mu)^2 / (N - 1)} \tag{5.6}$$

$$S^T = \begin{pmatrix} Std_{t_1} \\ Std_{t_2} \\ Std_{t_3} \\ ... \\ Std_{t_{6000}} \end{pmatrix} \qquad A = \begin{bmatrix} Rot_{2t_1} & Rot_{2t_2} & Rot_{2t_3} & ... & Rot_{2t_{6000}} \\ Rot_{3t_1} & ... & & & ... \\ Rot_{4t_1} & & ... & & ... \\ ... & & & ... & ... \\ Rot_{11t_1} & ... & ... & ... & Rot_{11t_{6000}} \end{bmatrix}$$

Here A is a matrix made up of the observations of the 10 interior rotations that are considered for post-processing purposes. The matrix is built with the columns representing the 6000 data points that make up a given rotation. This can be thought of as the independent variables that the standard deviations are being found for. Each rotation considered serves as an observation of that given time step variable. The result of this setup is a row vector of standard deviations with each entry representing the standard deviation value for that data point on the interval $[1, 6000]$. This general scheme is able to be used to obtain row vectors for the drag, side force, and torque moment standard deviations. Once these standard deviation vectors are calculated they can be used to show statistical uncertainty from the phase average values for the mentioned parameters at each time step. When this is applied to a know rotation rate of the stepper motor the final results can be displayed as graphs of shaded regions of uncertainty mapped of yaw angle as shown in Figures 5.7-5.9 for testing conducted on the AR1 circular cylinder at $Re = 235301$. When the average of the standard deviation row vector is found this solves for the statistical uncertainty

value this is used during the tabulation of total uncertainty. The quoted average statistical uncertainty demonstrates a reasonable confidence of repeatability between the rotations and can be improved with an increase of either the number of interior rotations of a given test or increasing number of experiments.

Figure 5.7: Standard deviation drag force statistical uncertainty of aspect ratio 1 circular cylinder for the 400RPM fan, 1RPM stepper
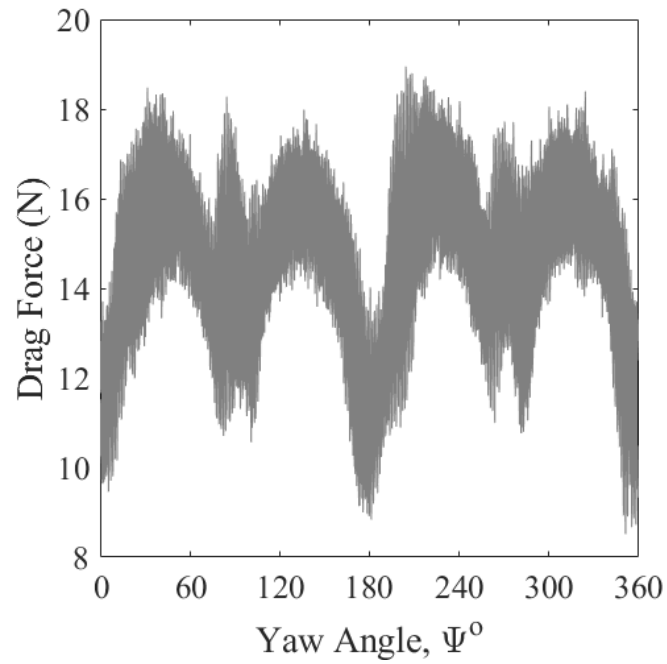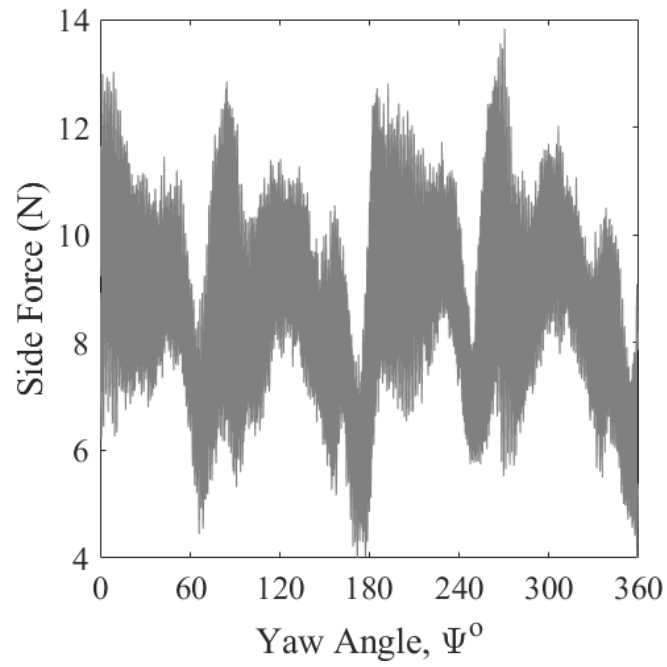
Figure 5.8: Standard deviation side force statistical uncertainty of aspect ratio 1 circular cylinder for the 400RPM fan, 1RPM stepper
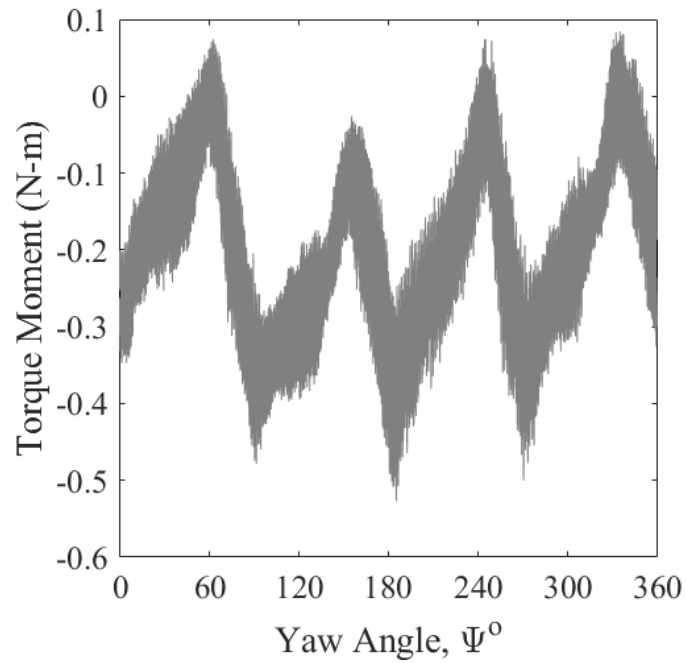

Figure 5.9: Standard deviation torque moment statistical uncertainty of aspect ratio 1 circular cylinder for the 400RPM fan, 1RPM stepper

5.2.2 Total Uncertainty

The final tabulation of total uncertainty of the CR test rig is made up of both the statistical uncertainty that is determined by the observations collected for a given test run or series of the same test, which was calculated in the previous section, and any uncertainty that exists within the physical system itself. The component that will determine the value of this system uncertainty is the ATI Mini58 load cell. The uncertainty that will be used in this report comes directly from the published calibration certificate that is provided by ATI to its customers upon delivery of any purchased models. The common sources of error that can impact the certainty of a load cell consists of steady state temperature assumption, errors associated from non-linearity, cross-talk, and hysteresis to list the more significant sources. The ATI published full-scale measurement uncertainty considered all lists error sources and represents them as a single percentage of the maximum sensing range of the load cell. Table 5.2 makes use of the full-scale measurement uncertainty with the previously cataloged sensing ranges to provide the system uncertainty that is caused via the load cell.

To translate the individual components of total uncertainty into a single total value that is provided for the three components measurements of interest the following Eq. 5.7 is used:

$$\sigma_{total} = \sqrt{\sigma_{loadcell}^2 + \sigma_{statistical}^2} \qquad (5.7)$$

The largest source of identified uncertainty as a component of the whole total uncertainty of the system is coming from the system uncertainty of the load cell. This was to be expected as the the sensing range the ATI Mini58 far exceeds the measured values of the tests conducted in this project. The full-scale measurement uncertainty window of $1.25 - 2.25\%$ at this higher sensing range leaves a larger window of un-

certainty that may be possible to achieve with a smaller range load cell. This would require a load cell that would be expected to have an inferior full-scale measurement uncertainty as the commercially available ATI Mini58 but if the sensing range was tailored more specifically to the window of forces and moments seen by the test objects could in the end result in a lower uncertainty component from the load cell [10, 19].

Table 5.2: Total system uncertainty tabulation for CRT test rig considering statistical uncertainty associated from data set size and systemic uncertainty of load cell measurement

Component	$\sigma_{loadcell}$	$\sigma_{statistical}$	σ_{total}
$F_x(N)$	8.750	1.368	8.856
$F_y(N)$	8.750	1.395	8.860
$T_z(N-m)$	0.674	0.061	0.678

The issue of this current tabulation of total uncertainty for the apparatus is how large this uncertainty is when compared to the forces and moments that can be achieved on the test objects within the operational limits. In its current form the total uncertainty window can reach as high as 10% of the captured loads from the load cell with the torque moment seeing the worst of this effect. This brings into question how well the testing rig, at this phase of the project, can actually capture the nonlinear behavior that is shown within the results of this thesis. Is this nonlinear behavior that is being captured truly there or is instead a product of this significant uncertainty will become a substantial area of focus for future work for the continued improvement of Cal Poly's implementation. This thesis work is to serve as an initial proof of concept for the incorporation of a continuous rotation technique within Cal Poly facilities using the resources already available to the department. This led to the conclusion that for this current proof of concept, the uncertainty from the load cell would be accepted at face value. Figures 5.10-5.21 demonstrate the uncertainty windows for two extremes of wind tunnel speed with the final processed result overlaid atop.

Figure 5.10: Comparison of phase averaged drag value to uncertainty window, AR1 circular cylinder for the 400RPM fan, 1RPM stepper

Figure 5.11: Comparison of phase averaged drag value to uncertainty window, AR1 circular cylinder for the 900RPM fan, 1RPM stepper

Figure 5.12: Comparison of phase averaged side value to uncertainty window, AR1 circular cylinder for the 400RPM fan, 1RPM stepper

Figure 5.13: Comparison of phase averaged side value to uncertainty window, AR1 circular cylinder for the 900RPM fan, 1RPM stepper
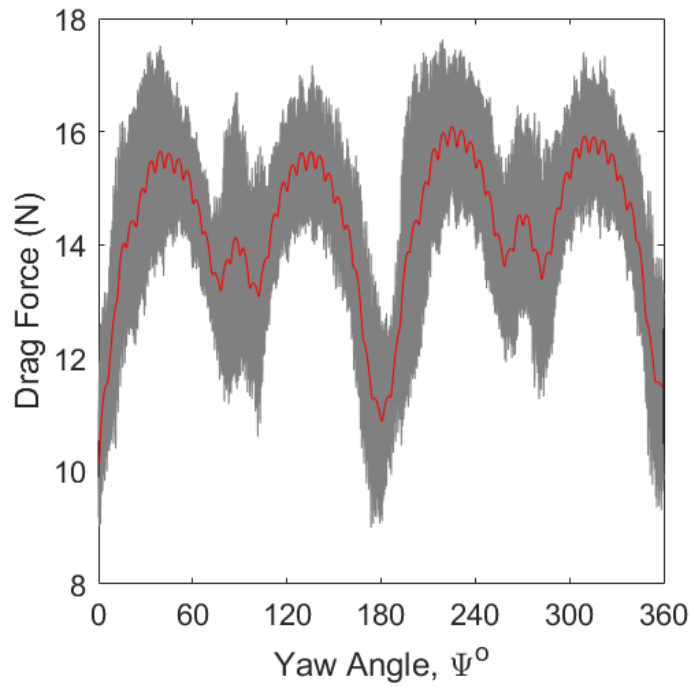
Figure 5.14: Comparison of phase averaged torque value to uncertainty window, AR1 circular cylinder for the 400RPM fan, 1RPM stepper
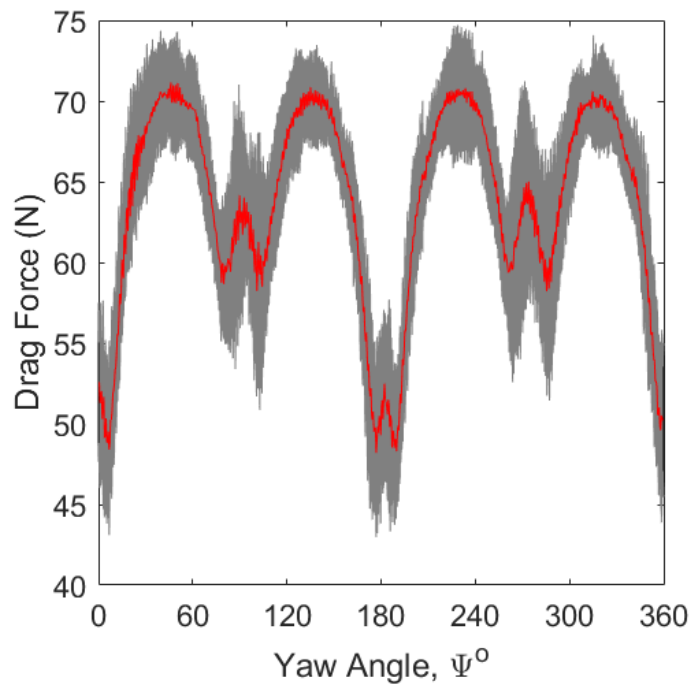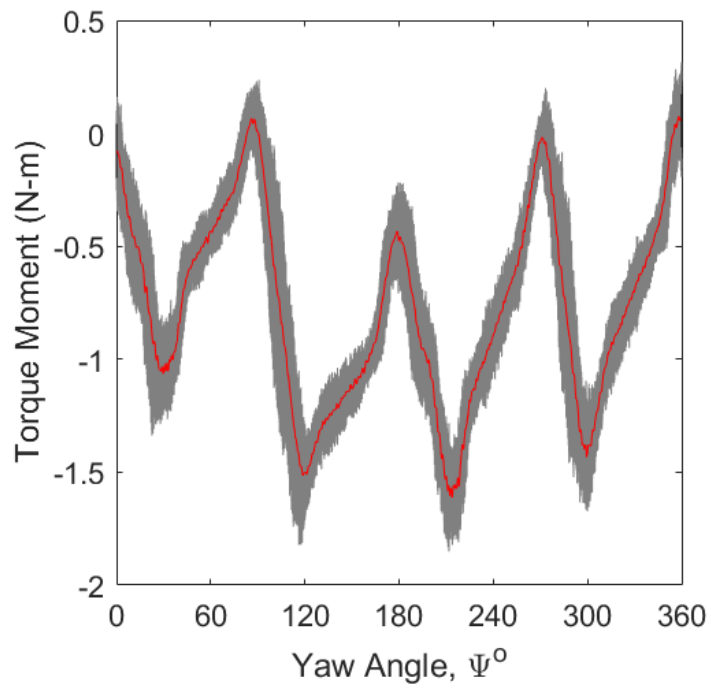

Figure 5.15: Comparison of phase averaged torque value to uncertainty window, AR1 circular cylinder for the 900RPM fan, 1RPM stepper
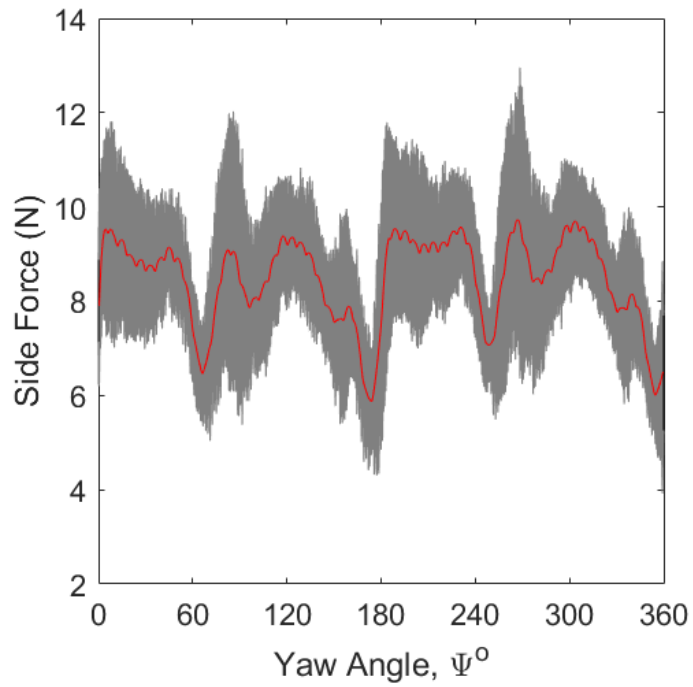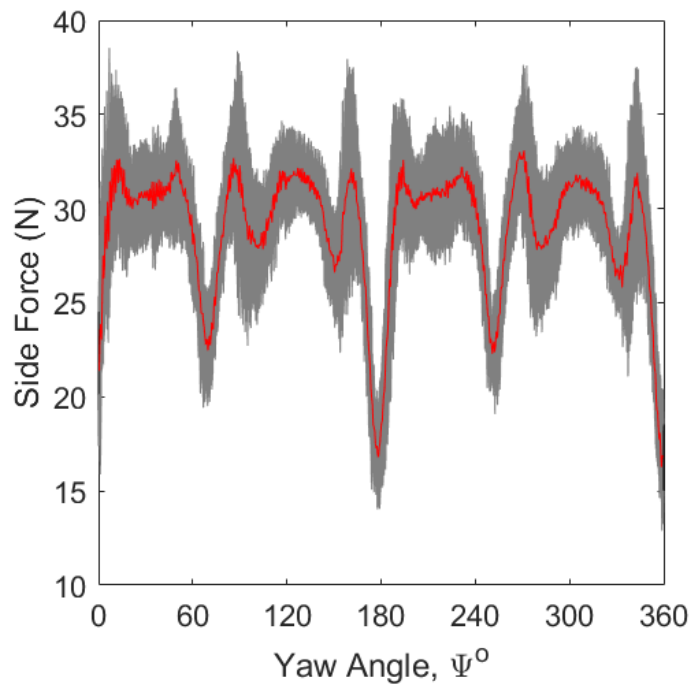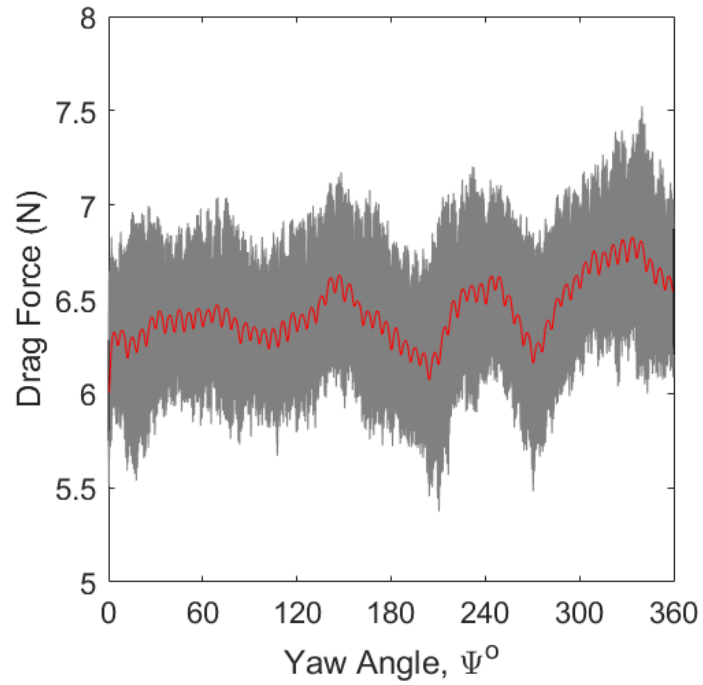
Figure 5.16: Comparison of phase averaged drag value to uncertainty window, Sphere for the 400RPM fan, 1RPM stepper
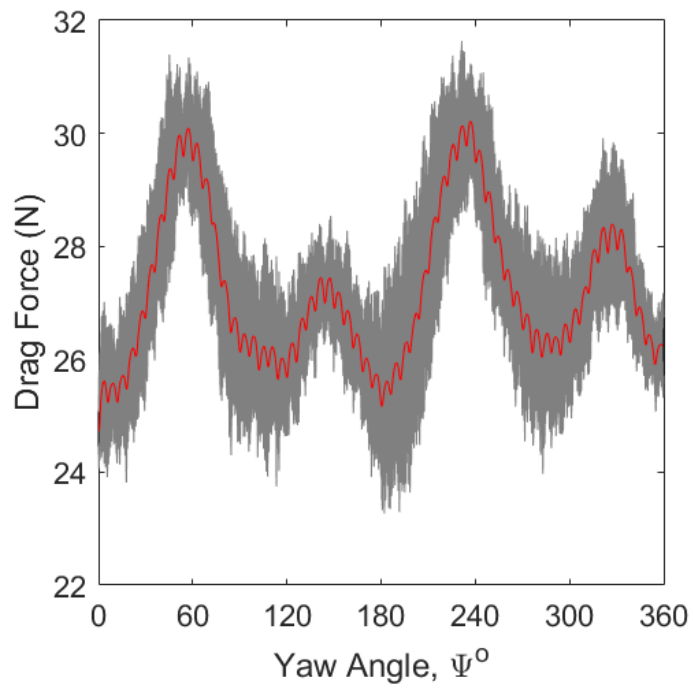
Figure 5.17: Comparison of phase averaged drag value to uncertainty window, Sphere for the 900RPM fan, 1RPM stepper

Figure 5.18: Comparison of phase averaged side value to uncertainty window, Sphere for the 400RPM fan, 1RPM stepper

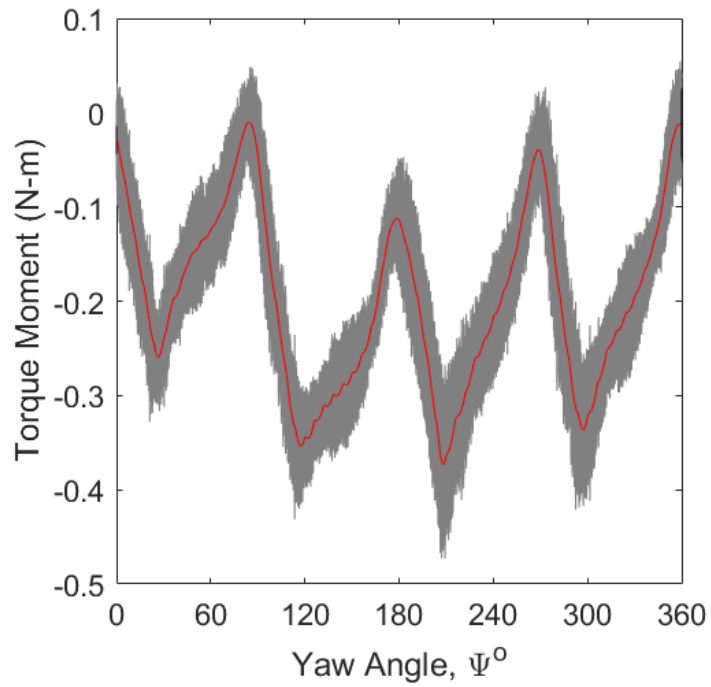Figure 5.19: Comparison of phase averaged side value to uncertainty window, Sphere for the 900RPM fan, 1RPM stepper

Figure 5.20: Comparison of phase averaged torque value to uncertainty window, Sphere for the 400RPM fan, 1RPM stepper
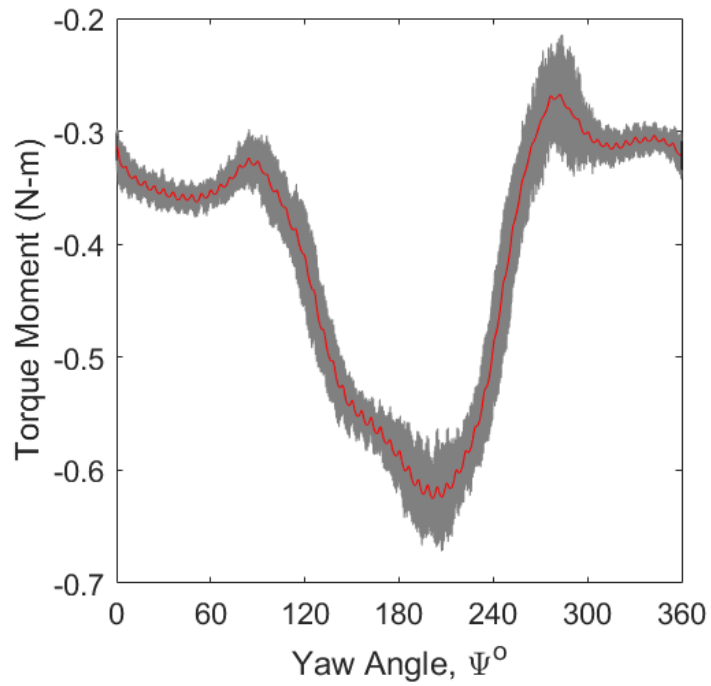
Figure 5.21: Comparison of phase averaged torque value to uncertainty window, Sphere for the 900RPM fan, 1RPM stepper

Chapter 6
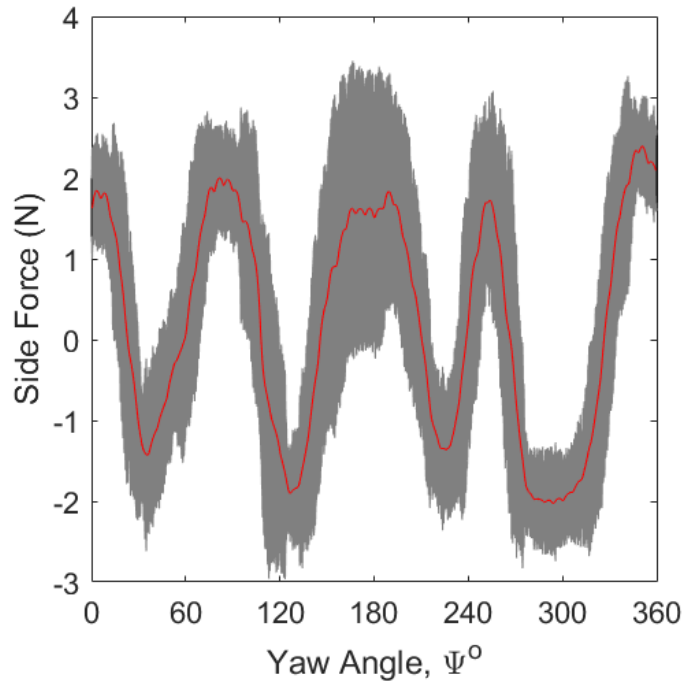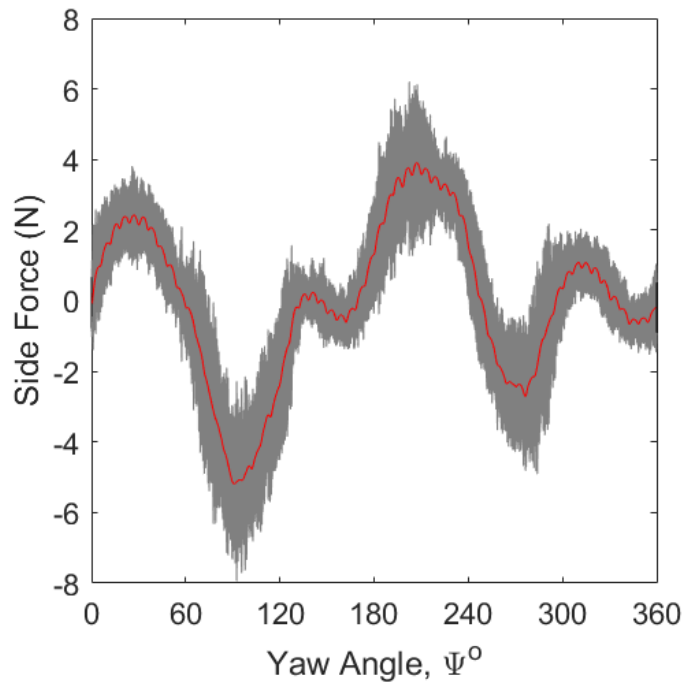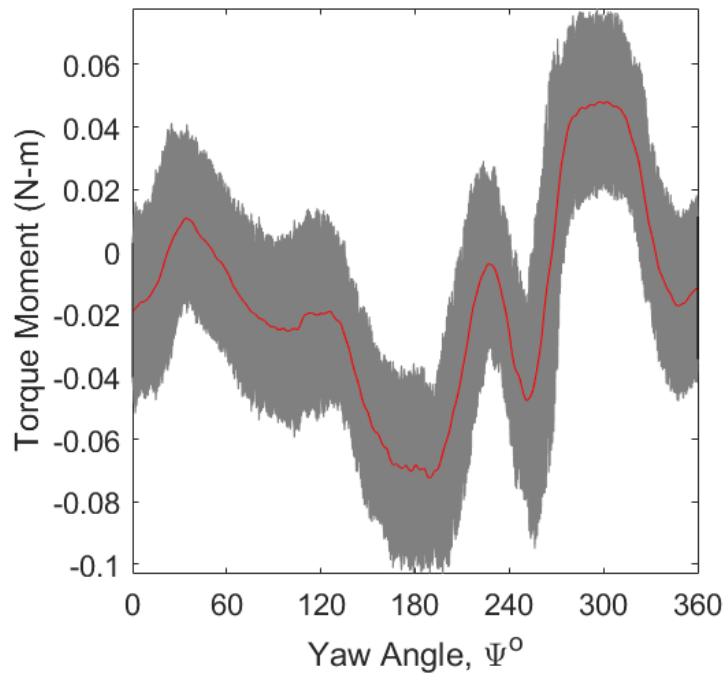
RESULTS AND DISCUSSION

Utilizing the reduced frequency variable as defined section 2.2.1, a set of test condi-
tions were developed to assess the CRT testing rig's ability to successful capture the
airloads acting on both an aspect ratio 1 circular cylinder and sphere. The results
included within this capture encompass a selection of the testing conditions as listed
in section 4.3.1. Testing of each object was broken down into two categories, 1 RPM
stepper motor rotation rate testing or variable stepper motor rotation rate testing.
The cases where the stepper motor was kept at a constant 1 RPM rotation rate were
performed for a set of 6 distinct Reynolds numbers from wind tunnel power setting
of $25 - 75\%$. A range of 1-10 RPM stepper motor rotation rate was then assessed
for the 25% and 75% conditions. Static measurements were also taken in these two
testing conditions for the aspect ratio 1 circular cylinder at a yaw resolution of 1-
degree requiring a test time of 3 hours per test. Sphere static measurements were
collected from a single 30 second average measurement at one attitude. These static
measurements are overlaid onto the CRT measurements for comparison.

6.1 AR1 Testing

Testing was conducted for the AR1 cylinder over a set range of fan speeds within the
LSWT facilities that ranged from 25-75 percent total fan power. Table 6.1 serves to
catalog the range of Reynolds numbers, wind tunnel freestream velocity, and reduced
frequency, the parameter used to assess the extent of the unsteady nature of an
aerodynamic flow, to validate that all tested conditions are within the quasi-steady

89

assumption. Velocity is determined from an average 100 data points collected at the wind tunnel in the various fan speeds that were previously listed within the test matrix. The velocity measurements themselves are determined from a total pressure and static pressure ports located within the wind tunnel test section. The ambient pressure and temperature readings are taken from a weather clock housed in the control room. These are used to determine fluid characteristics for velocity and Reynolds number calculations. The uncertainties in ambient conditions are not accounted considering the stable weather conditions.

Table 6.1: Wind Tunnel Testing Flow Characteristics

$Parameter$	$AR1$
$V(m/s)$	$16.42 - 37.91$
Re	$25301 - 546268$
$Amb.P(Pa)$	101460
$T(°C)$	22
k	$3.0x10^{-4} - 7.0x10^{-3}$

6.1.1 CR 1RPM Rotation Rate

The first area of interest of the results concerns testing where the rotation rate of the stepper motor was kept at a constant value. The parameter that is to be explored in this section of the results considers variation to the fan speed of the wind tunnel, hence Reynolds number. Before discussing the final results of the CR load maps generated, a sampling of some of the intermediate steps in the process are shown to better represent the work that is undertaken for processing each test case. Figures 6.1-6.3 illustrate the first step that is taken to take the total series of raw data measurements and convert them to a more refined sample. In these graphes, the encoder data is used to assess the starting point of a rotation and its progression through a complete revolution. This serves as the next starting point for the subsequent rotations and so on. When all rotations have been overlaid on top of each other they are visually inspected in

a plot to ensure no offset of data is present. This step of visual inspection is made easier for this particular test object as it is characterized by an expected symmetry of all three components from the first half of the rotation to the second half while also corroborating with encoder output for any indications of slippage.
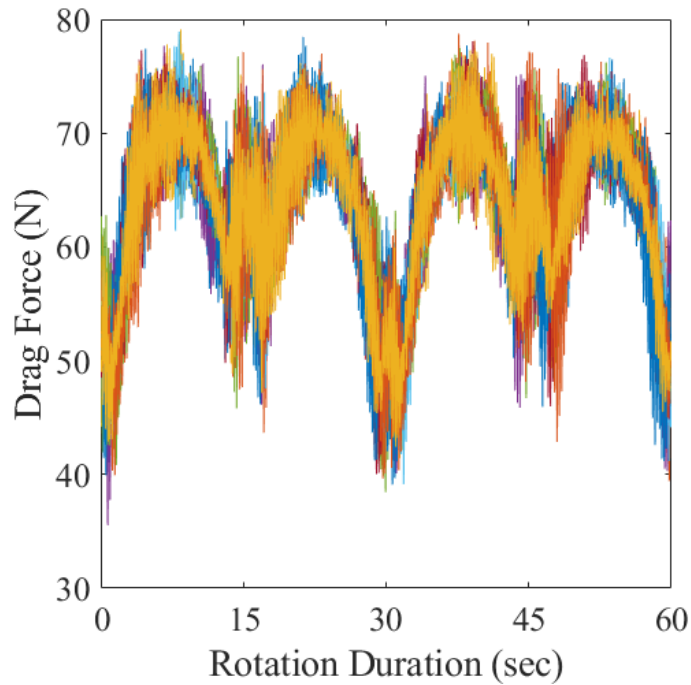
Figure 6.1: Rotations Drag, AR1, Stepper 1RPM, Fan 900RPM

The overlay excludes the initial and final rotations made by the stepper motor to ensure a constant rotation is present needed for the quasi-steady aerodynamics assumption. Following this overlay, the rotations are time averaged to result in a single vector of data points representing the average data value for each time step taken over the course of a rotation. These are represented by Figures 6.4-6.6. While the data may vastly bed reduced, it is still a poor approximation of the actual measurement acting on the cylinder. This conceptually makes sense as with each rotation being made up of 6000 data points the process of time averaging 10 given rotations culminates in only ten observations being used to collect a single data point of this refined vector of 6000 entries. To obtain a higher precision in the measurement the
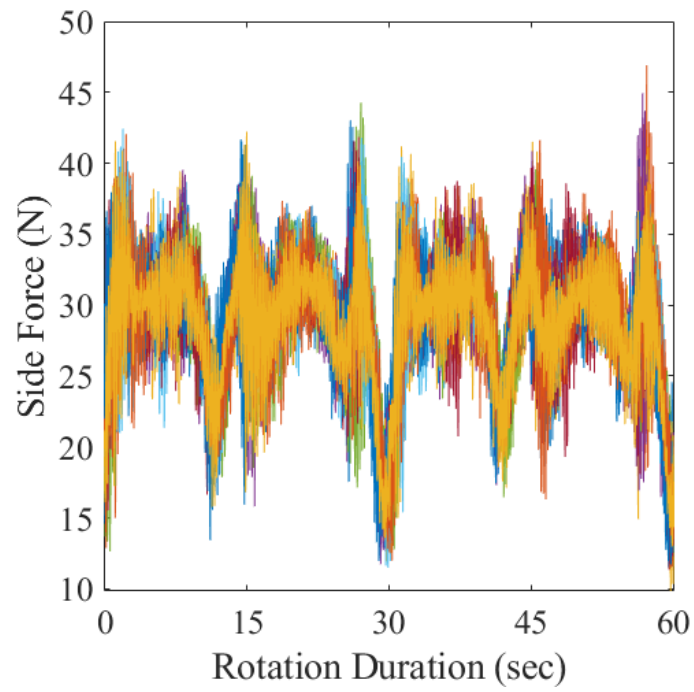
Figure 6.2: Rotations Side Force, AR1, Stepper 1RPM, Fan 900RPM
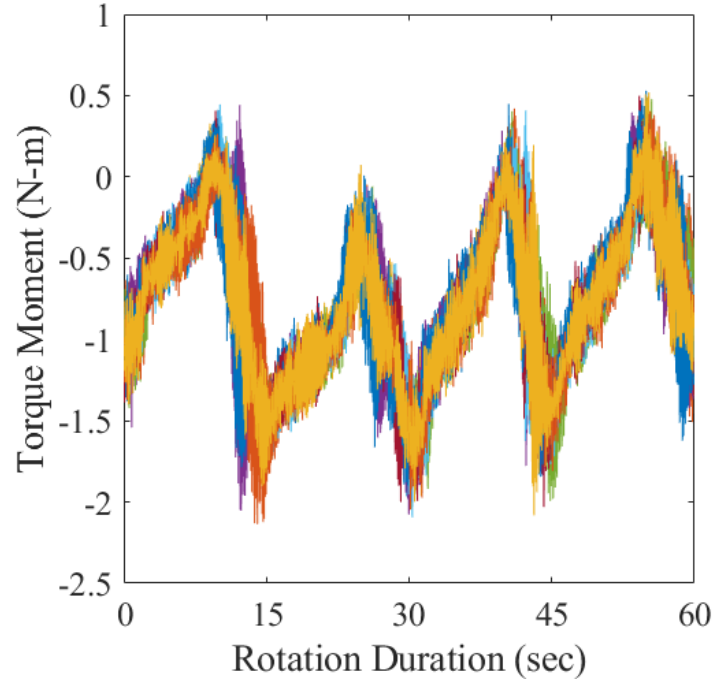
Figure 6.3: Rotations Torque, AR1, Stepper 1RPM, Fan 900RPM

final step of assembly bin-averaging (phase averaging) is employed. At the given sampling frequency of the LabVIEW interface a total of 17 data points of the time averaged vector are binned and average to produce a single data point of the finalized vector. Further increase to resolution was achieved by having the latter half of one bin serve as the first half of the following bin. This results in a 0.5 degree step size for entries of the finalized load maps. A bin made up of 17 time averaged data points, which in turn are made up of 10 raw rotational data points, becomes a total of of 170 measurements taken from the load cell reduced to a single refined value.
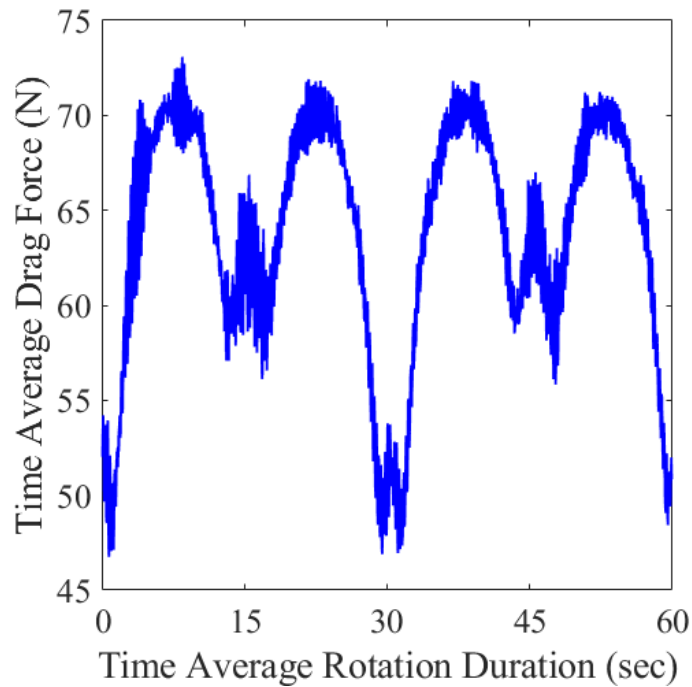
Figure 6.4: Time Average Drag, AR1, Stepper 1RPM, Fan 900RPM
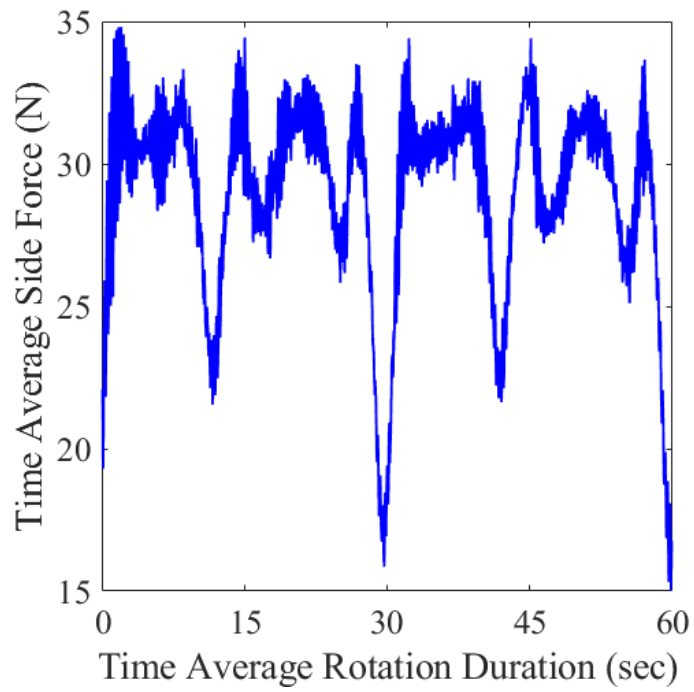
Figure 6.5: Time Average Side, AR1, Stepper 1RPM, Fan 900RPM
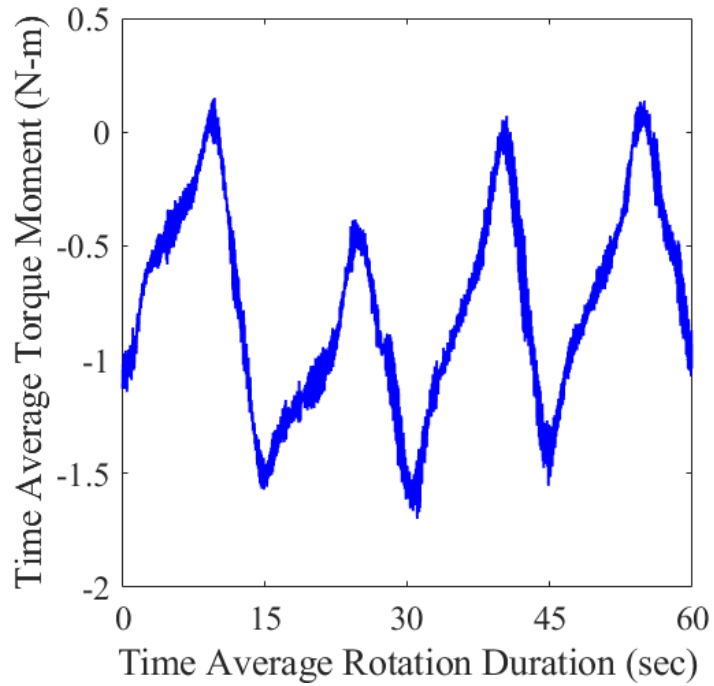
Figure 6.6: Time Average Torque, AR1, Stepper 1RPM, Fan 900RPM

Figures 6.7-6.9 culminate the labor undergone by the CR technique into a set of the three loading conditions of interest at a variety of tunnel speeds. An interesting behavior that is observed is the development of greater nonlinear behavior for the test object models at higher tunnel speed. This can be explained by several factors. At these higher wind tunnel speeds the reduced frequency of the problem decreases in value making it closer in value to a complete static aerodynamic problem. This would result in the CR technique being better able to capture specific nonlinear characteristics that are present from the test object than at lower speeds. This behavior would also be expected to not be as present at lower speeds which is supported from the graphs. A promising sign of successful implementation of the CR technique is the symmetry of loading, especially for that of drag in Figure 6.7. The crests of any one given test condition appear to be consistent across the complete load map.
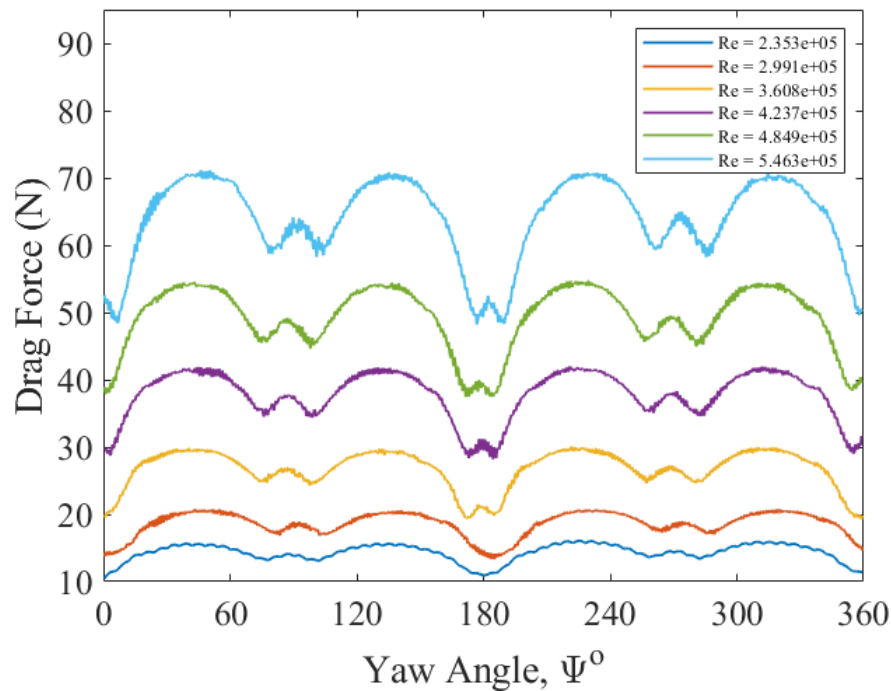
Figure 6.7: Fan Variation: Drag Force, AR1, Stepper 1 RPM
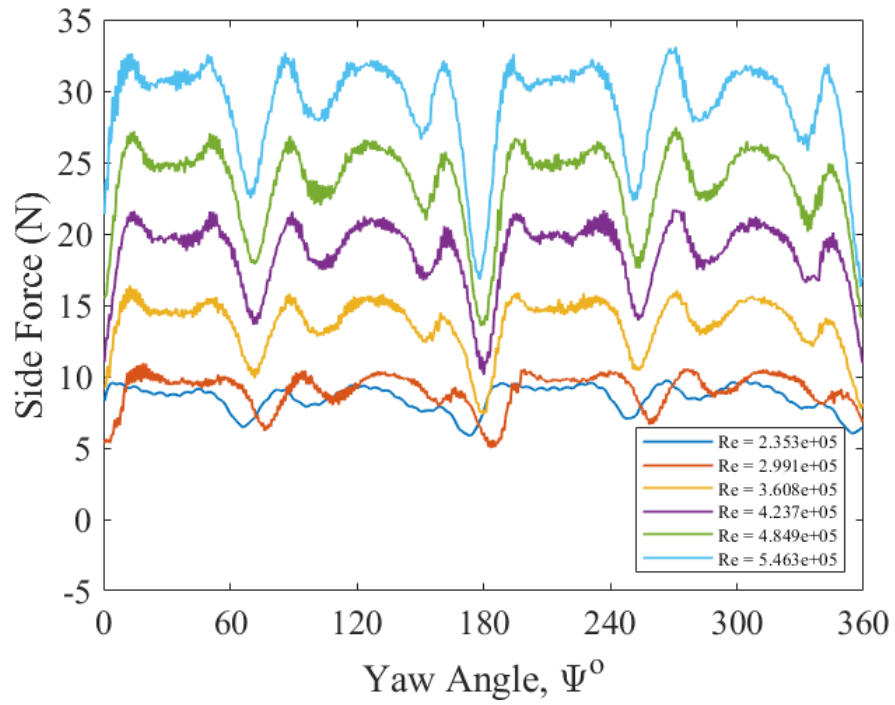
Figure 6.8: Fan Variation: Side Force, AR1, Stepper 1 RPM
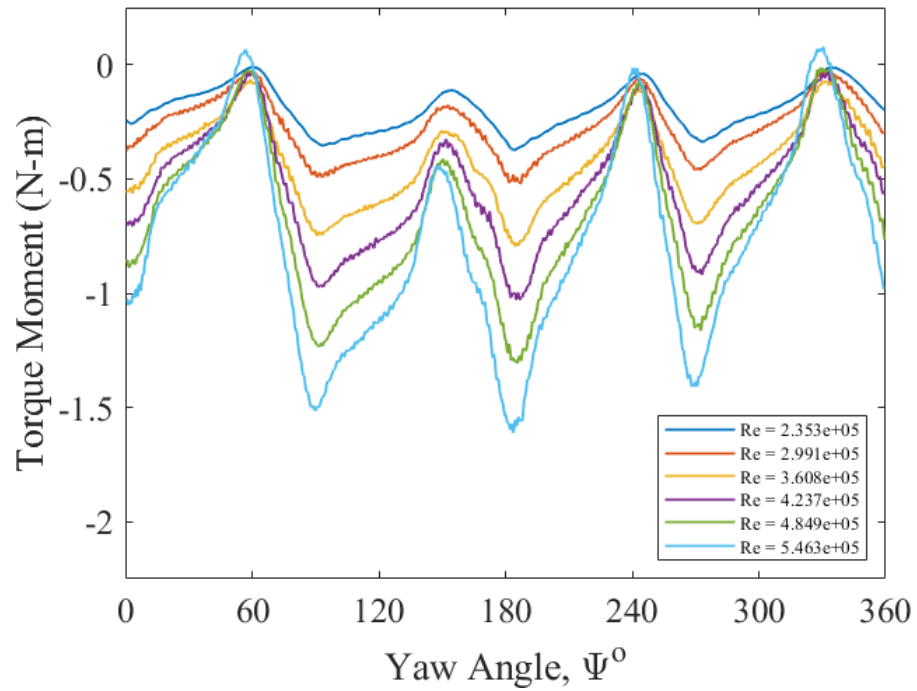
Figure 6.9: Fan Variation: Torque Moment, AR1, Stepper 1 RPM

6.1.2 Rotation Rate Variation

The next focus of testing for the CR testing rig considered how the impact of variation to the rotation rate of the stepper motor would impact the ability to obtain measurements in accordance to what would be expected from truly static measurements. This process was conducted for a span of stepper motor speeds of 1-10 RPM. Wind tunnel fan speeds of 400 and 900 RPM was used as these two made up the extreme ends for all testing. Given that angular velocity and fluid velocity both help determine reduced frequency it would be expected that the most interesting cases would be that of the low speed fan with high stepper motor rotation and low stepper motor rotation with high fan speed. The simple reasons being this should show the case with the highest reduced frequency followed by the lowest respectively. When looking at the low fan speed cases of Figures 6.10-6.12 traces of this can be witnessed. The regions where the most significant divergence to the static measurements appear to fall along the points in the load map where the cylinder would be positioned with its end caps facing the flow, see 90 degree on Figure 6.10. The non linear behavior that is clearly seen by the 1-4 RPM stepper tests is non-existent to the 10 RPM case.

A point worth mentioning when considering the success of this testing rig to capture quasi-steady measurements concerns the load cell that was utilized and the amount of uncertainty present for measurements taken of these objects. This is most apparent in the low speed fan case of Figures 6.10-6.12, for example with a Total Drag uncertainty of around 6 Newtons for a load map peak to peak variations also of 6 Newtons. This leads the more important assessment to be how closely a particular case follows the trend of static measurements opposed to actual magnitudes. Any further work on this project should make serious consideration for improvements to the current load cell setup to reduce this component of total uncertainty. This behavior is seen to match well with the results of the high speed fan tests of Figures 6.13-6.14. The higher wind
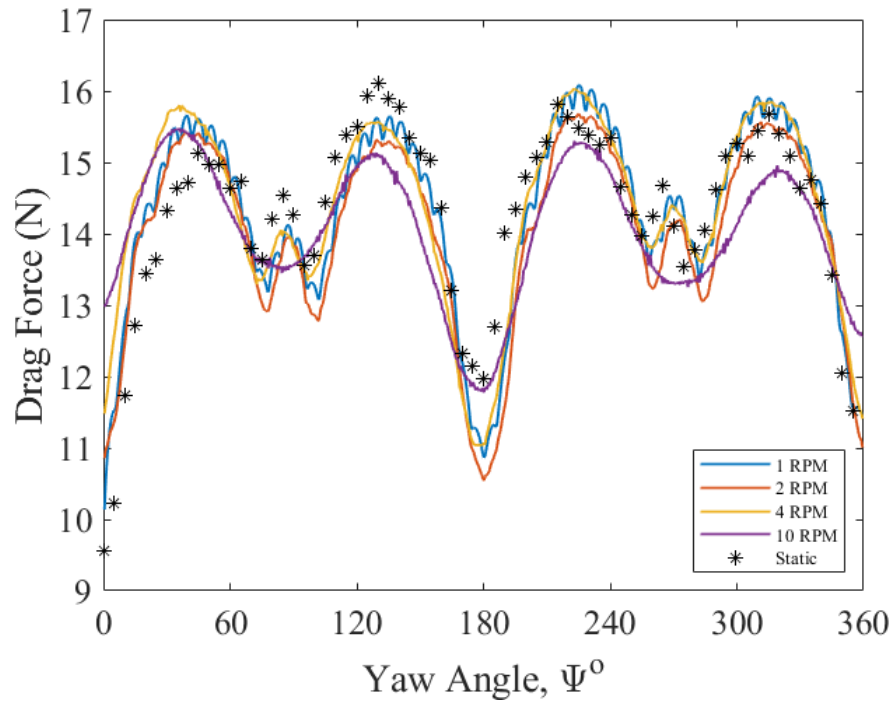
Figure 6.10: Stepper Variation: Drag Force, AR1, Fan 400RPM
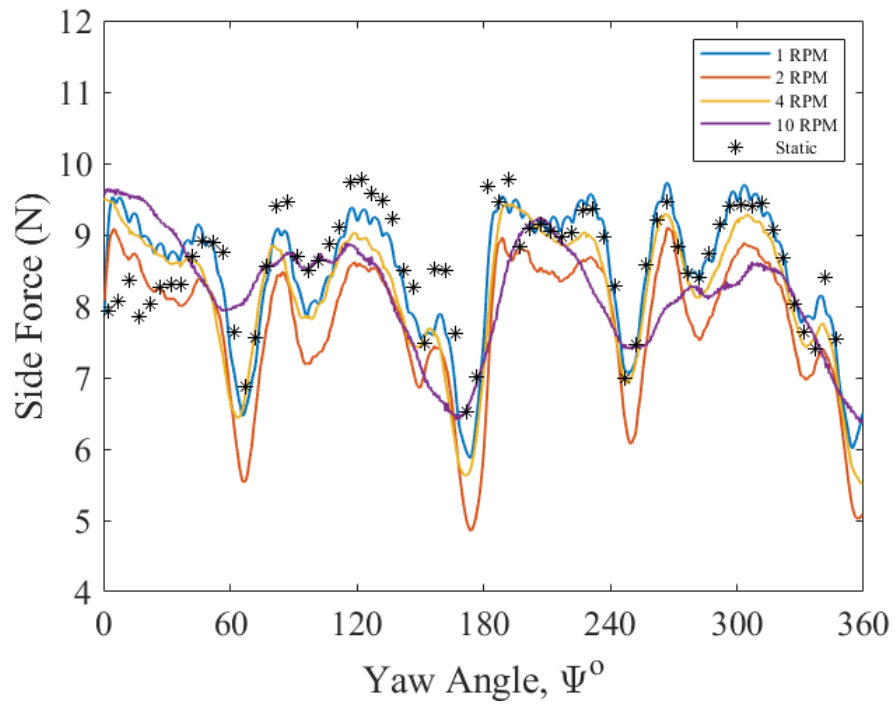
Figure 6.11: Stepper Variation: Side Force, AR1, Fan 400RPM
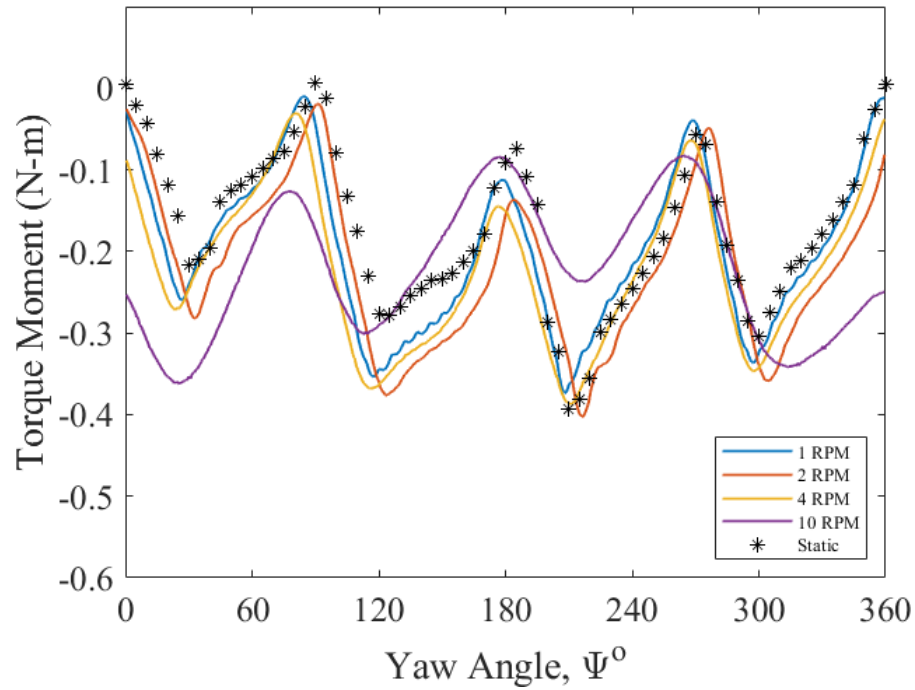
Figure 6.12: Stepper Variation: Torque Moment, AR1, Fan 400RPM

tunnel speed lowers the reduced frequency of each test case which is supported by the higher stepper motor RPM cases providing a better matching to the non linear behavior portions of the static measurements. The 1 RPM case still delivers the best approximation with key highlights being at the 180 degree portion of Figure 6.13 and overall superior behavior of Figure 6.14 than compared with the 10 RPM case.
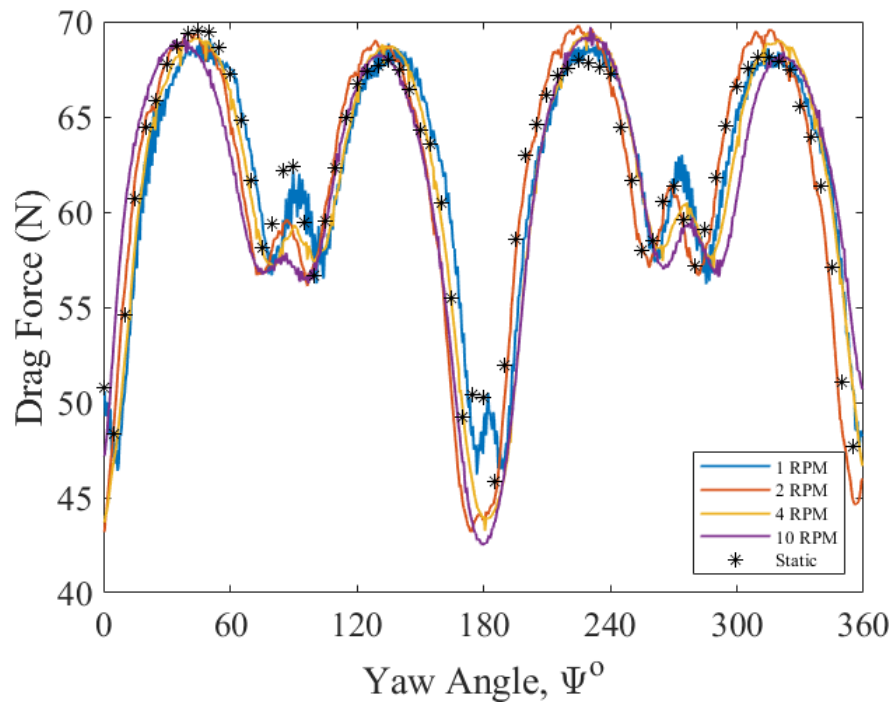
Figure 6.13: Stepper Variation: Drag Force, AR1, Fan 900RPM
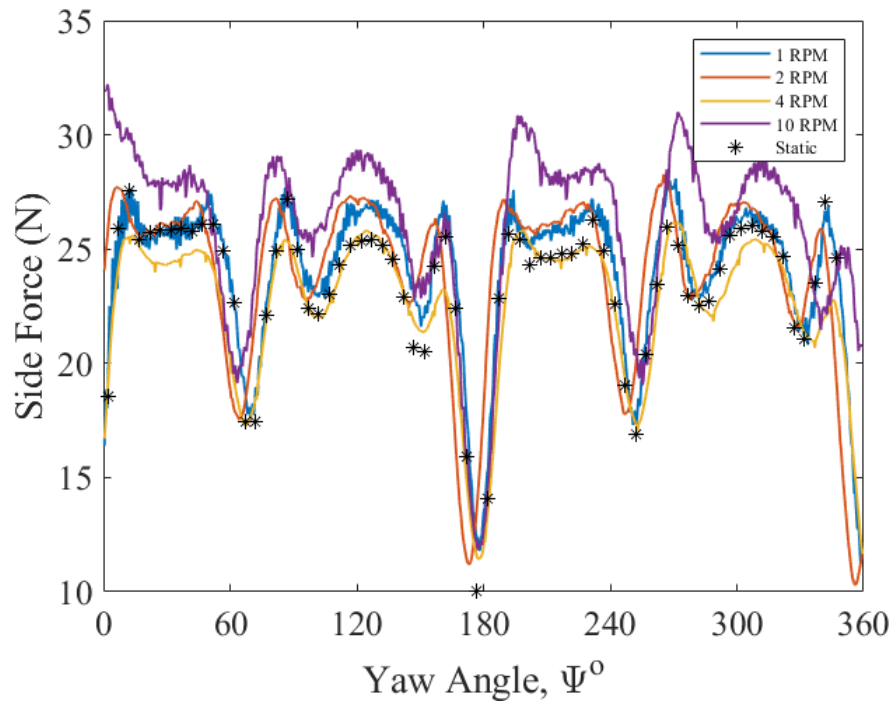
Figure 6.14: Stepper Variation: Side Force, AR1, Fan 900RPM
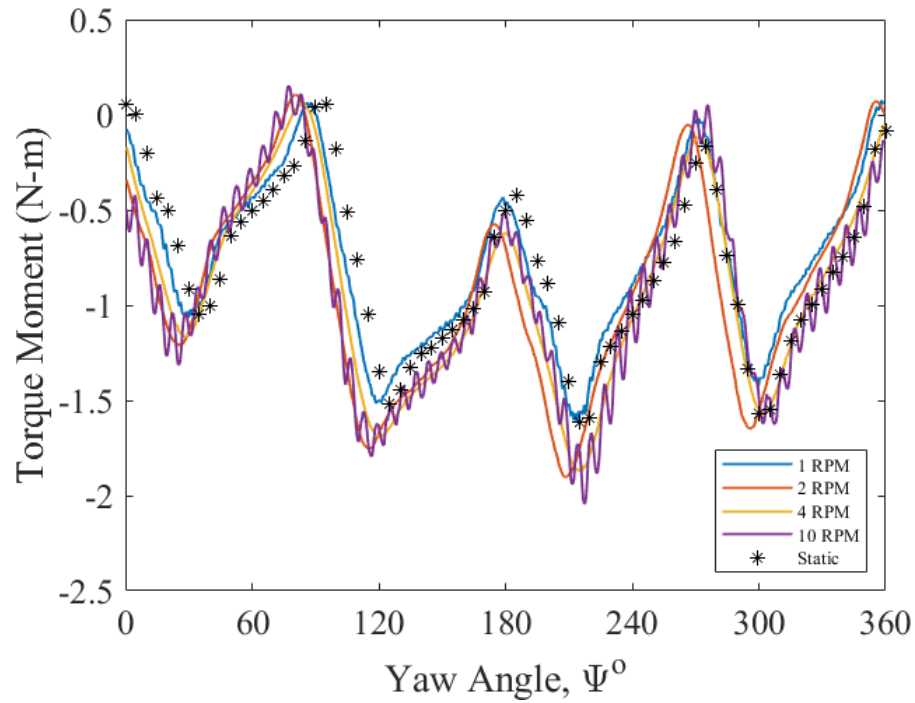
Figure 6.15: Stepper Variation: Torque Moment, AR1, Fan 900RPM

6.2 Sphere Testing

Following the completion of testing for the AR1 circular cylinder the same set of test conditions was repeated for the sphere model. The test of the sphere offered a unique test for the CR testing rig as a sphere allows the same orientation to the freestream regardless of attitude change. This would result in all components staying constant over the complete rotation for a static measurement case. Static measurements instead of taking the 3 hour approach done for the AR1 cylinder made use of this fact and instead relied on a single 30 second average reading at one attitude.

6.2.1 CR 1RPM Rotation Rate

When stepper motor rotation is held constant at 1 RPM as previously done for AR1 cylinder, the corresponding results are shown in Figures 6.16-6.18. When specifically looking at the drag and torque plots we witness the same refinement detail captured by the CR testing rig at highers speeds correlating to lower reduced frequencies. This suggests the surface of the sphere would not be perfectly uniform for a complete revolution. This fact is validated by the test object in question having a small engraving on on side of the sphere with a company logo. The side force unlike any previous plots displayed what seemed to be no truly definite pattern between the various wind tunnel speeds. The side force that would be expected by for the load cell in this orientation should remain essentially zero for the complete rotation. While it does appear that zero is the average value across each test as they each appear to oscillate around that value the higher wind tunnel speed, which should provide the clearest picture, has the largest amplitude away from the value of zero. All values are within the uncertainty window given this load cell used so for better understanding it may be required that future work reexamines side force of this object with a more suitable load cell than that of the ATI mini58.
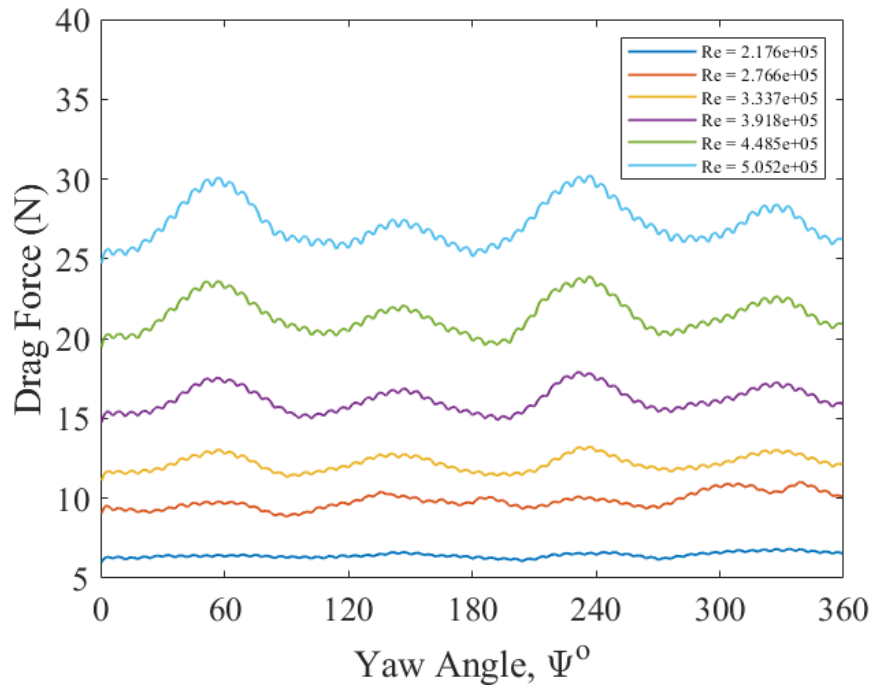
Figure 6.16: Fan Variation: Drag Force, Sphere, Stepper 1RPM
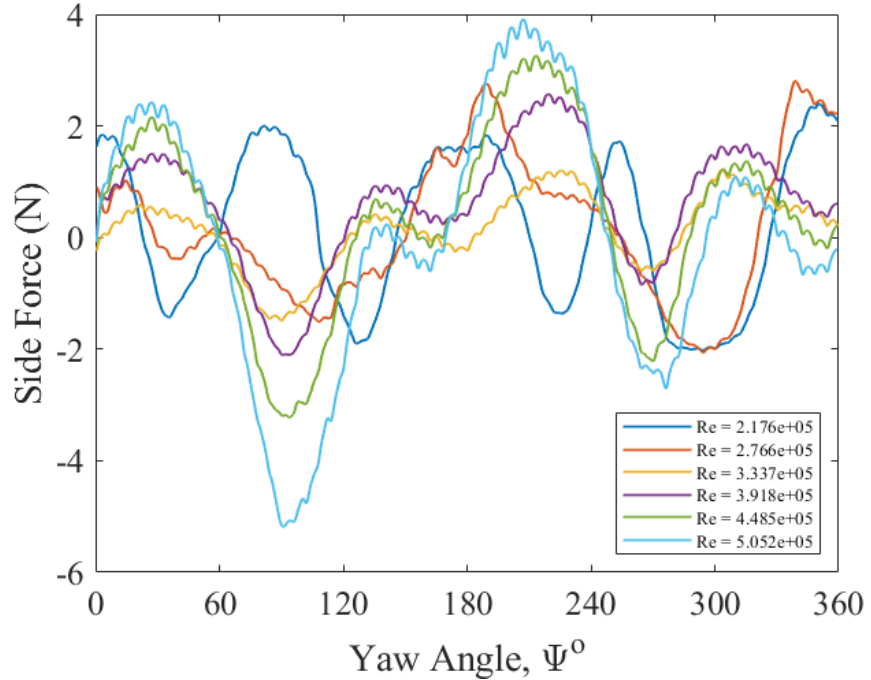
Figure 6.17: Fan Variation: Side Force, Sphere, Stepper 1RPM
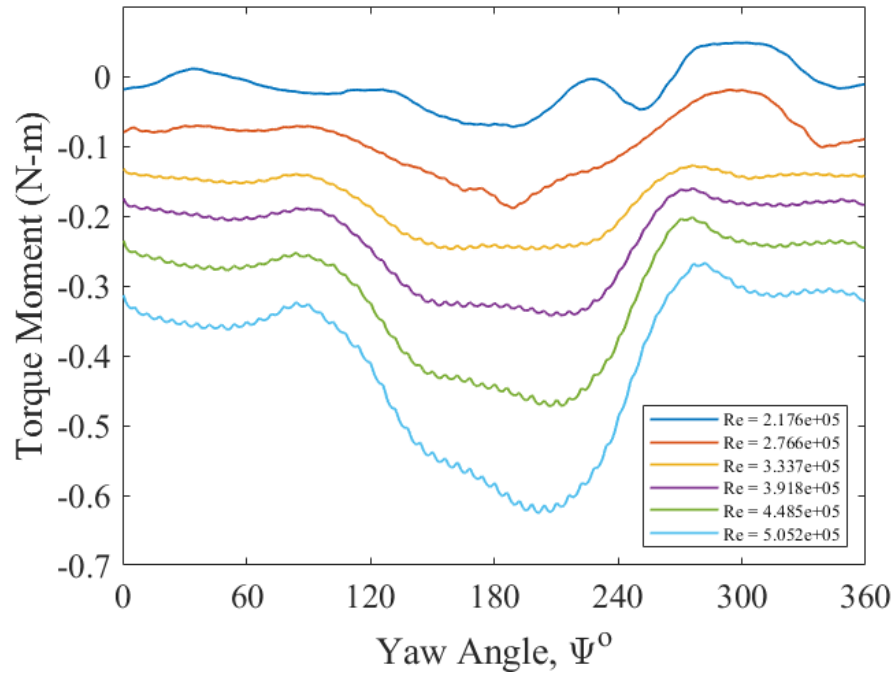
Figure 6.18: Fan Variation: Torque Moment, Sphere, Stepper 1RPM

6.2.2 Rotation Rate Variation

Results of RPM manipulation of the stepper motor of the sphere do not paint as clear of a picture from that of the tests conducted from the AR1 cylinder. One factor that is driving this is from the static measurement of the sphere only coming from a single attitude measurement. This fails to capture any non uniform behavior that CR is picking up at low RPM cases as shown in Figures 6.19 and 6.21. A future task of this project would be to conduct static testing in the same manner as that of the AR1 testing. This was not done for this project as the sphere was a secondary supplemental object and time did not allow for those each two 3 hour tests to be conducted. Looking to Figure 6.19 the static average of 5.4 Newtons is well within the uncertainty windows of all test cases shown. The average of -0.1 Newtons and -0.08 Newton meters for static side force and torque is best followed by the 10 RPM case. This could be explained by the loss of capturing finer detail leading to a more

averaged value for side force and torque considering the whole sphere in the same realm that the static measurement was taken. Figures 6.22-6.24 for the high speed case experience the small behavior of most closely matching the static measurement. Interestingly for Figure 6.24 the static measurement was found to be -0.33 Newton meters which closely matches all cases for the first 60 degrees of rotation. This would make sense since the static attitude matches the starting orientation of the rotation. The subsequent dip in all test cases beyond 60 degrees indicates non uniform surface which was already found to be true. This further warrants the need for the retesting of static measurement using the full three hour format.
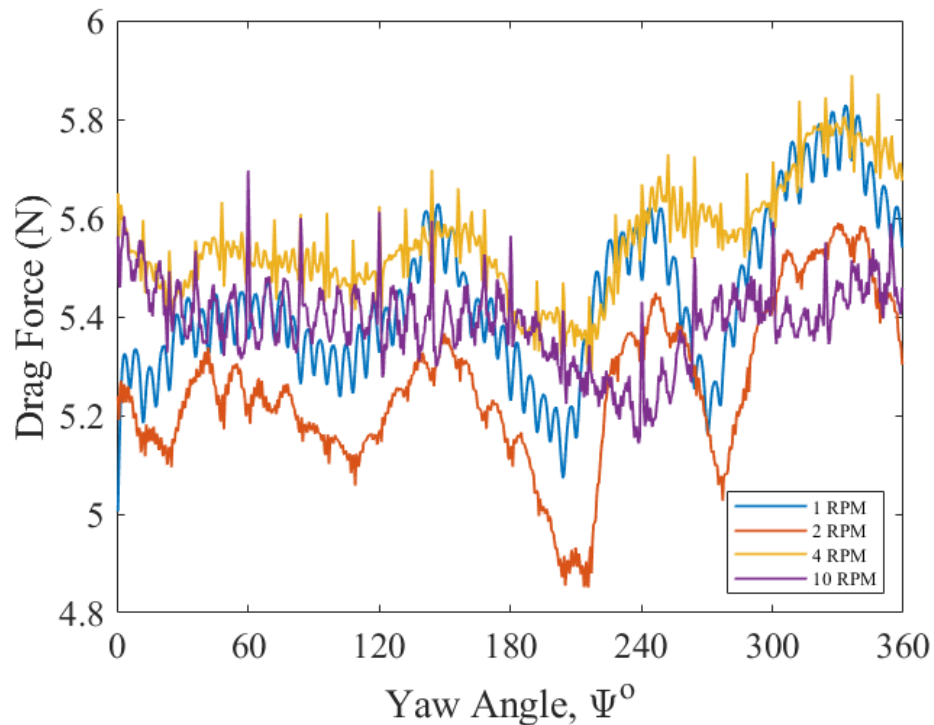
Figure 6.19: Stepper Variation: Drag Force, Sphere, Fan 400RPM
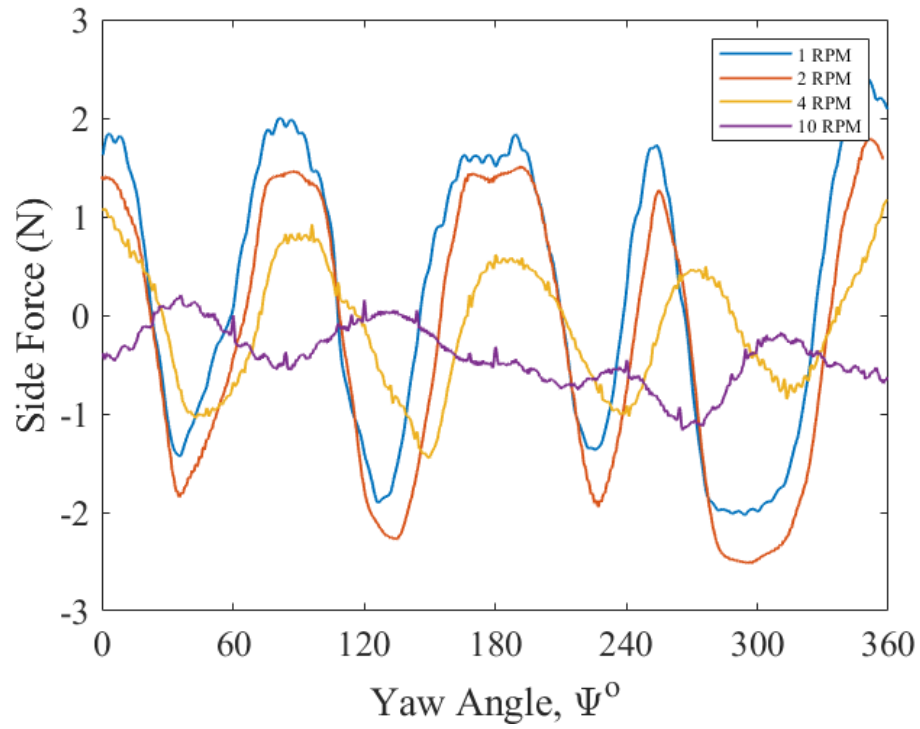
Figure 6.20: Stepper Variation: Side Force, Sphere, Fan 400RPM
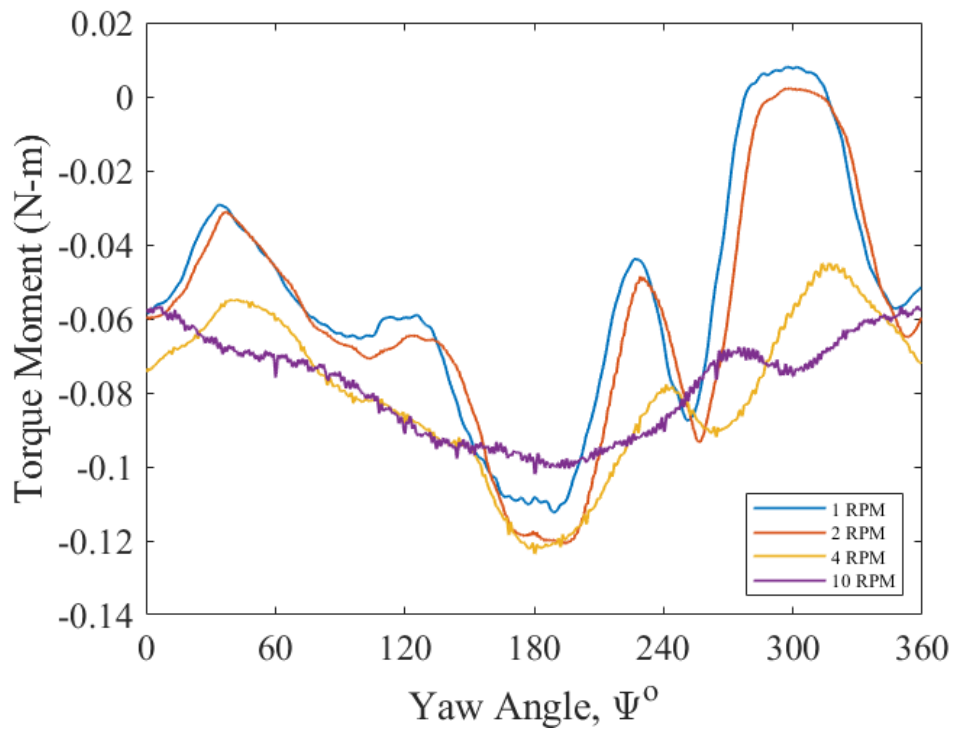
Figure 6.21: Stepper Variation: Torque Moment, Sphere, Fan 400RPM
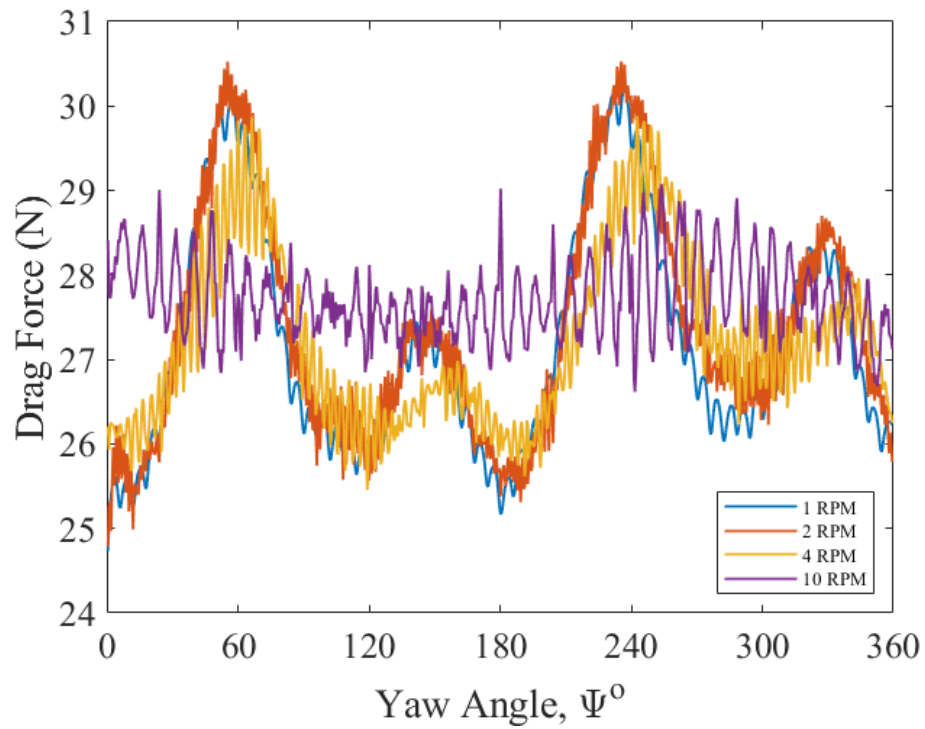
Figure 6.22: Stepper Variation: Drag Force, Sphere, Fan 900RPM
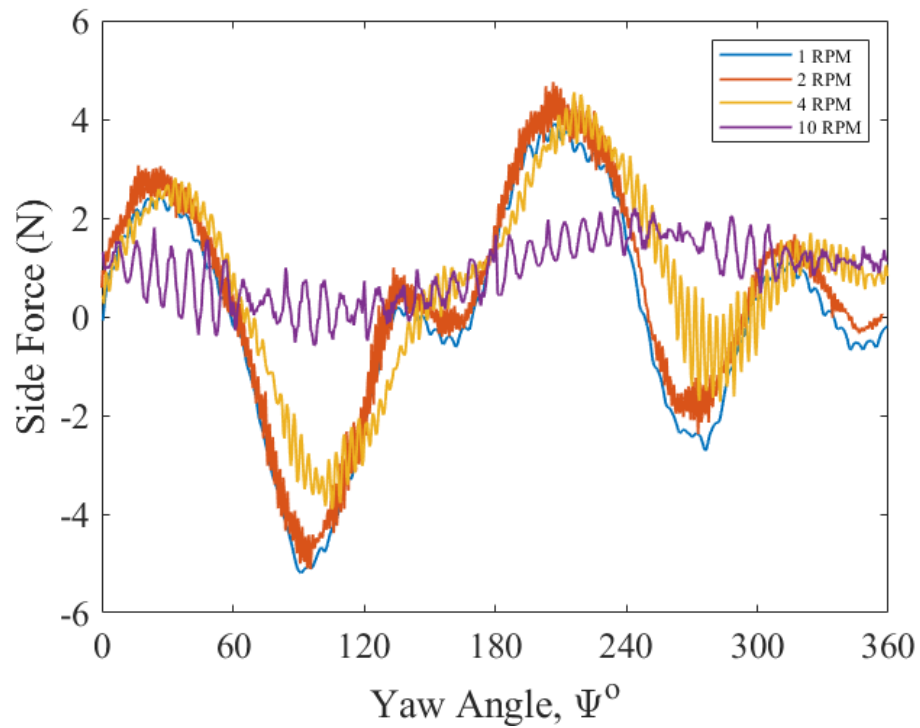
Figure 6.23: Stepper Variation: Side Force, Sphere, Fan 900RPM
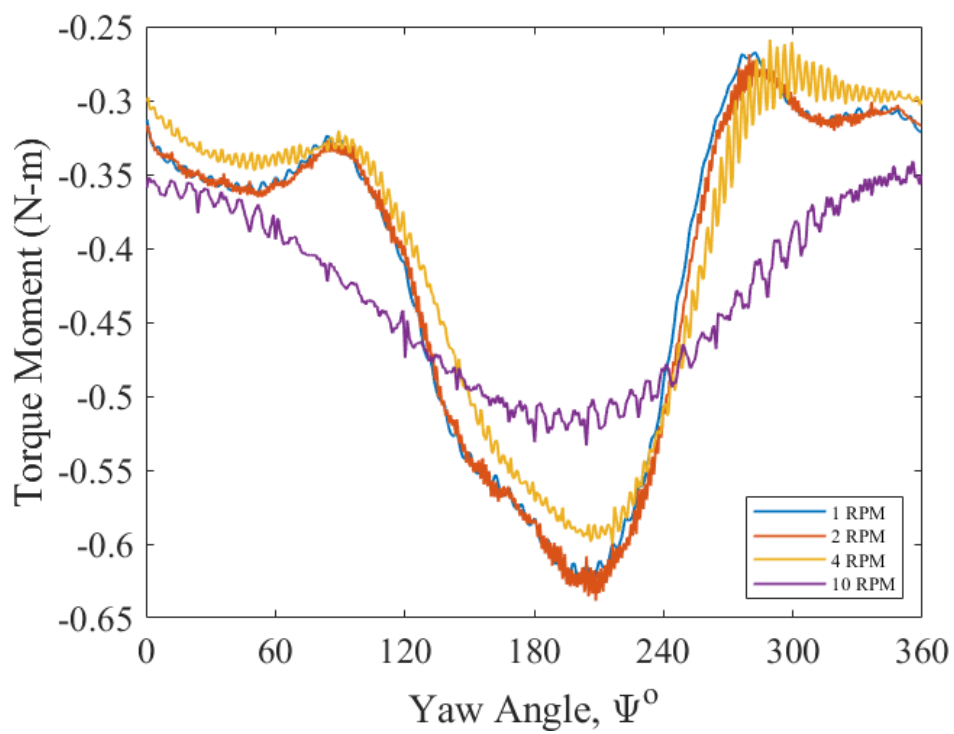
Figure 6.24: Stepper Variation: Torque Moment, Sphere, Fan 900RPM

Chapter 7

CONCLUSION AND FUTURE WORK

7.1 Conclusion

The objectives of this thesis work was to provide evidence for the feasibility for the incorporation of a CRT testing rig within the current infrastructure available here at Cal Poly on the scale of a proof of concept. A goal for improvement of slippage monitoring was set to provide further fidelity than was previously offered at Georgia Tech. Categorizing the uncertainty of the completed system and demonstrated repeatability were required to validate this method for use within the LSWT for capturing complete high resolution load maps. A quasi-steady assumption is established using the reduced frequency variable to help identify test conditions that can be aided with use of CRT. Background knowledge was obtained from work previously accomplished at Georgia Tech to identify desirable load map profiles for certain test objects and general configuration for testing rig. Individual components for the Cal Poly test rig are detailed with physical and digital interfaces as to how they can be properly incorporated using department facilities. Testing procedures are developed to provide repeatable and consistent processes for collecting and processing load cell data. Uncertainty is evaluated between components specific to the data sets collected and uncertainty associated with systemic components like the load cell. Results for the determined test matrix are provided with ability to closely match static measurements taken through a method of a much higher time commitment.

This method serves as a means of obtaining quick aerodynamic load measurements using 6-DOF load cell mounted to a stepper motor housing. This system allows for high resolution load maps applied to an arbitrary number of test bodies. The continuous motion of this method reduces the amount of testing time that would require to manually change the attitude of the test object and measure static readings with traditional means. This offers a great opportunity to increase the feasibility to test more complex bodies at a fraction of the time. Complex bodies that would not be possible to test in current allotted times of lab sections at this level of resolution. While this thesis serves as proof of concept for this testing apparatus, a number of future tasks were identified to bring this current implementation closer to a full fledged means for accurate testing at Cal Poly. Results and conclusions for this phase can only provide validation to a proof of concept and not provide insight into the actual airloading of an object at this time. This project is intended to continue and evolve in the future following the submission of this thesis. The implementation arrived at the conclusion of this current work will not be the final version of this testing rig. Specific conclusions of this project consist of:

1. The continuous rotation method offers measurement of quasi-steady loads acting on a given test body, with higher resolution yaw attitude change of 0.5 degrees. Complete load maps can be generated in short testing duration to offer an increased feasible for researchers to test unique objects at small attitude change. Each of these tests take 12 minutes as compared to 3 hours for static measurements.

2. Uncertainty summation indicates the largest source being from the load cell. In the current scope of this project the load cell uncertainty is accepted as a given. The load cell used for the project is the one that was available for use at the LSWT. The sensing range of the load cell is far exceeding the range the

tests conducted will inhabit making it ill-fitted for use of this technique. Future projects focused on utilizing the finalized implementation of the test rig will benefit from purchase of a lower sensing range load cell or the construction of an in-house load cell tailored for the desired test range.

3. The statistical uncertainty that is indicative of the repeatability of loads between the rotations is in a reasonable range. It shows confidence that with an increase in the number of rotations (experiments), this uncertainty can be lowered further. Although the overall uncertainty in the measured loads is heavily dependent on the choice of load cell ranges, the current set up sufficiently captures the load variations over full 360 degrees of rotation. Drag force, side force, and torque moment values for total uncertainty are 8.856 N, 8.860 N, and 0.678 N-m respectively. The same conclusion is made for load cell uncertainty with values as 8.750 N, 8.750 N, and 0.674 N-m. Statistical uncertainty was also individually found to be 1.368 N, 1.395 N, and 0.061 N-m.

4. Encoder data can assess progression of rotation of test object and presence of slippage and location on a rotation. No evidence of slippage has been observed within the encoder resolution of 6 pulses in one second corresponding to 6 degrees rotation in one second at 1 RPM of stepper motor.

5. Reduced frequency effects provide justification that all tested cases can be assessed using the quasi-steady aerodynamics assumptions as the range of $3.0x10^{-4}-7.0x10^{-3}$ are all within the $0 < k \leq 0.5$ requirement.

7.2 Future Work

The future work on this testing rig requires it largest attention towards a refinement to the total uncertainty the system currently offers. The expected sensing range of the ATI load cell does not provide the needed range to reduce uncertainty for test objects sized within the LSWT test section. Progress towards the purchase and installation of another lower sensing range load cell, despite potentially having a higher measurement percent uncertainty, can greatly reduce the largest source of uncertainty currently found in the project. Additional testing and collection of more cases with current models, especially the sphere, as well as new models will be key to moving this program to its next phase as use as a quick collection tool for the building of a catalog of various tested objects. This catalog of tested objects will provide future students a database to which they can construct software for the estimation of untested objects through knowledge of tested ones. Static testing of the sphere will help to better understand how well CR was able to capture details of the test object geometry. The float valve did provide an easy way to obtain a sphere of that needed size but, due to non uniform surface other means of creating a sphere test body for the CR technique should be explored. Included within the list below are recaps of major future tasks as mentioned above with the addition of other tasks that will serve for the general improvement, or refinement, of the the continuous rotation technique testing rig from the preliminary proof of concept reached with this thesis.

- Sensing range and full-scale measurement uncertainty percentage trade study for determination of proper load cell implementation to lower total uncertainty.

- Sphere static testing using same testing structure as aspect ratio one circular cylinder static testing.

- Incorporation of tests conducted on test bodies of uniform material and finish, unlike the test bodies used in this proof of concept that consisted of multiple materials or asymmetry within the finished surface. An example of this would be to use a McMaster purchased sphere for use as the sphere test object.

- Stepper motor noise testing in absence of wind tunnel operation.

- Variable test body weight testing for further analysis of stepper noise source and possible removal without use of filter.

- Further assessment of experimental design considering factors of model size, support rod interference, and ideal test body location.

- Data collection for tare readings of support rod.

- Further processing data to be represented as Fourier approximation.

BIBLIOGRAPHY

[1] A2 wind tunnel, https://a2wt.com/cycling, 2020.

[2] Bluff body, viscous flow characteristics: Immersed bodies. Technical report, Louisiana Tech University.

[3] Cal poly wind tunnel refurbishment, https://thinkflip.tumblr.com/post/123688645978/cal-poly-low-speed-wind-tunnel-refurbishment-week.

[4] Drag of blunt bodies and streamlined bodies. Technical report, Princeton University.

[5] P series nema 23 stepper motor cad model, 29 2019.

[6] P series nema 23 stepper motor data sheet, 29 2019.

[7] Digital stepper driver, 29 2022.

[8] Ati mini58 load cell specifications manual, 29 2023.

[9] F/t sensor data acquisition (daq systems manual, 29 2023. Document : 9620-05-DAQ.

[10] R. Almeida, D. Vaz, A. Urgueira, and A. Borges. Using ring strain sensors to measure dynamic forces in wind-tunnel testing. *Sensors and Actuators A: Physical*, 185:44–52, 2012.

[11] T. Asai, K. Seo, O. Kobayashi, and R. Sakashita. Fundamental aerodynamics of the soccer ball. *Sports Engineering*, 10:101–110, 2007.

[12] P. Bearman. On vortex shedding from a ciruclar cylinder in the critical reynolds number regime. *Journal of Fluid Mechanics*, 37:577–585, 1969.

[13] P. Bearman. Development in the understanding of bluff body flows. *JSME International Journal*, 41:103–114, 1998.

[14] L. Bruno, D. Fransos, N. Coste, and A. Bosco. 3d flow around a rectangular cylinder: A computational study. *Journal of Wind Engineering and Industrial Aerodynamics*, 98:263–276, 2010.

[15] J. Cermak. Wind-tunnel development and trends in applications to civil engineering. *Journal of Wind Engineering and Industrial Aerodynamics*, 91:355–370, 2003.

[16] L. Cicolani and M. Ehlers. Modeling and simulation of a helicopter slung load stabilization device. In *Proceedings of the American Helicopter Society 58th Annual Forum*, Montreal, Canada, June 2002.

[17] C. Cueto. Design and manufacturing of a test rig for continuous wind tunnel load measurements. Technical report, California Polytechnic State Univeristy, 2023.

[18] N. Delany and N. Sorensen. Low-speed drag of cylinders of various shapes. Technical report, NACA, 1953.

[19] M. Dubois. Six-component strain-gage balances for large wind tunnels. In *Proceedings of the Fourth SESA International Congress on Experimental Mechanics*, Boston, MA, May 1980.

[20] N. Findanis and N. Ahmed. *Wind Tunnels and Experimental Fluid Dynaimcs Research*. InTech, 2011.

[21] A. Forbes, V. Raghav, M. Mayo, and N. Komerath. Rotation effects on hub drag. In *Proceedings of the ASME 2013 International Mechanical Engineering Congress and Exposition*, San Diego, CA, Nov 2013.

[22] J. Freund and M.-G. Mungal. Drag and wake modification of axisymmetric bluff bodies using coanda blowing. *Journal of Aircraft*, 31:572–578, 1994.

[23] D. Greenwell and M. Garcia. Autorotation dynamics of a low aspect-ratio rectangular prism. *Journal of Fluids and Structures*, 49:640–653, 2014.

[24] F.-R. Grosche and G. Meier. Research at dlr gottingen on bluff body aerodynamics, drag reduction by wake ventilation and active flow control. *Journal of Wind Engineering and Industrial Aerodynamics*, 89:1201–1218, 2001.

[25] N. Hiremath. Vortex aerodynamics of rotors at high advance ratios. Technical report, Georgia Tech, 2018.

[26] N. Hiremath, N. Mothahari, and N. Komerath. Generalized approach for slung-load aerodynamics. *72nd Forum of AHS International*, 2016.

[27] N. Hiremath, D. Shukla, A. Pandey, J. Gregory, and N. Komerath. Pressure field of a yawed apect ration 1 circular cylinder. In *Proceedings of the ASME 2017 International Mechanical Engineering Congress and Exposition*, Tampa, FL, Nov 2017.

[28] F. Howard and W. Goodman. Axisymmetric bluff-body drag reduction through geometrical modification. *Journal of Aircraft*, 22:516–522, 1985.

[29] J. Howell, A. Sheppard, and A. Blakemore. Aerodynamic drag reduction for a simple bluff body using base bleed. *Mechanical Systems Journal*, 112:1085–1091, 2003.

[30] C. Hsing and C. Lan. Low-speed wall interference assessment/correction with vortex flow effect. *Journal of Aircraft*, 34:221–227, 1997.

[31] P. Irwin. Bluff body aerodynamics in wind engineering. Technical report, Rowan Williams Davies and Irwin Inc, 2007.

[32] G. Jones, J. Cincotta, and R. Walker. Aerodynamic forces on a stationary and oscillating circular cylinder at high reynolds numbers. Technical report, NASA, 1969.

[33] Y. Kawamura and T. Mizota. Wind tunnel experiment of bluff body aeodynamic models using a new type of magnetic suspension and balance system. *Journal of Fluids Engineering*, 135, 2013.

[34] N. Komerath and N. Hiremath. *Aerodynamic Loads on Arbitrary Shapes*. SCV Inc, 2016.

[35] N. Komerath, N. Hiremath, D. Shukla, J. Robinson, A. Jha, and A. Palaniappan. Aerodynamic loads on arbitrary configurations: Measurements, computations, and geometric modeling. 2017.

[36] G. Larose and A. D'Auteuil. On the reynolds number sensitivity of the aerodynamics of bluff bodies with sharp edges. *Journal of Wind Engineering and Industrial Aerodynamics*, 94:365–376, 2006.

[37] B. Lee. Some effects of turbulence scale on the mean forces on a bluff body. *Journal of Wind Engineering and Industrial Aerodynamics*, 1:361–370, 1975.

[38] J. Libii. Using wind tunnel tests to study pressure distributions around a bluff body: the case of a ciruclar cylinder. *World Transactions on Engineering and Technology Education*, 8:361–366, 2010.

[39] M. Manin, F. Ajalli, and M. Soltani. An experimental investigation of the reduced frequency effects into pressure coefficients of a plunging airfoil. *WIT Transactions on Engineering Sciences*, 59:153–161, 2008.

[40] R. Mehta. Aerodynamics of sports balls. *Ann. Rev. Fluid Mech.*, (17):151–189, 1985.

[41] R. Meroney. Wind-tunnel modeling of the flow about bluff bodies. Technical report, Colorado State University, 1986.

[42] M. Mokry and L. Ohman. Application of the fast fourier transform to two-dimensional wind tunnel wall interference. *Journal of Aircraft*, 17:402–408, 1980.

[43] N. Motahari, N. Hiremath, and N. Komerath. Aerodynamic load maps of bluff-body combinations in incompressible flow. *ASME 2016 Fluids Engineering Division Summer Meeting*, 2016.

[44] N. Motahari, T. Kim, D. Shukla, N. Hiremath, and N. Komerath. Divergence prediction for practical helicopter slung loads. *ASME 2016 International Mechanical Engineering Congress and Exposition*, 2016.

[45] N. Mothahari, F. Turbeville, N. Hiremath, and N. Komerath. Aerodynamic load maps of vechile shapes at arbitrary attitude. *SAE Technical Paper 2015-01-2574*, 2015.

[46] S. Murman. Lift and drag behavior of unconstrained bluff bodies. Technical report, NASA, 2010.

[47] G. Ocokoljic, B. Rasuo, and M. Kozic. Supporting system interference on aerodynamic characteristics of an aircraft model in a low-speed wind tunnel. *Aerospace Science and Technology*, 64:133–146, 2017.

[48] A. N. Ormond. Force measuring instrument, Dec. 29 1959. US Patent 2,918,816.

[49] K. Park, Y. Sung, and J. Han. Development of a cable suspension and balance system and its novel calibration methods for effective wind tunnel tests. *Measurement*, 170, 2021.

[50] P. Pereira, M. Herzog, and D. Dimarogonas. Slung load transportation with a single aerial vechicle and disturbance removal. *24th Mediterranean Conference on Control and Automation*, 2015.

[51] P. Pereira, M. Herzog, and D. Dimarogonas. Slung load transportation with a single aerial vehicle and disturbance removal. In *Proceedings of the 24th Mediterranean Conference on Control and Automation*, Athens, Greece, June 2016.

[52] S. Pirau, B. Liberi, N. Barbely, and N. Komerath. Aerodynamic load maps of bluff bodies: Measurements and diagnostics. *Journal of Mechanical Science and Technology*, 2009.

[53] V. Raghav, R. Shenoy, M. Smith, and N. Komerath. Investigation of drag and wake turbulence of a rotor hub. *Aerospace Science and Technology*, 28:164–175, 2013.

[54] M. Rizk and E. Murman. Wind tunnel wall interference corrections for aircraft models in the transonic regime. *Journal of Aircraft*, 21:54–61, 1983.

[55] A. Roshko. On the drag and shedding frequency of two-dimensional bluff bodies. Technical report, NACA, 1954.

[56] A. Roshko. On the wake and drag of bluff bodies. *Journal of the Aeronautical Sciences*, pages 124–132, 1954.

[57] A. Roshko. Perspectives on bluff body aerodynamics. *Journal of Wind Engineering and Industrial Aerodynamics*, 49:79–100, 1993.

[58] G. Schewe. Reynolds-number effects in flow around more-or-less bluff bodies. *Journal of Wind Engineering and Industrial Aerodynamics*, 89:1267–1289, 2001.

[59] D. Schrage, M. Smith, and J. Prasad. Georgia tech vertical lift research center of excellence. Technical report, Georgia Tech, 2017.

[60] S. Sharma, V. Raghav, N. Komerath, and M. Smith. Wall effect on fluid-structure interactions of a tethered bluff body. *Physics Letters A*, 377:2079–2082, 2013.

[61] W. Shih, C. Wang, D. Coles, and A. Roshko. Experiments on flow past rough circular cylinders at large reynolds numbers. *Journal of Wind Engineering and Industrial Aerodynamics*, 49:351–368, 1993.

[62] D. Shukla, N. Hiremath, and N. Komerath. Testing-based approach to determining the divergence speed of slung loads. *MDPI Review*, 2008.

[63] G. Suryanarayana, H. Pauer, and G. Meier. Bluff-body drag reduction by passive ventilation. *Experiments in Fluids*, 16:73–81, 1993.

[64] A. Szewczyk. The effects of three-dimensional imposed disturbances on bluff body near wake flows. Technical report, Notre Dame, 1994.

[65] M. Thomas, D. Pandey, and J. Nguyen. Flow characteristics of the renovated cal poly 3 x 4 ft subsonic wind tunnel. Technical report, California Polytechnic State Univeristy, 2011.

[66] G. S. Trimble. Six component balance for wind tunnels, Oct. 30 1956. US Patent 2,768,526.

[67] V. Tucker. Measuring aerodynamic interference drag between a bird body and the mounting strut of a drag balance. *J. exp. Biol.*, 154:439–461, 1990.

[68] G. Van Raemdonck and M. van Tooren. Time-averaged phenomenological investigation of a wake behind a bluff body. *BBAA VI International Colloquium on: Bluff Bodies Aerodynamics Applications*, 2008.

[69] A. Vargas and D. Anderson. Computer vision technique to estimate the slung load dynaimcs when coupled to a multirotor unmanned aerial vechicle. Technical report, Univeristy of Glasgow, 2017.

[70] Warner and Norton. Wind tunnel balances. Report 72, National Advisory Committee for Aeronautics, 1920.

[71] R. Willard and S. Kranzler. Improved wind tunnel data reduction procedure. Technical report, Sight, Sound and Motion, 1996.

[72] S. Yagmur, S. Dogan, M. Aksoy, E. Canli, and M. Ozgoren. Experimental and numerical investigation of flow structures around cylindrical bluff bodies. *EPJ Web of Conferences*, 92, 2015.

[73] A. Zahm. The six-component wind balance. Technical report, NACA, 1922.

[74] R. B. Zipin. Multi-axis load cell, Feb. 24 1976. US Patent 3,939,704.

Appendix A

ACTUATION CODES AND POST-PROCCESSING ROUTINES

A.1   Arduino

A.1.1   Stepper Motor Control

```
const int stepPin = 5;
const int dirPin = 2;
const int enPin = 8;
int x =0;
int y = 0;
int rots =10;


const int PhotoIn = 4;
int State = 0;
int counter = 0;
int Encoder;


void setup(){
  Serial.begin(9600);

  while (!Serial.available()){
  }
  Serial.println(Serial.read());

  delay(60000);
  pinMode(PhotoIn,INPUT);
  Encoder = digitalRead(PhotoIn);
  Serial.println(Encoder);

  pinMode(stepPin,OUTPUT);
  pinMode(dirPin,OUTPUT);
```

```
  pinMode(enPin,OUTPUT);
  digitalWrite(enPin,LOW);
  digitalWrite(dirPin,HIGH);

        while(y < rots){
                x = 0;
                while(x < 25000) {
                        digitalWrite(stepPin,HIGH);
                        delayMicroseconds(1200); // Set based off of desired RPM
                        digitalWrite(stepPin,LOW);
                        Encoder = digitalRead(PhotoIn);
                        Serial.println(Encoder);
                        x++;
                        delayMicroseconds(1200); // Set based off of desired RPM
                        }
                y++;
                }
    Serial.println("DONE");
}

void loop(){
}
```

A.1.2   Optical Encoder Control

```
const int PhotoIn = 4;
int State = 0;
int counter = 0;
int CurrentST;
int LastST;

void setup() {
  // put your setup code here, to run once:
pinMode(PhotoIn,INPUT);
Serial.begin(9600);
delay(60000);
// Read initial state
LastST = digitalRead(PhotoIn);
Serial.println(LastST);
delayMicroseconds(1200); // Match delay of stepper motor pulse
}
```

```
void loop() {
  // put your main code here, to run repeatedly:
CurrentST = digitalRead(PhotoIn);
Serial.println(CurrentST);
delayMicroseconds(1200); // Match delay of stepper motor pulse
}
```

A.2   Matlab

A.2.1   Post Processing Scheme

```
load("Cockrell_AR1_8rpm_400rpm_61423.txt");
Drag = Cockrell_AR1_8rpm_400rpm_61423(49300:end,1);
Side = Cockrell_AR1_8rpm_400rpm_61423(49300:end,2);
Torque = Cockrell_AR1_8rpm_400rpm_61423(49300:end,6);
time = linspace(0,720,length(Cockrell_AR1_8rpm_400rpm_61423(:,1)));
Time = time(49300:end);

d = designfilt('bandstopiir','FilterOrder',2, ...
'HalfPowerFrequency1',3,'HalfPowerFrequency2',50, ...
'DesignMethod','butter','SampleRate',Fs);
Drag = filtfilt(d,Drag);
Side = filtfilt(d,Side);
Torque = filtfilt(d,Torque);

figure(1)
plot(Time,Drag)

D1 = Drag(1:6000);
D2 = Drag(6001:12000);
D3 = Drag(12001:18000);
D4 = Drag(18001:24000);
D5 = Drag(24001:30000);
D6 = Drag(30001:36000);
D7 = Drag(36001:42000);
D8 = Drag(42001:48000);
D9 = Drag(48001:54000);
D10 = Drag(54001:60000);
D11 = Drag(60001:66000);
D12 = Drag(66001:72000);
```

```
S1 = Side(1:6000);
S2 = Side(6001:12000);
S3 = Side(12001:18000);
S4 = Side(18001:24000);
S5 = Side(24001:30000);
S6 = Side(30001:36000);
S7 = Side(36001:42000);
S8 = Side(42001:48000);
S9 = Side(48001:54000);
S10 = Side(54001:60000);
S11 = Side(60001:66000);
S12 = Side(66001:72000);

T1 = Torque(1:6000);
T2 = Torque(6001:12000);
T3 = Torque(12001:18000);
T4 = Torque(18001:24000);
T5 = Torque(24001:30000);
T6 = Torque(30001:36000);
T7 = Torque(36001:42000);
T8 = Torque(42001:48000);
T9 = Torque(48001:54000);
T10 = Torque(54001:60000);
T11 = Torque(60001:66000);
T12 = Torque(66001:72000);

t1 = Time(1:6000);
t2 = Time(6001:12000);
t3 = Time(12001:18000);
t4 = Time(18001:24000);
t5 = Time(24001:30000);
t6 = Time(30001:36000);
t7 = Time(36001:42000);
t8 = Time(42001:48000);
t9 = Time(48001:54000);
t10 = Time(54001:60000);
t11 = Time(60001:66000);
t12 = Time(66001:72000);

time60 = linspace(0,60,6000);

figure(2)
hold on
plot(time60,D2)
plot(time60,D3)
```

```
plot(time60,D4)
plot(time60,D5)
plot(time60,D6)
plot(time60,D7)
plot(time60,D8)
plot(time60,D9)
plot(time60,D10)
plot(time60,D11)
hold off

%% Time Average

DD = (D2+D3+D4+D5+D6+D7+D8+D9+D10+D11)/10;
SS = (S2+S3+S4+S5+S6+S7+S8+S9+S10+S11)/10;
TT = (T2+T3+T4+T5+T6+T7+T8+T9+T10+T11)/10;

figure(3)
plot(time60,DD)

%% Bin Average

deg = linspace(0.5,359.5,748);
idx(1) = 2;
for i = 1:749
    idx(i+1) = 2+i*8;
end

for i = 1:length(idx)-2
    Davgdeg(i) = sum(DD(idx(i):idx(i+2)))/17;
end

for i = 1:length(idx)-2
    Savgdeg(i) = sum(SS(idx(i):idx(i+2)))/17;
end

for i = 1:length(idx)-2
    Tavgdeg(i) = sum(TT(idx(i):idx(i+2)))/17;
end
```

A.2.2   Mounting Rod Sizing

```
 %% Christian Cueto - Rotating Test Rig Envelope Rod Sizing
clear
```

```
close all
clc

%% Max drag force exerted:
vmax=50; %m/s
crossA=.6096*.4572; %m^2
rho=1.225; %kg/m^3
Cd=2;
Fd=.5*rho*vmax^2*crossA.*Cd; %N

%% Find min diameter to avoid
Est=190e9; %GPa
Eal=69e9; %GPa

rodL=.4572; %m
deflMax=rodL*tand(1); %m
InertSt=(Fd*rodL^3)/(deflMax*3*Est);
InertAl=(Fd*rodL^3)/(deflMax*3*Eal);
rSt=((4*InertSt)/pi)^.25 %m
rAl=((4*InertAl)/pi)^.25 %m
rStmm=((4*InertSt)/pi)^.25*1000 %mm
rAlmm=((4*InertAl)/pi)^.25*1000 %mm
deflMaxmm=deflMax*1000; %m

%% Weight Calcs
wSt=7900*(pi*rSt^2*rodL) %kg
wAl=2720*(pi*rAl^2*rodL) %kg

%% Deflection vs Tunnel Speed
% change the below values for cross sectional aread and Cd of your
%cylinder and the script should calculate the rest.
v=linspace(0,50); %m/s
crossA= 0.219075^2; %m^2
Cd=1.3;
Fd2=.5*rho*v.^2*crossA.*Cd; %N
%rSt2=.0075; %m
rSt2=.005; %m
rSt3=.0075; %m
%rAl2=rSt2; %m
InertSt2=(pi*(rSt2.^4))/4;
InertSt3=(pi*(rSt3.^4))/4;
%InertAl2=(pi*(rAl2.^4))/4;
defVecSt=((Fd2(1,:)*rodL^3)./(3*Est.*InertSt2))*1000;
defVecSt2=((Fd2(1,:)*rodL^3)./(3*Est.*InertSt3))*1000;
%defVecAl=((Fd2(1,:)*rodL^3)./(3*Eal.*InertAl2))*1000;
```

```matlab
ceiling=ones(1,100);
ceiling=ceiling*deflMaxmm;
figure(1)
plot(v,defVecSt,'LineWidth',1.5)
hold on
plot(v,defVecSt2,'LineWidth',1.5)
%plot(v,defVecAl)
plot(v,ceiling,'LineWidth',1.5)
%set(gca, 'XScale', 'log')
grid on
ylabel('Deflection of the axle (mm)')
xlabel('Tunnel Speed (m/s)')
set(gca,'fontname','times')
set(gca,'fontsize',15)
legend('10mm rod deflection','15mm rod deflection', ...
'1 degree pitch change','Location','Northwest');
ylim([0 12])

%% Maximum Loading Graph
figure(2)
plot(v,Fd2,'LineWidth',1.5)
hold on
ceiling2=ones(1,100);
ceiling2=ceiling2*700;
plot(v,ceiling2,'LineWidth',1.5)
grid on
ylabel('Maximum Drag Force (N)')
xlabel('Tunnel Speed (m/s)')
set(gca,'fontname','times')
set(gca,'fontsize',15)
%title('8.65" PVC Pipe: Drag Force')
ylim([0 900])
legend('Frontal loading force profile',...
'Maximum load for sensing range','Location','Northwest');

figure (3)
Td2=Fd2*0.6096; %Nm
plot(v,Td2,'LineWidth',1.5)
hold on
ceiling3=ones(1,100);
ceiling3=ceiling3*30;
plot(v,ceiling3,'LineWidth',1.5)
grid on
set(gca,'fontname','times')
set(gca,'fontsize',15)
```

```
ylabel('Maximum Drag Torque (Nm)')
xlabel('Tunnel Speed (m/s)')
%title('8.65" PVC Pipe: Drag Torque')
legend('Frontal loading torque profile', ...
'Maximum load for sensing range','Location','Northwest');

% Reynolds Number 4 in nom
vl = linspace(0,45,10);

crossA=20.25/1550;
r = 2.25;
h = 4.5;
Lc = ((pi*r^2*h)/(2*pi*r*h+2*pi*r^2))/39.37;
mu = 18.18*10^-6;
Re4l = rho*vl*Lc/mu;
Re4b = rho*50*Lc/mu;

% Blockage percent 4 in nom

WTA = 4*3/10.764;

BLKSt24 = (crossA+(rodL*2*rSt2))/WTA;
BLKSt34 = (crossA+(rodL*2*rSt3))/WTA;

% Reynolds Number 8 in nom

vb = linspace(20,50,7);
vl = linspace(0,20,5);

crossA= 0.219075^2;
r = 4.3125;
h = 8.625;
Lc = ((pi*r^2*h)/(2*pi*r*h+2*pi*r^2))/39.37;
mu = 18.18*10^-6;
Reb8 = rho*vb*Lc/mu;
Rel8 = rho*vl*Lc/mu;

% Blockage percent 8 in nom

WTA = 4*3/10.764;

BLKSt28 = (crossA+(rodL*2*rSt2))/WTA;
BLKSt38 = (crossA+(rodL*2*rSt3))/WTA;

% Reynolds Number 6 in nom
```

```
vl = linspace(0,30,7);
vb = linspace(30,50,5);

crossA= 0.168275^2;
r = 3.3125;
h = 6.625;
Lc = ((pi*r^2*h)/(2*pi*r*h+2*pi*r^2))/39.37;
mu = 18.18*10^-6;
Rel6 = rho*vl*Lc/mu;
Reb6 = rho*vb*Lc/mu;

% Blockage percent 6 in nom

WTA = 4*3/10.764;

BLKSt26 = (crossA+(rodL*2*rSt2))/WTA;
BLKSt36 = (crossA+(rodL*2*rSt3))/WTA;
```

Appendix B

ASME IMECE 2023 PAPER

An agreed upon task when this thesis work was undertaken was an additional require-
ment from the thesis advisor Dr. Hiremath. The added task to write and submit a
condensed version of my thesis document for consideration at an engineering confer-
ence. This was accomplished by submitting said paper to consideration of the ASME
2023 International Mechanical Engineering Congress and Exposition. Included below
is the first page of the accepted paper that was presented by Co-author, Quintin
Cockrell, at the conference in New Orleans, LA on October 30th, 2023.

IMECE2023-113814

DEVELOPMENT AND INTEGRATION OF CONTINUOUS LOAD AND POSITION MEASUREMENT FOR QUASI-STEADY FLOWS

Quintin J. Cockrell[1,†], Nandeesh Hiremath[2,†,*],

[1]M.S. Candidate, Aerospace Engineering, California Polytechnic State University, San Luis Obispo, CA
[2]Assistant Professor, Aerospace Engineering, California Polytechnic State University, San Luis Obispo, CA

ABSTRACT

Obtaining aerodynamic forces and moments about all three orthogonal axes for arbitrary shapes at arbitrary orientations in a fast manner via a measurement technique specific to Cal Poly's low-speed wind tunnel to continually obtain the forces and moments under quasi-steady conditions is explored. A Continuous Rotation Technique (CR) uses a 6-DOF load cell and stepper motor to rotate an object about an axis for a complete rotation. The forces and moments acting upon the object pass through the stepper motor and interface plates and recorded by the load cell as the object is rotated continuously a finite number of rotations. An optical encoder installation tracks the progress of a rotation serving indicator between the subsequent rotations to determine starting angles and body slippage. Average loading of measurements at each timestep along the average time for rotation is found. This dataset along the average time is placed in 1-degree bins and averaged to a final dataset of load measurements at 1-degree intervals for a complete 360-degree load map. Testing of this technique is performed on aspect ratio 1 circular cylinder. This paper showcases the repeatability of the results in a different and smaller wind tunnel with improved certainty on angle measurements.

Keywords: Aerodynamics, Experimentation, Instrumentation, Measurement Techniques, Wind Tunnel

NOMENCLATURE

F Load cell force
F_{full} Fullscale force of load cell
V_{mea} Measured voltage
V_{exc} Excitation voltage
cal Load cell calbration factor
u Velocity (m/s)
Re Reynolds number
q Dynamic pressure (Pa)
L Characteristic length (m)
μ Dynamic viscosity (Pa-s)
ρ Density (kg/m^3)

1. INTRODUCTION

The aerodynamic load on a bluff body varies sharply with attitude. Several different fluid dynamic phenomena are encountered. Flat surfaces facing the flow have large regions of high pressure. Sharp corners generate flow separation. Strong vortices form at yawed corners, allowing separated shear layers to roll up into each other. Curved surfaces can generate unsteady flow separation, as the separation lines move along the surface in response to the location and strength of vortical structures breaking away. Base regions have separated flow. At higher speeds, skin friction becomes significant. While the fundamental knowledge base on bluff body aerodynamics has progressed slowly through the years, engineers have been called upon to design various applications where results on aerodynamic loads and flowfield features are essential. One such area of immense interest is the problem of carrying objects as loads slung below helicopters, and sometimes even under fixed-wing airplanes. Most such load/vehicle combinations are likely to experience divergent oscillations above some flight dynamic pressure: knowing the safe flight speed thus becomes crucial to operations. With vertical-lift aircraft such as the V-22 tiltrotor reaching speeds well over 100 m/s, the aerodynamics of complex shapes becomes increasingly interesting from the perspective of safe operations.

The traditional method for certification of slung loads has been to flight-test every combination of slung object and carrier vehicle. Computational fluid dynamics coupled with computational structural dynamics has been proposed and pursued [1, 2] as a means of predicting the dynamics of new configurations, with wind tunnel experiments seen as a validation step. Wind tunnel experiments and flight tests have been used to develop control surfaces and other control techniques to suppress divergence. However, it is seen that present-day computational efforts are unable to provide reliable *a priori* predictions for configurations where

[†]Joint first authors
[*]Corresponding author: nhiremat@calpoly.edu

Quintin Cockrell is a Master's student in the Aerospace Engineering Department at the California Polytechnic State University, San Luis Obispo. He attended the school for undergraduate where he earned a B.S in Aerospace Engineering with a concentration in Aeronautics and minor in Philosophy in 2022. His research interests fall into the fields of wind tunnel experimentation and renewable air-breathing propulsion systems. Upon the completion of this thesis, Quintin plans to return to the Pacific Northwest to his home state of Washington and pursue a career within the aerospace industry.